Spatial and temporal distribution of Arctic aerosols: new insights from the CALIPSO satellite

Maurizio Di Pierro

A dissertation
submitted in partial fulfillment of the
requirements for the degree of

Doctor of Philosophy

University of Washington
2013

Reading Committee:

Lyatt Jaeglé, Chair

Thomas P. Ackerman

Becky Alexander Suess

Robert Wood

Program Authorized to Offer Degree:
Atmospheric Sciences

University of Washington

Abstract

Spatial and temporal distribution of Arctic aerosols:
New insights from the CALIPSO satellite

Maurizio Di Pierro

Chair of the Supervisory Committee:
Professor Lyatt Jaeglé
Atmospheric Sciences

The Arctic is a receptor of pollution transported from distant regions. Pollution reaches the Arctic both in gaseous and aerosol form, both of which have important climatic and ecological implications. This dissertation focuses on aerosols in the Arctic, specifically their transport to and their distribution in space and time within the arctic troposphere. The cornerstone of this thesis is the analysis of the retrievals made by the satellite-borne Cloud-Aerosol Lidar with Orthogonal Polarization (CALIOP), a two-wavelength polarization-sensitive lidar that measures the atmospheric attenuated backscatter return and provides high-resolution vertical profiles of aerosols and clouds.

Chapter 2 uses CALIOP observations to follow the evolution of pollution aerosols transported from East Asia to the Arctic. The transport pathway is elucidated with backtrajectories and aerosol simulations with the GEOS-Chem chemical transport model. The polluted air mass experiences strong ascent within a cyclonic circulation near the source region. Once in the free troposphere, a block in the upper-air flow forces the circulation to take on a strongly southerly route. Since the air mass reaches the Arctic very rapidly (3-5 days), the aerosol scavenging is

incomplete. Transport is nearly-isentropic except in its initial phase. Once in the Arctic, the aerosol plume slowly subsides due to radiative cooling.

Using six years of CALIOP observations, Chapter 3 focuses on the horizontal, vertical and temporal distribution of Arctic aerosols. At low altitudes in the High Arctic (poleward of 70ºN), aerosol extinctions maximize in winter/early spring and reach their lowest values during summer. In the lower troposphere in the Low Arctic, in addition to the winter/early spring maximum, aerosol extinctions also display a secondary maximum in summer due to boreal forest fires. CALIOP measurements show that a major low-level Eurasian pollution transport pathway occurs on the western flank of the Siberian anticyclone. There is a progressive shift of the extinction maximum with altitude, from January at 0–2 km, to March at 2–5 km, to April at 5–8 km. In the free troposphere, the most polluted aerosol transport pathway occurs downwind of East Asia. Biomass burning emissions anomalies and the Arctic Oscillation control the interannual variability of aerosol extinction throughout the Arctic troposphere.

Chapter 4 focuses on comparing the Arctic aerosol distribution observed by CALIOP against a simulation from the GEOS-Chem global chemical transport model. Independent in situ observations are also used in this evaluation. The model successfully reproduces the seasonal cycle of sulfate aerosol concentrations at the surface, the vertical and temporal distribution of extinction in the free troposphere and the variability and magnitude of column optical depth from March to September. However the model does not reproduce the low-level extinction maximum observed by CALIOP and in situ instruments during winter. The model significantly underestimates observed sea-salt aerosol concentrations maximum at three High Arctic surface stations. This suggests a potential missing source of sea salt aerosols from blowing snow over sea ice from November to March. In summer, aerosol wet removal within the Arctic is too weak, possibly due

to a raindrop size distribution in the parametrization of below-cloud scavenging that is too large for the Arctic summer stratocumulus drizzle. The model underestimates extinction over central and eastern Russia through the troposphere in all seasons, suggesting that emissions in northern Russia are likely underestimated.

TABLE OF CONTENTS

Page

List of Figures

Figure Number Page

List of Tables

Table Number Page

ACKNOWLEDGEMENTS

I would like to express my sincere gratitude to my advisor, Professor Lyatt Jaeglé, for offering me the opportunity to work under her guidance and for believing in me. I am very grateful for her encouragement and guidance throughout the years. I would also like to thank my committee members, professors Rob Wood, Stephen Warren, Thomas Ackerman and Becky Alexander, as well as professors Tad Anderson and Mike Wallace and Edwin Eloranta for their valuable insights and discussion. I greatly enjoyed the companionship and support of my colleagues Sarah Strode, Yurong Luan, Yanxu Zhang, and Viral Shah, as well as the many friends I have made during these years and those who visited me from far away. I would like to thank the NASA CALIPSO Science Team, the many scientists who contributed to the development of the GEOS-Chem model, and my friend and collaborator Gabriele Curci. Finally, I would like to thank my parents Luisa and Giulio, my grandmother Cleondina, my sister Erica, my brother Alessandro and my wife Laura for their generosity, love and affection.

Chapter 1

INTRODUCTION

The Arctic is a pivotal region of the Earth's climate and a sentinel of our changing environment. In the last 30 years, the energy balance of the Arctic has greatly changed as seen most impressively in the dramatic decline of its summertime sea ice cover and rising surface temperatures, twice as large as the global average (IPCC). Aerosols originating from human activities have played a highly uncertain but potentially large role in perturbing the Arctic energy balance. The remoteness of this region, however, makes direct observations very challenging. Observations of the vertical and temporal distribution of Arctic aerosols are particularly scarce, but are much needed to help constrain climate model simulations and better understand the importance of the various processes that drive Arctic climate change.

1.1 Arctic aerosols observations

Perhaps the first observations of aerosol anthropogenic perturbations of the Arctic climate are attributable to Swedish geologist and Arctic explorer Nordenskiöld as early as 1883. He observed a pervasive layer of fine dust coating the Greenland ice, which seemed to cause accelerated melting of the ice in the form of cavities of 1 m wide and up to 1 m deep (Garrett and Verzella, 2008). It is now believed that the dust observed by Nordenskiöld contained soot from fly ash originating from the widespread combustion of coal during the industrial revolution. Several decades later (between 1948 and 1961), Alaska-based U.S. Air Force officer M. Mitchell Jr. systematically

recorded the presence of haze bands that limited the visibility to a few miles. In 1956 he called this phenomenon Arctic Haze.

Arctic Haze exhibits a regular seasonal cycle at the surface, with a maximum in pollutant concentration and light extinction in winter/early spring and a minimum from June to October (Law and Stohl, 2007). The winter/spring maximum is believed to be caused by favorable low-level transport from mid-latitude polluted regions. In addition, during winter the strong surface-based temperature inversions and the dry conditions lead to very little removal and thus accumulation of aerosols (Shaw, 1995). For opposite reasons, removal and dilution are stronger in summer, leading to much lower airborne pollutant concentrations in this season. Moreover, transport from the mid-latitudes in summer is also inhibited by the poleward retreat of the Polar Front (Stohl et al., 2006).

The chemical composition of Arctic aerosol mass measured at the surface is dominated by sulfate ($SO_4^{=}$) and organic matter, with other inorganic ions (e.g. NO_3^-, Cl^-, NH_4^+, Na^+, Ca^+, K^+, Mg^+) and black carbon (BC) making up the rest (Quinn et al., 2007; Law and Stohl, 2007). Sulfate originates from anthropogenic sources as well as natural sources such as sea spray oxidation of biologically produced dimethylsulfide (DMS) (Quinn et al., 2007). Recent measurements of aerosol composition throughout the troposphere indicate that organic aerosol produced by boreal forest fires may contribute a significant amount (50-70%) to the total aerosol mass in summer (Schmale et al., 2011).

Sulfate and BC aerosol concentrations have decreased by 30-70% in the Scandinavian and North American Arctic from the 1990s to the mid-2000s (Quinn et al, 2007; Gong et al., 2010). This decrease is due to the collapse of the economies of the Former Soviet Union, combined with declining emissions of BC and SO_2 in United States and Europe due to the implementation of

stricter air quality regulations. In contrast, emissions of BC in East Asia have more than doubled from 1980 to 2000 (Novakov, 2003).

1.2 Arctic aerosols and climate

While an aerosol can also interact directly with terrestrial radiation when it absorbs water to form a haze (Ritter et al., 2005), much of early Arctic aerosol research focused on the quantification of the aerosol direct shortwave radiative effect, which describes the aerosol interaction with solar radiation. Aircraft measurements carried out during the Arctic Gas and Aerosol Sampling Program (AGASP) in 1983 showed a negative radiative effect (cooling) at the surface in both spring (-11 W/m^2) and summer (-55 W/m^2) for the haze layers sampled. At the top of atmosphere (TOA) the haze effect was that of a warming in spring (+32 W/m^2), but a cooling in summer (-12 W/m^2) (Valero et al., 1984). The TOA radiative effect is highly dependent on the underlying surface albedo and the absorbing characteristics of the aerosol, and is more often negative in summer because of the low surface albedo (Iziomon et al., 2006). Quinn et al. (2008) used a climate model simulation to study the climate impacts of short-lived pollutants in the Arctic, and found that the aerosol surface radiative effect is negative in all seasons (from -0.04 W/m^2 in winter to -0.93 W/m^2 in summer), whereas at the TOA it is positive (from +0.08 W/m^2 in winter to +0.92 W/m^2 in spring). The associated surface temperature cooling, relative to pre-industrial times, varies between -0.5^{o}C in summer to -1.4^{o}C in winter.

The indirect effects of aerosols on cloud properties are highly uncertain but potentially comparable to the direct effect in terms of surface temperature response (-0.4^o to -0.8^{o}C) (Quinn et al., 2008). Since anthropogenic aerosols are efficient cloud condensation nuclei (CCN), they activate more droplets, which compete for available water vapor and grow to a smaller size. This causes an increase in cloud albedo (Twomey, 1977), thus reducing the amount of solar radiation

reaching the surface and leading to surface cooling. At the same time, longwave emissivity is enhanced, causing a warming of the surface. Other indirect effects include the increase in cloud lifetime (Albrecht, 1989), which also causes a surface cooling.

The deposition of soot on snow and ice has received much attention in recent years. Soot, which contains light-absorbing black carbon (BC) aggregates, decreases the albedo of ice and snow upon which it deposits. Clarke and Noone (1985) estimated an albedo reduction of 1-3% on fresh and more than 3% on older snow, because, when melting is incomplete, BC concentrates on the snow surface instead of being washed out. More recent estimates find Arctic-averaged snow albedo decreases of 0.6-4.7% for (Park et al., 2005; Flanner et al., 2007; Koch et al., 2009a, Wang et al., 2011). By reducing snow albedo, BC causes a positive radiative forcing at the surface, which accelerates snow-melt (Warren and Wiscombe, 1980). Greenland ice core observations show that deposition of anthropogenic BC in the Arctic peaked in the first decade of the 20th century to 5 times its pre-industrial levels, leading to a 1 W/m^2 radiative forcing in summer (McConnell, 2007). Hegg et al. (2010) analyzed the chemical constituents of snow samples collected across the Canadian and Siberian Arctic and found that biomass burning is the dominant source of BC at most sites. Doherty et al. (2010) found higher BC concentrations in snow in the Russian Arctic (34±46 ng g^{-1}) than in the Canadian Arctic (14±9 ng g^{-1}). Recent model estimates of BC surface radiative forcing confirm this albedo forcing maximum in spring, and estimate the effect at 1.2 W/m^2 averaged north of 60^{o}N, with roughly comparable contributions from open fires and anthropogenic sources (Wang et al., 2011). Quinn et al. (2008) have calculated an Arctic averaged surface temperature forcing of 0.3-0.8^{o}C from BC deposition, depending on season.

Koch et al. (2005) used a global climate model to estimate the contribution of the various source regions to the BC burden in the Arctic. They found that anthropogenic BC emitted in East

Asia dominates the BC Arctic burden. This indicates a potentially dramatic shift in the geographic distribution of the sources of Arctic aerosols. Shindell and Faluvegi (2009) estimate that the decrease in sulfate emissions that took place in Europe and United States as well as the increasing BC emissions from East Asia may be responsible for most of the Arctic warming observed in the last 3 decades.

1.3 Ecological impact of Arctic aerosols

In addition to climatic effects, the atmospheric transport of gaseous and aerosol pollutants has important ecological implications for the Arctic ecosystems, which are yet not well understood. The Arctic is considered a unique environment in that the coupling of climate, ecosystem behavior and air composition is uniquely strong among the Earth's biomes. Several bioclimatic feedbacks have been proposed, which include change in surface albedo caused by vegetation changes, as well as altered decomposition rates and biological productivity (Harte, 1986). The deposition of air pollutants on the earth surface can sometimes disrupt the biogeochemical cycles that tie together the various elements of the Arctic ecosystems. Ice core measurements reveal that the ice acidity has nearly doubled from 1950 to 1980, going from 8 to 14 μequiv H^+/l. (Barrie et al., 1989). Acidic precipitation, both in the form of rain and snow, is known to interfere with nitrogen fixing bacteria and lichens at pH as high as 5 and cause a reduction of the flux of nitrogen in streams and lakes (Harte, 1986).

Several types of Persistent Organic Pollutants (POP), including chlorinated organic compounds and pesticides have been detected in Arctic air, water and soils since the 1980s (Barrie et al., 1989). Since these pollutants are liposoluble, they accumulate in the biological tissue of organisms at the top of the food chain and may interfere with their biology. While industrial emissions of POP have decreased since the 1990s following stricter regulations, the soils in the

mid to high latitudes constitute a large reservoir of legacy emissions (Meijer et al., 2003). Recent concentration measurements of several polychlorinated biphenyl (PCBs) during an aerosol transport event at Spitsbergen showed concentrations up to 6.6 standard deviations above the climatological mean (Eckhardt et al., 2007). This indicates that re-emission of legacy POP from biomass burning in mid to high latitudes may represent a significant source of these toxic compounds. Since boreal forest fires are projected to increase following increasing temperatures (Stocks et al., 1998), there is concern for increasing emissions of POPs in future decades.

1.4 Thesis work

Although observations of Arctic surface aerosol mass concentrations and optical properties have been performed at a few sites since the 1980s, the spatial coverage of these observations remains very sparse and mostly concentrated in the North American and Scandinavian Arctic. Furthermore, little is known about the vertical distribution of aerosols over the Arctic, a key piece of information to estimate the impact of aerosols on climate (Haywood and Ramaswamy, 1998). The few available observations of the aerosol vertical distribution from specific aircraft campaigns are limited in space and time.

Early studies on transport pathways to the Arctic did not consider East Asia as a potentially significant source of aerosols to the Arctic and focused on the meteorological mechanisms conducive to aerosol pollution events that originated in Europe and North America (Rahn and McCaffrey, 1980; Barrie et al., 1981, Raatz and Shaw, 1984; Barrie et al., 1989). However, the dramatic shift in the distribution of anthropogenic emissions in the northern hemisphere from 1980 to 2000 is likely to have altered the source contribution to the Arctic burden of mid-latitude sources (Novakov et al., 2003). In recent years, pollution sources located in East Asia have received increasing attention, but their impact on the Arctic remains uncertain because of the lack of

observations to constrain models. In particular, current models disagree as to the importance of East Asia as a significant source of aerosol to the Arctic (Koch et al., 2005; Stohl et al., 2006).

More generally, the composition of the Arctic troposphere is poorly represented by the current generation of chemical transport models. For example, models appear to be unable to correctly simulate the observed seasonal cycle of aerosol extinction at the surface (Textor et al., 2006; Shindell et al., 2008). These models also display very large difference in terms of the mass of aerosols transported to the Arctic. Lack of observations and very specific meteorological conditions present over the Arctic are likely responsible for this lag of the Arctic behind other regions in terms of modeling.

My work relies on retrievals from the NASA/CNES Cloud-Aerosol Lidar with Orthogonal Polarization (CALIOP) on board the CALIPSO satellite, which began acquiring data in June 2006. CALIOP measures the attenuated backscatter return from the atmosphere as a function of height. The dense spatial coverage of CALIPSO orbits over the Arctic, together with CALIOP insensitivity to surface brightness makes CALIOP a useful tool for the study of Arctic aerosol. Through a series of algorithms, aerosol and cloud layers are detected and their optical depth and layer-integrated optical properties are calculated. Of particular importance for my work is the aerosol extinction coefficient, which I abbreviate as *extinction*. In order to interpret the CALIOP observations, I also use an aerosol-oxidant simulation of the GEOS-Chem Chemical Transport Model (CTM). GEOS-Chem is driven by assimilated meteorological fields from the Goddard Earth Observing System (GEOS) of the NASA Global Modeling and Assimilation Office.

In my thesis, I use CALIOP satellite observations to address the following two objectives:

1) Determine the horizontal, vertical, and seasonal distribution of aerosols over the Arctic.

2) Examine the ability of the GEOS-Chem CTM to reproduce the aerosol distribution observed by CALIOP, and identify gaps in our understanding of aerosols sources and sinks over the Arctic.

In Chapter 2 (*"Satellite observations of aerosol transport from East Asia to the Arctic: three case studies",* published in Atmospheric Chemistry and Physics, Di Pierro et al., 2011), I document three case studies of aerosol transport from East Asia to the Arctic and investigate their transport mechanisms. This chapter demonstrates the ability of CALIOP to track aerosol transport events to the Arctic and tests different ways to compare CALIOP retrievals to results from the GEOS-Chem CTM. Chapter 3 *("Spatial and seasonal distribution of Arctic aerosols observed by the CALIOP satellite instrument (2006-2012)"*, Atmospheric Chemistry and Physics, Di Pierro et al., 2013) compiles the horizontal and vertical distribution of Arctic aerosols retrieved by CALIOP over a 6-year period. In this chapter, I develop a methodology to reconstruct CALIOP's annual cycle of extinction and compare it against independent observations, with particular attention to the challenges and limitations that are specific to CALIOP retrievals in the Arctic. In Chapter 4, I perform a systematic comparison between the GEOS-Chem model and CALIOP observations for 2006-2010 and also examine the performance of GEOS-Chem against independent ground and aircraft observations. This validation enables me to identify gaps in our understanding of aerosol sources and removal processes in the Arctic. Finally, Chapter 5 presents a summary and recommendations for future work.

Chapter 2

SATELLITE OBSERVATIONS OF AEROSOL TRANSPORT FROM EAST ASIA TO THE ARCTIC: THREE CASE STUDIES

This chapter was published in Atmospheric Chemistry and Physics under the title:

Di Pierro, M., Jaeglé, L., and Anderson, T. L.: Satellite observations of aerosol transport from East Asia to the Arctic: three case studies, Atmos. Chem. Phys., 11, 2225-2243, doi:10.5194/acp-11-2225-2011, 2011.

2.1 Introduction

Starting in the 1950s, weather reconnaissance flights over the Arctic have revealed the existence of a haze that could extend over vast areas (Mitchell, 1956). This phenomenon became later known as Arctic Haze. Chemical analyses of the particulate matter showed that the haze was predominantly composed of sulfate and organic matter in addition to smaller quantities of black carbon (BC), ammonium, nitrate, and dust aerosols, as well as heavy metals and condensed volatile organic carbon compounds (Quinn et al., 2002).

Arctic Haze has long been attributed to transport of pollution from mid-latitude sources (Shaw, 1995). Chemical transport models (CTMs) show the dominant role of Europe and Russia as sources of low-level aerosol pollutants to the Arctic, but also show that East Asian and North

American aerosols make a significant contribution in the middle and upper troposphere during winter and spring (Klonecki et al., 2003; Koch and Hansen, 2005).

Transport to the Arctic is largely mediated by the Polar Dome, a tropospheric barrier of isentropic surfaces closing around the Arctic. If the transport is adiabatic, air parcels follow the northward sloping surfaces and necessarily have to ascend (Carlson, 1981). Also, following this argument, a warm air mass will ascend more than a cooler one when traveling from the mid-latitudes to the Arctic. Springtime transport of North American and East Asian sources to the Arctic generally occurs by export from the boundary layer in the warm conveyor belt of mid-latitude cyclones, followed by poleward transport along sloping isentropes in the free troposphere, and entrance into the polar dome from above by means of radiative cooling (Klonecki et al., 2003; Stohl, 2006). In contrast, northern Eurasian emissions tend to be transported at lower levels to the Arctic. Indeed, rapid low-level transport can be associated with a significant poleward retreat of the polar front in the presence of a blocking event or by prolonged flow over cold, snow-covered land masses causing strong diabatic cooling (Iversen and Joranger, 1985; Klonecki, 2003; Stohl, 2006).

In a recent CTM inter-comparison study, Shindell et al. (2008) demonstrated that the relative importance of different regions as aerosol sources for the Arctic is consistent across models, but that the absolute concentrations vary significantly. These discrepancies are linked to uncertainties in model representations of aerosol physical and chemical processes, but also to model-to-model variations in transport in the middle and upper troposphere. The scarceness of Arctic observations in the free troposphere has hindered the evaluations of models in that region. While there have been a number of recent aircraft campaigns targeting the Arctic (TOPSE, ARCTAS, ARCPAC and POLARCAT), most took place in the North American or European

sector of the Arctic. Thus the Siberian sector, where models predict a dominant influence of Asian aerosols, remains poorly characterized by observations.

In this study, we use Arctic observations of the vertical distribution of aerosols from the Cloud-Aerosol Lidar with Orthogonal Polarization (CALIOP) on board the CALIPSO satellite to examine three episodes of pollution export from East Asia to the Arctic, two during early spring and one in autumn. CALIOP has several advantages in the study of long-range transport of aerosols to the Arctic. Unlike passive satellite sensors (such as MODIS, MISR, PARASOL) it determines the precise vertical location of identified features and it can retrieve aerosol properties during both night and day, as well as over highly reflective ice and snow surfaces. The main limitations of CALIOP are that it only samples directly beneath the satellite (i.e. zero swath width) and that it can not detect aerosols located beneath optically thick clouds. In this paper, we combine CALIOP retrievals of aerosol attenuated backscatter and extinction, together with the GEOS-Chem model and backtrajectory calculations to track the transport pathway and evolution of these three Asian plumes. Section 2 presents a description of GEOS-Chem, CALIOP and the lagrangian trajectory model. The three case studies are presented in section 3. A discussion of the meteorological conditions favoring export from East Asia to the Arctic follows in section 4. Section 5 summarizes the results.

2.2 Models and observations

2.2.1 GEOS-Chem model

The GEOS-Chem global tropospheric chemistry model is driven by assimilated meteorological observations from the Goddard Earth Observing System (GEOS-5). The GEOS-5 meteorological fields have a 3 to 6 hour temporal resolution, with a native resolution of 0.5°x0.667° in the horizontal and 72 hybrid eta vertical levels, extending from the surface up to 0.01 hPa (~80 km).

For our simulations, we degrade these fields to a 2°x2.5° horizontal resolution and 47 vertical levels. We use version v8-02-04 of GEOS-Chem (http://acmg.seas.harvard.edu/geos/).

We conduct a fully coupled aerosol-oxidant simulation (Bey et al., 2001; Martin et al., 2003; Park et al., 2004) for 2007-2009. This simulation was initialized with a 1-year spin-up run. The aerosol simulation in GEOS-Chem represents the sulfate-nitrate-ammonium system (Park et al., 2004), organic carbon and black carbon (Park et al., 2003; Liao et al., 2007), sea salt (Alexander et al., 2005), and mineral dust (Fairlie et al., 2007), as an external mixture. The aerosol extinction and optical depth are calculated at 550 nm from Mie theory (Martin et al., 2003). This wavelength is close enough to CALIOP 532 nm channel to permit direct comparison between the two variables. The assumed dry aerosol mass extinction efficiencies are: 2.2 m^2/g for sulfate, 8 m^2/g for BC, 2.8 m^2/g for organic carbon, 2.4 m^2/g and 0.9 m^2/g for accumulation and coarse mode sea salt, respectively, and 3.1-0.16 m^2/g for dust depending on the size bin. We take into account aerosol growth as a function the local relative humidity.

Global anthropogenic emissions are from the EDGAR 3.2FT2000 database (Olivier and Berdowski, 2001) for 2000. Over Asia, these emissions are overwritten with the emission inventory of Zhang et al. (2009) corresponding to the year 2006, with annual anthropogenic and biofuel emissions of 47.1 Tg SO_2 , 2.97 Tg BC, and 6.57 Tg organic carbon. Dust emissions are based on a dust mobilization scheme that takes into account seasonal devegetation (Zender et al., 2003). Biomass burning emissions are taken from the GFEDv2 monthly inventory (Van der Werf et al., 2006). Aerosol dry deposition velocities are computed with a standard resistance-in-series scheme described by Wang et al. (1998). Wet deposition takes into account scavenging in convective updrafts in addition to in-cloud and below-cloud scavenging (Liu et al., 2001).

We also conduct a sensitivity simulation, where anthropogenic sources of aerosols and their precursors are turned off over Asia (defined here as 70-180°E; 8-70°N). In this simulation, we also turned off Asian dust sources in the region 42-152.5°E, 20-88°N. We infer the Asian contribution to the AOD by subtraction between the standard simulation and the sensitivity simulation with Asian anthropogenic aerosol sources and dust sources turned off. The resulting AOD will be referred to as 'Asian AOD'. In the discussion we will also refer to the anthropogenic sulfate component of the Asian AOD as 'Asian Sulfate AOD', and to the Asian AOD dust component as 'Asian Dust AOD'.

For comparison to CALIOP observations, we sample the model along the CALIPSO orbit tracks, extracting 1-hour time resolution tracer fields obtained from the original fields by linear interpolation. Thus, the observed and model scenes always coincide to within thirty minutes.

2.2.2 CALIOP lidar measurements

The CALIPSO satellite was launched on April 28, 2006 and is part of the sun-synchronous A-train constellation of satellites, which orbits at 705 km above mean sea level at an inclination of 98º, and completes 14.55 orbits a day crossing the equator at 1:30 p.m. local time. The CALIOP lidar is the main instrument on board CALIPSO. The lidar pulse is simultaneously emitted at 532 nm and 1064 nm, providing vertically resolved attenuated backscatter profiles of the atmosphere at both wavelengths. A polarization beam splitter allows measurements of the parallel and perpendicular components of the 532 nm return (Winker et al., 2004). The two channels and polarization information are used to discriminate between clouds and aerosols. CALIOP's vertical resolution is 30-60) m in the troposphere. The horizontal resolution of a single lidar shot is 333 m. However, a single atmospheric return signal is noisy, so consecutive profiles are averaged over 5-80 km to increase the signal-to-noise ratio and allow retrieval of faint features, such as aerosol

layers far from their source region (Vaughan et al., 2004). Nighttime retrievals are characterized by a higher lidar signal-to-noise ratio compared to daytime retrievals, thus higher accuracy is achieved at night in terms of locating the boundaries of the layers and retrieving optical properties.

The measured Level-1 attenuated return signal is analyzed by three consecutive algorithms, which locate the feature, classify it into cloud or aerosol, and solve for its optical properties (Vaughan et al., 2004; Winker et al., 2009; Young et al., 2009). The results are archived in Level-2 Layer products and Profile products. The Level-2 Layer products contain information on the spatial distribution (i.e. top and bottom of individual features) and integrated optical properties of all aerosol and cloud features detected. In the Level-2 Profile products, each atmospheric column is vertically resolved for its optical properties at a vertical resolution of 60-120 m in the troposphere.

The performance of the aerosol-cloud discrimination algorithm has been assessed on a global basis based on expert manual classification performed over one day of data (Liu et al., 2009). A percentage of 3-4% of aerosol layers are erroneously classified as clouds, which is roughly comparable to the percentage of cloud layers erroneously classified as aerosols. Under daytime conditions, misclassification of aerosols as clouds is more frequent than at nighttime, whereas the opposite occurs for the misclassification of clouds as aerosols. These issues will be addressed in more detail over the Arctic in this paper (Section 2.3.2.3).

In our study, we use version 2.01 Level-2 Cloud (5-km) and Aerosol (40-km) Profile products to perform comparisons between CALIOP and GEOS-Chem aerosol extinction profiles. The plume optical properties are extracted from 5-km Aerosol Layer products. The reported uncertainty in extinction coefficient is reported to be ±40% based on a 30% lidar ratio uncertainty (see http://www-calipso.larc.nasa.gov/products/). After our analysis was completed, a more recent

version of the CALIOP retrieval became available (v3.01). We have repeated our analysis with this more recent version in one case study, finding nearly identical results (see section 2.3.1).

2.2.3 HYSPLIT trajectory model

We use the NOAA Air Resources Laboratory Lagrangian Trajectory model HYSPLIT version 4.9 (Draxler, 2004) to calculate backtrajectories and identify the source of the aerosols observed over the Arctic. In our calculations, HYSPLIT is driven by the NCEP (National Centers for Environmental Prediction) GDAS (Global Data Assimilation System) meteorological fields with a 3 hourly temporal resolution, 1ºx1º horizontal resolution and 23 vertical levels from 1000 to 20 hPa. The trajectories include 3-D turbulent components to simulate dispersion (Draxler, 2004). We employed model vertical velocity fields rather than constraining the transport to occur on isentropic surfaces. The cross-section of aerosol plumes observed by CALIOP is sampled by taking the mid-point of each 5-km horizontal layer belonging to the plume. A random subset of 50 points is then extracted from the observed plume and backtrajectories are run for 10 days.

2.3 Case studies

We visually inspected CALIOP Level-2 observations for the year 2007 over the Arctic using the GEOS-Chem model simulation to locate large Asian aerosol transport events. We then selected three events during which the aerosol plumes were intercepted multiple times by the CALIPSO orbit tracks: February 28-March 4; March 12-19 and October 20-27, 2007.

2.3.1 February 28-March 4 2007 pollution export episode

This event was the most intense of the three presented here. Due to the large horizontal extent of the aerosol pollution plume (spanning more than 100º longitude), the CALIPSO orbits intercepted it 23 times over this 5-day period.

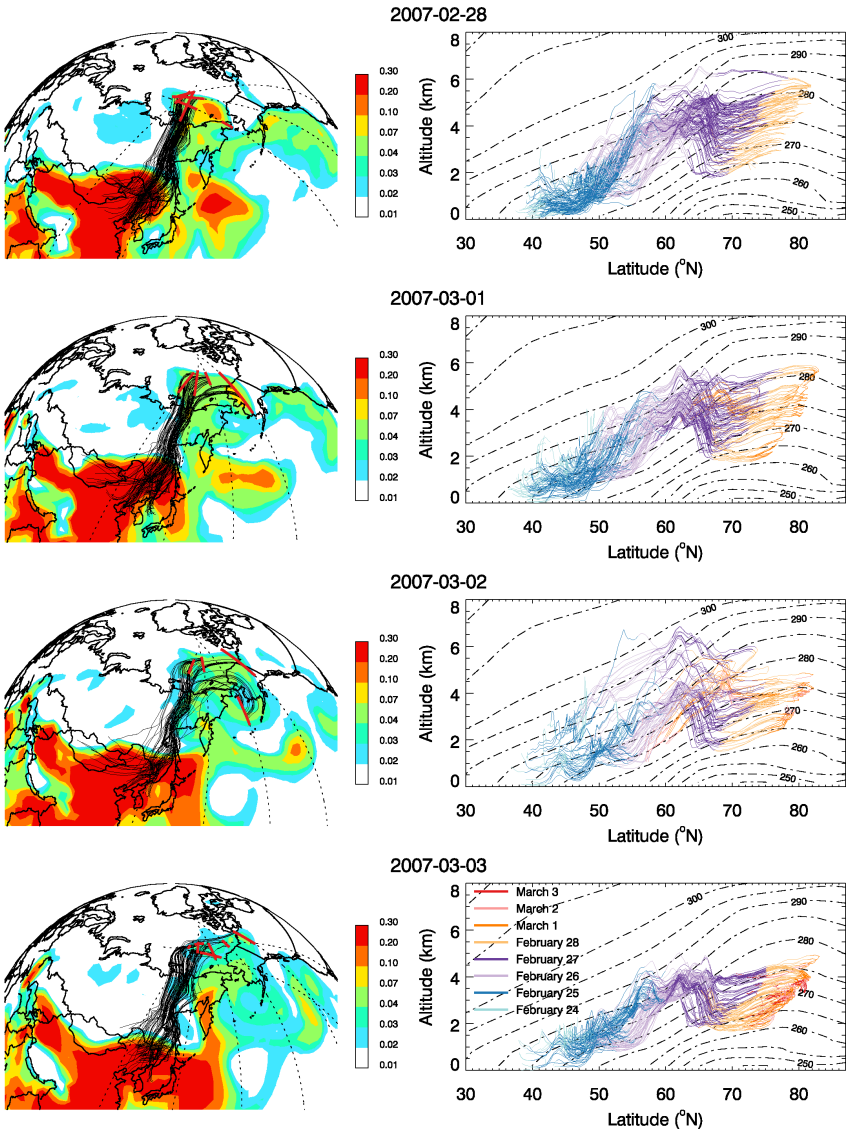

Figure 2.1: February 28-March 3 2007 Arctic haze event. Left column: daily Asian AOD (550 nm) calculated with GEOS-Chem. CALIPSO orbits are indicated by dashed lines and the parts of the orbit where the haze layers are observed are shown in red. Backtrajectories corresponding to the observed aerosol layers are shown in black, starting with 4-day backtrajectories on February 28, and incremented by 24 hours for each subsequent day. Right column: height (altitude above mean sea level) evolution as a function of latitude for backtrajectories shown on the left panel. The backtrajectories are color-coded based on the date (see legend on bottom panel). The potential temperature surfaces (dashed lines) are zonally averaged between 120ºE and 150ºW and temporally averaged between February 25, 0Z and the time the last plume was observed for each day.

Table 2.1: Summary of the 23 Arctic aerosol layers observed by CALIOP for the February 28-March 4, 2007 case study.

		CALIOP					GEOS-Chem	
Date[a]	Location of endpoints (Latitude ; Longitude)	Length (km)	Mean Altitude (km)	IVDR[b]	Color Ratio	AOD (plume | column)[c]	AOD w/o TH[d] (plume | column)	AOD w/ TH[d] (plume | column)
02-28 17.33 N	72.5ºN;148.8ºE | 80.9ºN;174.0ºW	1275	3.8	0.027	0.26	0.03 | 0.05	0.08 | 0.13	0.06 | 0.08
02-28 19.12 N	79.3ºN;146.7ºE | 81.8ºN;175.7ºW	720	5.3	0.029	0.26	0.03 | 0.03	0.03 | 0.10	0.02 | 0.05
02-28 19.59 D[e]	80.9ºN;169.8ºW | 81.8ºN;161.9ºE	475	5.7	0.031	0.36	0.04 | 0.05	0.02 | 0.08	0.02 | 0.04
02-28 20.51 N[e]	81.4ºN;145.3ºE | 81.8ºN;161.9ºE	235	5.2	0.032	0.29	0.03 | 0.03	0.05 | 0.11	0.04 | 0.07
02-28 21.37 D	77.1ºN;169.6ºW | 81.8ºN;141.8ºE	1065	5.1	0.028	0.32	0.04 | 0.04	0.06 | 0.12	0.06 | 0.07
02-28 23.16 D	64.5ºN;172.1ºW | 67.9ºN;175.5ºW	400	3.7	0.065	0.34	0.01 | 0.01	0.01 | 0.08	0.01 | 0.03
02-28 23.16 D	75.2ºN;171.8ºE | 80.1ºN;148.3ºE	765	3.7	0.021	0.31	0.04 | 0.04	0.06 | 0.12	0.06 | 0.07
03-01 13.20 N	60.1ºN;161.5ºW | 75.3ºN;141.6ºW	1845	4.0	0.044	0.27	0.10 | 0.11	0.07 | 0.10	0.06 | 0.06
03-01 14.59 N	75.2ºN;166.5ºW | 79.1ºN;151.1ºW	560	4.3	0.024	0.24	0.02 | 0.02	0.05 | 0.10	0.04 | 0.06
03-01 16.38 N	74.6ºN;167.2ºE | 81.3ºN;153.9ºW	1120	3.6	0.026	0.24	0.01 | 0.02	0.07 | 0.11	0.05 | 0.06
03-01 18.17 N	76.9ºN;149.4ºE | 81.8ºN;164.4ºW	1040	4.1	0.024	0.25	0.04 | 0.04	0.06 | 0.11	0.05 | 0.06
03-02 12.24 N	63.1ºN;145.3ºW | 74.9ºN;128.7ºW	1440	4.0	0.025	0.22	0.02 | 0.02	0.04 | 0.08	0.03 | 0.03
03-02 14.03 N	54.1ºN;175.7ºW | 63.1ºN;170.1ºW	1040	2.1	0.052	0.28	0.08 | 0.08	0.03 | 0.09	0.01 | 0.04
03-02 15.42 N	75.5ºN;176.5ºW | 79.8ºN;156.7ºW	660	3.5	0.028	0.26	0.01 | 0.05	0.06 | 0.09	0.03 | 0.04
03-02 17.21 N	77.2ºN;164.2ºE | 80.8ºN;171.6ºW	640	3.5	0.027	0.27	0.02 | 0.03	0.05 | 0.10	0.04 | 0.05
03-03 11.29 N	64.1ºN;130.6ºW | 71.0ºN;122.7ºW	820	3.6	0.029	0.26	0.04 | 0.04	0.04 | 0.07	0.02 | 0.02
03-03 13.08 N	71.6ºN;146.4ºW | 74.3ºN;141.0ºW	340	3.4	0.019	0.21	0.01 | 0.03	0.04 | 0.09	0.04 | 0.05
03-03 14.47 N	72.3ºN;169.8ºW | 77.6ºN;155.6ºW	700	3.1	0.020	0.21	0.01 | 0.01	0.04 | 0.08	0.02 | 0.03
03-03 16.26 N	77.4ºN;179.1ºE | 80.3ºN;163.8ºW	480	3.5	0.026	0.29	0.02 | 0.02	0.02 | 0.08	0.02 | 0.04
03-03 18.05 N	80.2ºN;171.4ºE | 80.9ºN;179.2ºE	160	3.3	0.029	0.23	0.01 | 0.02	0.01 | 0.08	0.00 | 0.02
03-03 20.30 D	78.7ºN;159.7ºW | 80.4ºN;172.5ºW	320	3.6	0.032	0.29	0.01 | 0.02	0.02 | 0.07	0.01 | 0.02
03-03 22.09 D	71.7ºN;163.8ºW | 77.1ºN;177.5ºW	720	2.8	0.010	0.24	0.01 | 0.01	0.03 | 0.07	0.02 | 0.03
03-04 10.33 N	61.0ºN;119.1ºW | 65.8ºN;115.2ºW	560	3.9	0.029	0.22	0.05 | 0.05	0.04 | 0.07	0.02 | 0.02
03-04 15.30 N	77.7ºN;165.9ºW | 78.7ºN;160.9ºW	160	2.9	0.026	0.27	0.02 | 0.02	0.02 | 0.06	0.00 | 0.00
Mean[f]	--	730	3.8	0.030±0.011	0.26±0.04	0.037 | 0.044	0.049 | 0.093	0.036 | 0.048

(a) Dates are given as MM-DD UTC time (hh.mm). N or D indicates night or day observations.
(b) Integrated Volume Depolarization Ratio (IVDR).
(c) The first number corresponds to the observed AOD in the plume only while the second number indicates the AOD for the entire column (0-10 km). These numbers are obtained by first regridding the CALIOP observations to the horizontal and vertical resolution of GEOS-Chem.
(d) The two GEOS-Chem columns correspond to the AOD without threshold (w/o TH) and with threshold (w/ TH) based on the CALIOP sensitivity.
(e) The third haze layer was observed under daytime and nighttime conditions so it straddles 2 files.
(f) All mean aerosol properties are weighted by the length of the cross-section.

2.3.1.1 Morphology and optical properties of the observed haze layers

Figure 2.1 shows the locations of the haze layers observed by CALIOP during the February 28-March 3 period. The CALIPSO orbits are drawn with a dashed line and their segments in the haze layer are in red. The layers were first observed over the East Siberian Arctic sector on February 28, and then slowly drifted east to the North American sector. Table 2.1 presents a summary of the latitude/longitude range, height, aerosol optical depth (AOD), integrated volume depolarization ratio (IVDR) and integrated attenuated color ratio (ratio between attenuated backscatter at 1064 nm and 532 nm, henceforth simply referred to as color ratio) for the 23 plume cross sections observed by CALIOP during this event.

Figure 2.2 displays a subset of five CALIOP and GEOS-Chem aerosol extinction cross sections of the haze event. The aerosol layers appear as thin elongated features ranging in thickness from 500 to 2000 m, and individual segments had a length of 160 km to 1845 km (Table 2.1). The altitude of the features ranged from 1.5-4.5 km altitude at lower latitudes (60-70°N) increasing to 2-6.5 km poleward of 70°N.

The ascending shape of the aerosol plumes is characteristic of transport along sloping isentropes. The northward tilt of the aerosol layers is consistent with the local configuration of potential temperature surfaces (dashed lines in Figure 2.2). The tilt is higher than the potential temperature surface slope in some instances, e.g. panel c in Figure 2.2, indicating that various parts of the plume were emitted from sources at different potential temperatures and also underwent different histories of diabatic processes. In the case of panel b (Figure 2.2), the lack of tilt is associated with a local flattening of the isentropes.

By integrating the CALIOP extinction over the length and height of individual plumes, we find AODs ranging from 0.01 to 0.08, with a mean of 0.036 for all observations (Table 2.1). If we

integrate over the entire vertical column (0-10 km) the mean AOD increases to 0.044. The plume displays fairly uniform values of IVDR, with most values below 0.03, indicating small particles and relatively small amounts of dust. Indeed, because of their large size and non-sphericity, dust aerosols exhibit the highest depolarization ratio (IVDR>0.06) of all aerosol species, while other aerosols have a much lower depolarization ratio (Liu et al., 2008). Values of the color ratio (0.21-0.36) are also small, indicating sub-micron size, typical of pollution aerosols or smoke.

Our results, obtained with version 2.01 of the CALIOP retrieval, do not change much when compared with the more recent version, 3.01. With v3.01, mean plume AOD is 0.030 (compared to 0.036 for v2.01), with mean IVDR 0.029 (0.03 for v2.01) and Color Ratio 0.24 (0.26 for v2.01). We find that the aerosol/cloud classification is the same for both versions, except for 2 out of the 23 CALIOP cross sections, where v3.01 classifies the features as mostly clouds, while v2.01 classifies them as aerosols.

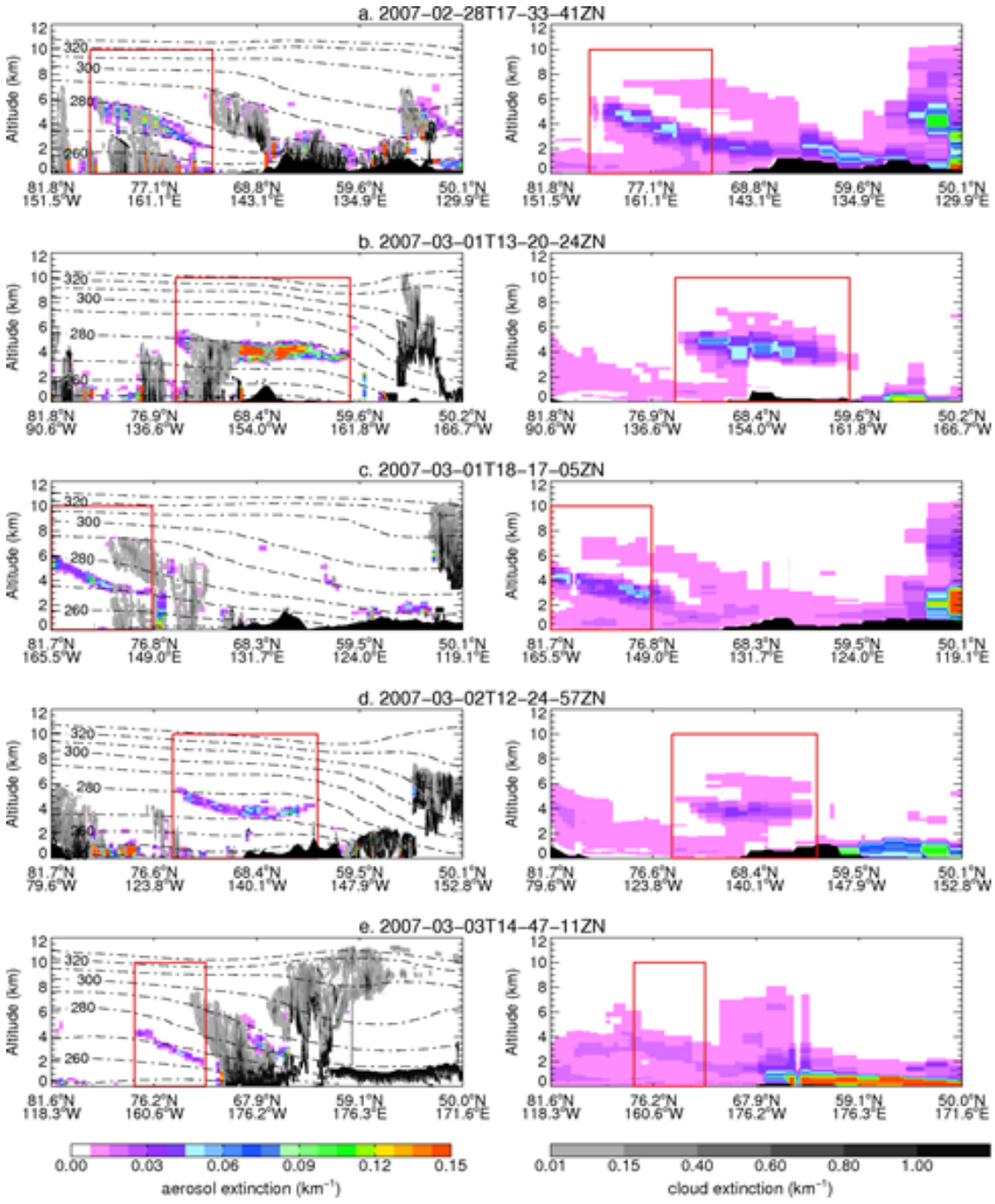

Figure 2.2: Aerosol extinction comparison between CALIOP (L2 profile data, left) and GEOS-Chem (right). Five scenes were chosen among the 23 East Asian plumes observed by CALIOP during the February 28-March 4 period. Aerosol extinctions are plotted in color and cloud extinctions observed by CALIPSO are in gray. The red box delimits the aerosol layers that have an East Asian origin (see text). Potential temperature contours are shown with dashed-dotted lines on the left panels. The text on top of each panel is the CALIOP file identifier.

2.3.1.2 Asian origin and meteorology of the event

The backtrajectories corresponding to each observed aerosol layer are shown in Figure 2.1. We are only displaying trajectories that originate in the boundary layer (defined here as reaching an altitude below 1500 m), which account for roughly half of the backtrajectories. The plume originated from the boundary layer over NE China 4-8 days prior to observations. In addition, 6% of the trajectories come from the Gobi desert. The Asian origin of the haze event is confirmed by the GEOS-Chem Asian AOD simulation, with observed plumes located over areas with enhancements in Asian AOD (Figure 2.1).

The observed airmasses ascended to 4-7 km altitude in 24 hours and most of the ascent took place between February 25 12Z and February 27 0Z (Figure 2.1, right panels). Potential temperature and precipitation computed along the trajectories shows that the initial stage of diabatic transport was associated with precipitation to the ground. This was followed by dry transport; with gradual ascent following isentropic surfaces poleward of 67ºN. We find that the departure from isentropy is due to radiative cooling at a rate of ~1.5 ºC/day, in agreement with previous studies (Curry, 1983; Carlson, 1981). The rapid altitude variations for backtrajectories between 55ºN and 60ºN are associated with orographic effects as parcels are traveling above the mountain ranges of southeastern Siberia at low altitudes.

Subsidence within the Arctic basin could be seen only for the last 16 hours of the last plume on March 4 at 15:30 UTC, with a subsidence rate of ~ 1 cm/s. No plume was observed to reach the surface. It is likely that the plumes dissipated to the point where their backscatter fell below CALIOP detection threshold even if subsidence continued.

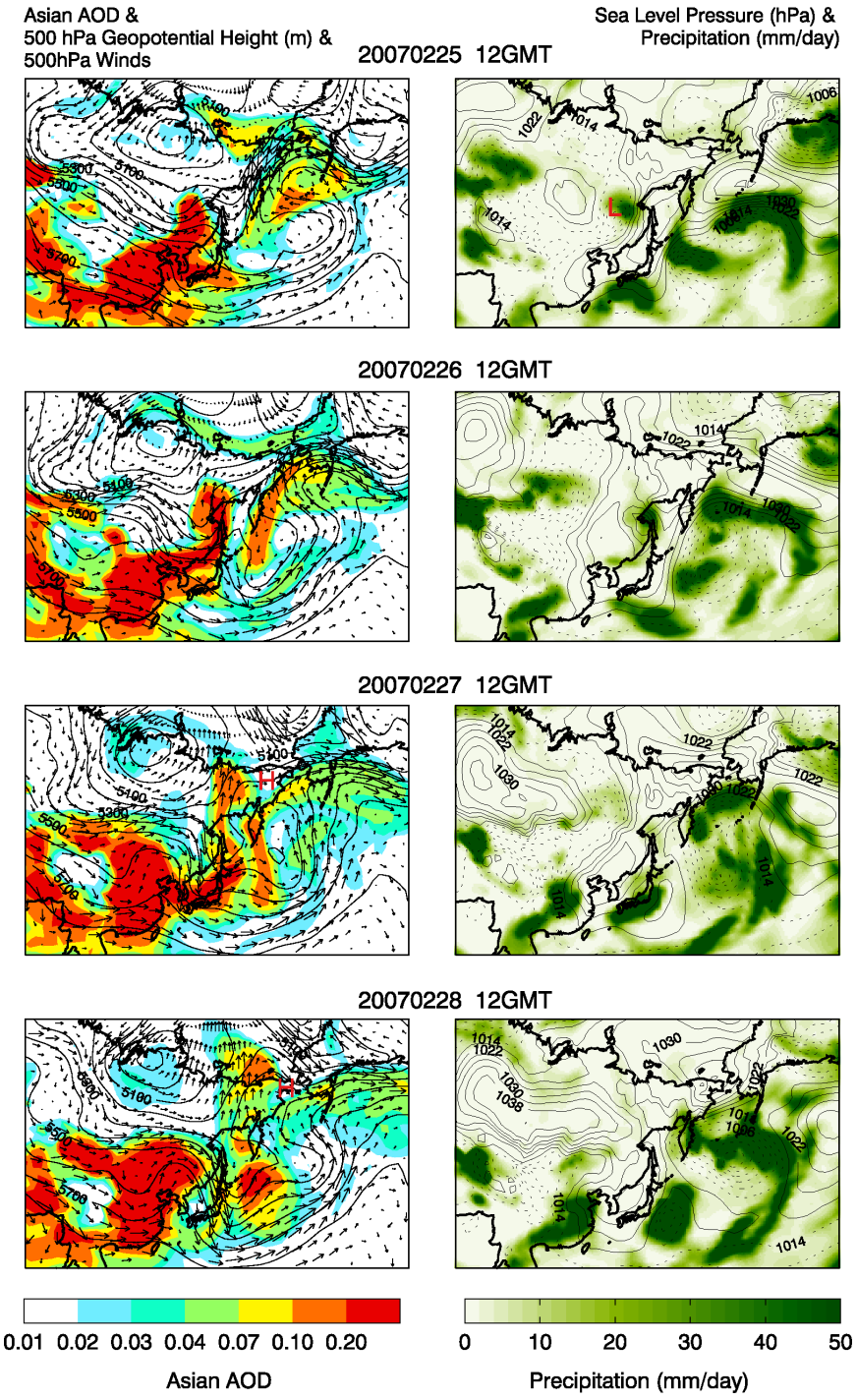

Figure 2.3: Left panel: 500 hPa geopotential height (black contours) and corresponding wind vector evolution during the initial period of aerosol export, together with GEOS-Chem Asian AOD (in color) for February 25-28, 2007. Right panel: Sea level pressure (contours) and precipitation (green). SLP contours (4 hPa) are dashed when SLP is below 1014 hPa. H indicates the blocking high pressure system; L shows the location of the low pressure center.

This export event was triggered by a mid-latitude cyclone that formed on February 21 North of the Black Sea and began to travel eastward over continental Asia. On February 23 at 12 UTC, the cyclone reached its maximum intensity (987 hPa). It then began to weaken as it continued on its eastward route. A secondary cyclogenesis occurred as the low pressure center passed over the Altai mountain range, a region of active lee cyclogenesis (Chen et al., 1991). The pressure minimum decreased for two consecutive 6-hour periods and reached a new minimum on February 24 at 12 UTC.

Figure 2.3 (left panels) shows the modeled Asian AOD, 500hPa geopotential heights and 500 hPa winds for February 25-28. Sea level pressure and precipitation are displayed on the right panels. Geopotential heights and sea level pressure are from the NCEP-NCAR Reanalysis (Kalnay et al., 1996), whereas precipitation is from GEOS-5. The secondary cyclogenesis is reflected in the mid-tropospheric deepening of a secondary wave that becomes a full trough on February 26, as shown in the two top panels of Figure 2.3.

The low pressure center (marked with an L in the top right panel of Figure 2.3) began to manifest its influence upon NE China on February 25, when persistent warm advection anticipated the passage of a cold front. In the early stages of the export the AOD enhancement is found on the east side of the surface low. Surface convergence around the low on February 25 provides the ascending motion by means of a warm conveyor belt, which lifts the pollution to the middle troposphere.

Both the trajectories and GEOS-5 meteorological fields indicate that precipitation was associated with this lifting between February 25 and February 27, south of 65°N. As a result of this precipitation, the aerosol-laden air mass underwent strong scavenging associated with transport in the low pressure system. By contrasting the GEOS-Chem AOD for individual aerosol

species over the Arctic with the corresponding values over the source region, we estimate export efficiencies of ~15% for sulfate, ~20% for BC, and 30-40% for dust.

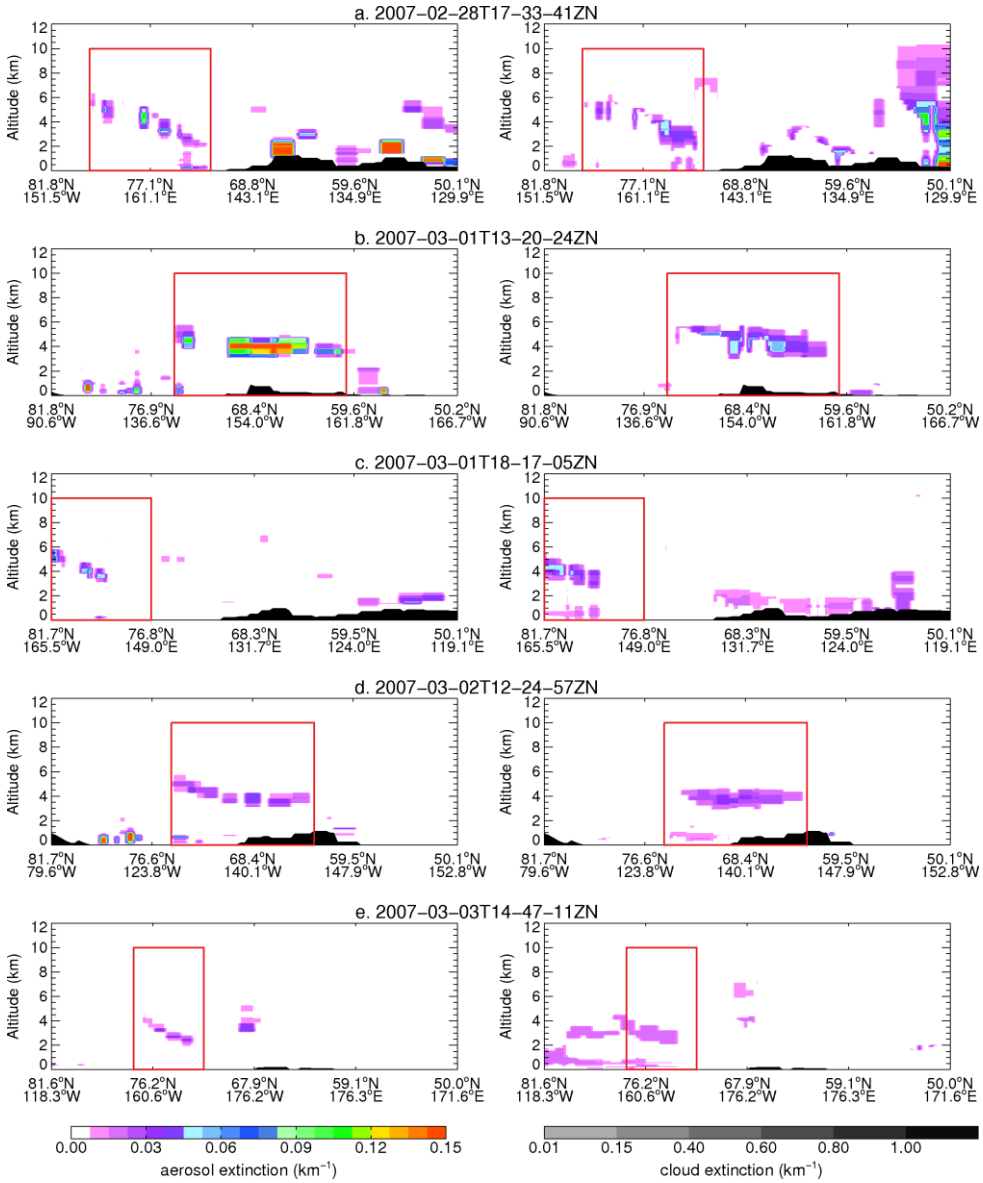

Figure 2.4: Same as Figure 2.2, but with the CALIOP extinction gridded onto the GEOS-Chem horizontal and vertical grid (left panels). The GEOS-Chem extinction cross sections (right panels) take into account the CALIOP altitude-dependent backscatter sensitivity threshold. In addition, model extinction is set to zero when CALIOP observes clouds.

The subsequent rapid poleward transport of the plume is associated with a NW Pacific blocking high pressure system (H in bottom left panels, Figure 2.3), which began to form at the end of February and persisted until mid-March. This high lead to a split Asian outflow, with one branch moving poleward, and the other branch going East out to the Pacific.

2.3.1.3 Comparison between observed and modelled haze layers

The model generally reproduces both the horizontal and vertical location of the observed aerosol layer (Figure 2.2, Table 2.1). However, while the boundaries of the haze layer are well defined in the observations, they appear to be more spread-out in the model. This could be due to the coarser horizontal and vertical resolution of the model. The difference between model and observations could also be associated with the sensitivity of the CALIOP instrument. Winker et al. (2009) report a 532 nm backscatter sensitivity threshold for CALIOP nighttime retrievals at 80 km horizontal averaging of $2x10^{-4}$ km^{-1} sr^{-1} at 10 km altitude increasing to $4x10^{-4}$ km^{-1} sr^{-1} at the surface. We take into account this altitude-dependent sensitivity by setting to zero model backscatter coefficients below the CALIOP detection threshold (Figure 2.4, right panels). We also grid CALIOP observation onto the model grid (Figure 2.4, right panels). This more direct comparison leads to sharply defined boundaries in the model plumes, in better agreement with CALIOP.

Figure 2.5 shows a comparison between satellite-retrieved and modeled mean extinction profiles averaged over the cloud free regions within the red box in Figure 2.4. We applied the CALIOP sensitivity threshold to the model extinction. In performing the horizontal averaging for both model and observations, we excluded atmospheric columns below the top of the CALIOP-detected clouds. The model generally captures the layer height and extinction observed by CALIOP. As summarized in Table 2.1, the model plume average AOD (0.036) is in good agreement with observations (0.037). For the 0-10 km column, the observed and modeled AOD are 0.044 and

0.048, respectively. If we do not take into account the altitude dependent sensitivity, we find that the model overestimates observations by 40-100% (model plume AOD: 0.049, model column AOD: 0.093, Table 2.1).

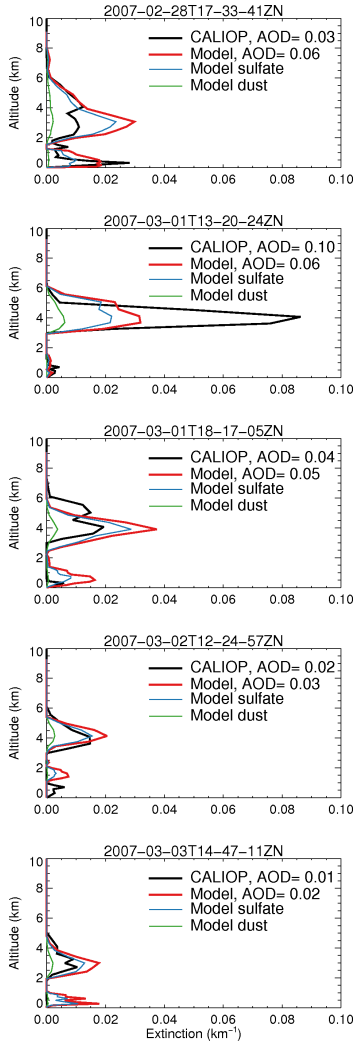

Figure 2.5: CALIOP (black) and GEOS-Chem (red) mean aerosol extinction profiles for the cloud-free regions within the red boxes in Figure 2.4. The CALIOP sensitivity threshold is applied to the modeled extinction profiles. The CALIOP extinction is gridded onto the GEOS-Chem vertical grid. The green and blue lines represent the extinction attributed to dust and sulfate respectively. The modeled and observed AOD, calculated by integration of the extinction profile over the vertical extent of each plume are listed on each panel.

Table 2.2: Summary of the 37 Arctic aerosol layers observed by CALIOP during the March 12-19 export event. Refer to Table 2.1 for the legend.

		CALIOP					GEOS-Chem
Date	Location of endpoints (Latitude ; Longitude)	Length (km)	Mean Altitude (km)	IVDR	Color Ratio	Int. β' [(a)] (x 10^{-3} sr^{-1})	Int. β' [(a)] (x 10^{-3} sr^{-1})
03-12 17.59 N	64.5ºN; 132.3ºE | 71.1ºN; 140.1ºE	800	4.6	0.063	0.29	-	-
03-13 18.43 N	66.8ºN; 123.7ºE | 77.4ºN; 145.1ºE	1360	4.0	0.054	0.30	-	-
03-14 00.26 D	76.6ºN; 150.6ºE | 80.5ºN; 128.4ºE	640	4.1	0.058	0.31	1.03	0.70
03-14 02.05 D	69.1ºN; 141.4ºE | 77.7ºN; 121.7ºE	1120	3.2	0.069	0.36	1.81	0.94
03-14 18.34 D	79.8ºN; 147.2ºE | 81.3ºN; 164.6ºE	355	3.9	0.062	0.32	1.77	1.20
03-14 19.26 N	74.2ºN; 124.3ºE | 79.6ºN; 146.0ºE	800	4.3	0.053	0.25	-	-
03-14 20.13 D	79.8ºN; 122.6ºE | 81.8ºN; 167.3ºE	795	3.0	0.053	0.40	-	-
03-14 21.52 D	79.5ºN; 175.5ºE | 81.6ºN; 121.8ºE	960	3.4	0.054	0.34	-	-
03-14 23.30 D	78.0ºN; 159.0ºE | 81.7ºN; 121.2ºE	820	3.2	0.077	0.41	-	-
03-15 01.09 D	76.9ºN; 138.5ºE | 81.3ºN; 106.6ºE	800	3.9	0.069	0.30	-	-
03-15 17.38 D	79.5ºN; 159.4ºE | 80.5ºN; 129.6ºW	1275	4.0	0.049	0.27	0.98	0.91
03-15 19.17 D	80.8ºN; 146.2ºE | 81.4ºN; 167.5ºW	770	3.7	0.063	0.34	1.57	0.86
03-15 20.56 D	80.9ºN; 176.7ºE | 81.8ºN; 148.1ºE	480	3.4	0.072	0.31	-	-
03-16 01.53 D	81.2ºN; 97.7ºE | 81.7ºN; 63.2ºE	560	3.2	0.048	0.29	0.51	0.32
03-16 11.46 D	79.3ºN; 113.9ºW | 81.2ºN; 95.6ºW	395	4.7	0.065	0.29	-	-
03-16 12.39 N	72.9ºN; 136.4ºW | 79.1ºN; 115.2ºW	880	3.7	0.047	0.21	0.44	0.83
03-16 13.25 D	79.3ºN; 139.0ºW | 81.8ºN; 93.9ºW	835	2.7	0.051	0.41	-	-
03-16 14.17 N	76.3ºN; 152.6ºW | 79.1ºN; 140.3ºW	420	3.2	0.047	0.24	-	-
03-16 15.04 D	79.3ºN; 163.6ºW | 81.8ºN; 116.0ºW	875	3.6	0.061	0.35	-	-
03-16 16.43 D	80.7ºN; 118.0ºW | 81.3ºN; 167.0ºW	820	4.4	0.064	0.34	2.14	0.98
03-16 18.22 D	75.2ºN; 114.2ºW | 81.8ºN; 165.6ºW	1270	4.1	0.073	0.30	2.32	1.10
03-16 20.01 D	76.4ºN; 142.3ºW | 80.4ºN; 163.9ºW	640	4.1	0.081	0.31	1.15	0.74
03-17 11.43 N	67.2ºN; 130.7ºW | 76.3ºN; 114.0ºW	1140	3.2	0.063	0.26	1.66	0.79
03-17 12.29 D	79.0ºN; 126.8ºW | 80.7ºN; 113.5ºW	315	3.9	0.052	0.27	-	-
03-17 13.22 N	69.2ºN; 153.0ºW | 78.8ºN; 127.8ºW	1280	3.7	0.046	0.22	0.83	0.68
03-17 14.08 D	79.0ºN; 151.5ºW | 81.8ºN; 115.3ºW	715	3.8	0.053	0.26	-	-
03-17 15.47 D	81.6ºN; 119.7ºW | 81.8ºN; 139.9ºW	320	3.8	0.065	0.33	-	-
03-17 17.26 D	78.8ºN; 114.2ºW | 81.4ºN; 140.2ºW	560	3.8	0.067	0.28	-	-
03-17 19.05 D	71.7ºN; 117.4ºW | 77.3ºN; 131.6ºW	740	3.1	0.079	0.28	0.37	0.30
03-17 20.44 D	66.6ºN; 135.4ºW | 75.0ºN; 149.1ºW	1040	3.2	0.079	0.34	1.31	0.66
03-18 12.26 N	65.5ºN; 143.3ºW | 74.1ºN; 130.7ºW	1060	3.3	0.044	0.21	1.86	0.92
03-18 14.05 N	65.5ºN; 168.0ºW | 74.6ºN; 154.4ºW	1115	2.5	0.052	0.26	0.47	0.45
03-18 19.48 D	69.0ºN; 124.6ºW | 74.8ºN; 134.5ºW	720	3.1	0.096	0.32	1.13	0.52
03-19 11.31 N	66.4ºN; 128.5ºW | 69.1ºN; 125.4ºW	320	3.3	0.045	0.22	0.60	0.55
03-19 11.31 N	72.9ºN; 119.3ºW | 76.3ºN; 110.9ºW	440	2.4	0.033	0.18	-	-
03-19 13.10 N	70.2ºN; 148.6ºW | 76.1ºN; 136.1ºW	760	3.4	0.045	0.24	-	-
03-19 20.32 D	68.1ºN; 134.0ºW | 73.3ºN; 142.0ºW	640	2.2	0.097	0.30	1.03	0.43
Mean[(b)]	--	780	3.5	0.061±0.014 N:0.051±0.008 D:0.067±0.041	0.30±0.05 N:0.25±0.03 D:0.32±0.04	1.21±0.60	0.73±0.25

(a) Mean attenuated particle backscatter (β') integrated in the plume. β' is given only for cases with clear sky conditions persisting over at least 320 km.
(b) IVDR and color ratio are weighted by the length of the cross-section.

The dominant aerosol species in the model is sulfate (>80% of the total extinction), while dust accounts for most of the remaining extinction (see Figure 2.5). This is consistent with the low IDVR observed by CALIOP for this event. It is also consistent with the CALIOP aerosol

classification for the observed layers, with 60% of the layers classified as "clean continental", 20% as "dust", 10% as polluted continental, and 5% as smoke. In the model, Asian aerosol sources account for 40% of the total column AOD and 65% of the extinction within the plume.

2.3.2 12-19 March 2007 pollution export episode

2.3.2.1 Morphology and optical properties of the observed haze layers

The first haze layer of this second export episode was observed by CALIOP on March 12, 2007 at 17:59 UTC. Thirty-six other layers were observed over the following week, until March 19 (Table 2.2, Figure 2.6). The aerosol layers are initially detected at 70-82°N above the East Siberian sector of the Arctic, then slowly move towards the N. American sector remaining at a mean altitude of 3-4 km. The mean thickness of the layers is 3 km, with lengths ranging from 300 to 1400 km.

The depolarization ratio of these layers is often in excess of 0.06 (Table 2.2), indicating a strong dust component. We note that daytime (D) and nighttime (N) retrievals of IVDR and color ratio differ at 99% significance level, with nighttime values being systematically lower (IVDR:0.051 for N and 0.067 for D; color ratio: 0.25 for N and 0.32 for D, Table 2.2). Ice crystals may be responsible for the high depolarization ratio, but we rule out this possibility because the IVDR demonstrates remarkable constancy spatially and temporally, and the features persist for several days.

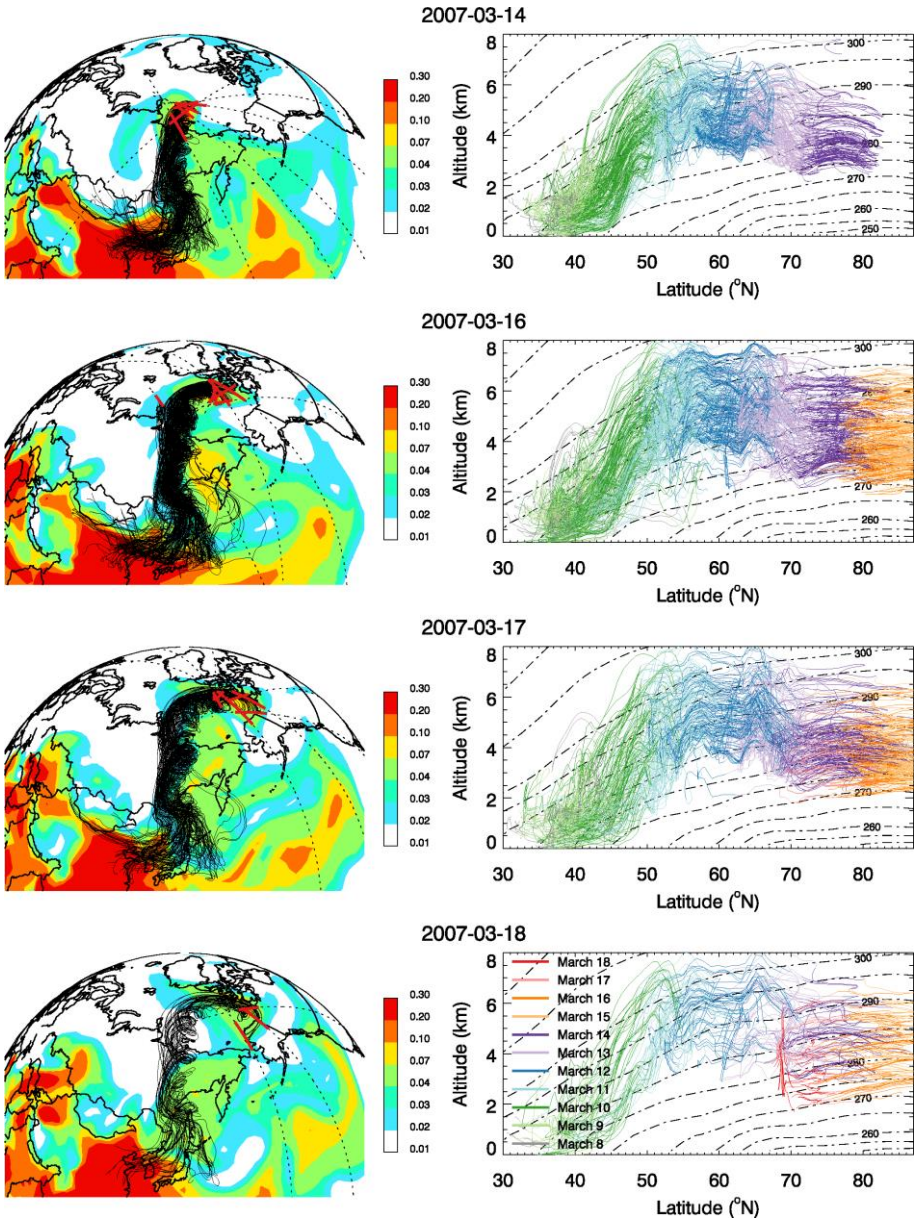

Figure 2.6: Same as Figure 2.1 but for March 14-18, 2007. The potential temperature contours (right panels) are zonally and temporally averaged in the longitude interval (110ºE, 160ºW) from March 9, 0Z until the time when the last plume was observed, for each day.

2.3.2.2 Meteorology

The event started with strongly descending northwesterly cyclonic flow from the Mongolian Plateau to the Sea of Japan on March 7-8 2007. This flow mobilized large amounts of dust, which

then mixed in with pollution aerosols from NE China and accumulated over the Sea of Japan. On March 10, 12 UTC (Figure 2.7, top panels), the GEOS-Chem model shows high Asian AOD values over the Sea of Japan. This is confirmed by observations from the MODIS instrument onboard Terra (not shown). The formation of a cyclone over the NE coast of China on March 10 (labeled C in Figure 2.7, right panels) led to the export of the pollution-dust mixture from the planetary boundary layer to the free troposphere. The 500 hPa geopotential heights show that a deep trough extended over NW China. On March 12 at 12 UTC an elongated region of enhanced AOD separates from the cyclonic circulation and is quickly en route to the Arctic, driven by the strong zonal geopotential height gradient between the Siberian trough and the pronounced Omega blocking high in the North Pacific (H in Figure 2.7, left panels).

Roughly half of all backtrajectories corresponding to the haze layers observed by CALIOP originated in the boundary layer. Of these 90% came from East Asia and 10% came from the Gobi desert (Figure 2.6). Ascent took place entirely outside the Arctic, predominantly during the early stages of the cyclone development on March 10 and 11; it was very intense with parcel rising to 4-8 km and precipitation reaching 4 mm/h (not shown). We compare the GEOS-Chem AOD over the source region (Yellow Sea and Sea of Japan) and the Arctic, inferring an export efficiency of ~10% for sulfate, 20% for BC, and 30-35% for dust. Compared to the previous case study, the sulfate export efficiency is lower (10% vs. 20%), likely due to the higher altitudes and thus more efficient scavenging encountered by these air parcels (Figure 2.6). Once the plume reached the Arctic, slow subsidence started at a rate of 0.6 cm/s. Parcel potential temperature decreased by 1.5-2 ºC/day as a results of radiative cooling and, possibly, turbulent mixing with the surrounding air.

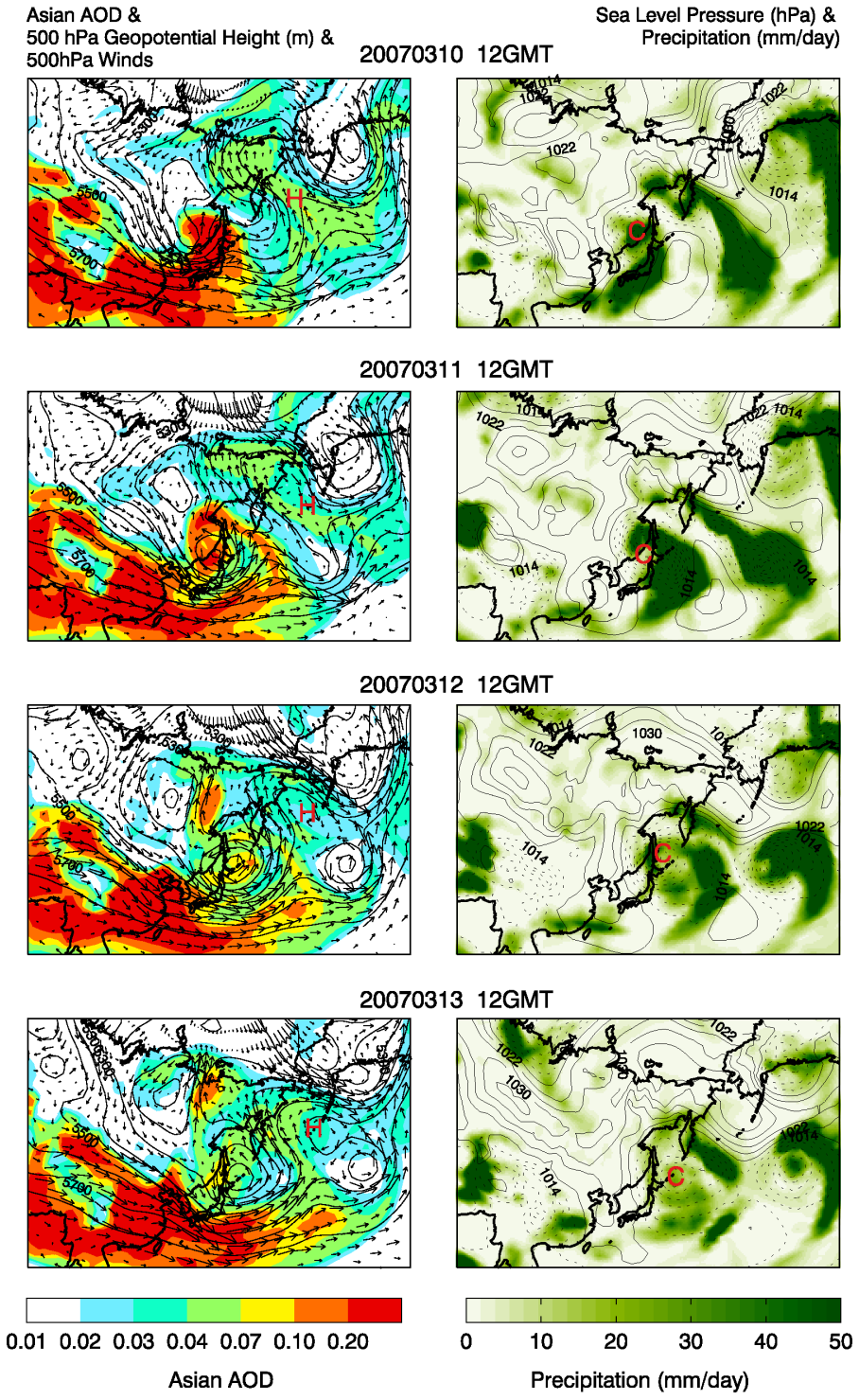

Figure 2.7: Synoptic situation during the initial stages of the export event of March 12-19, 2007. Conventions are the same as in Figure 2.3.

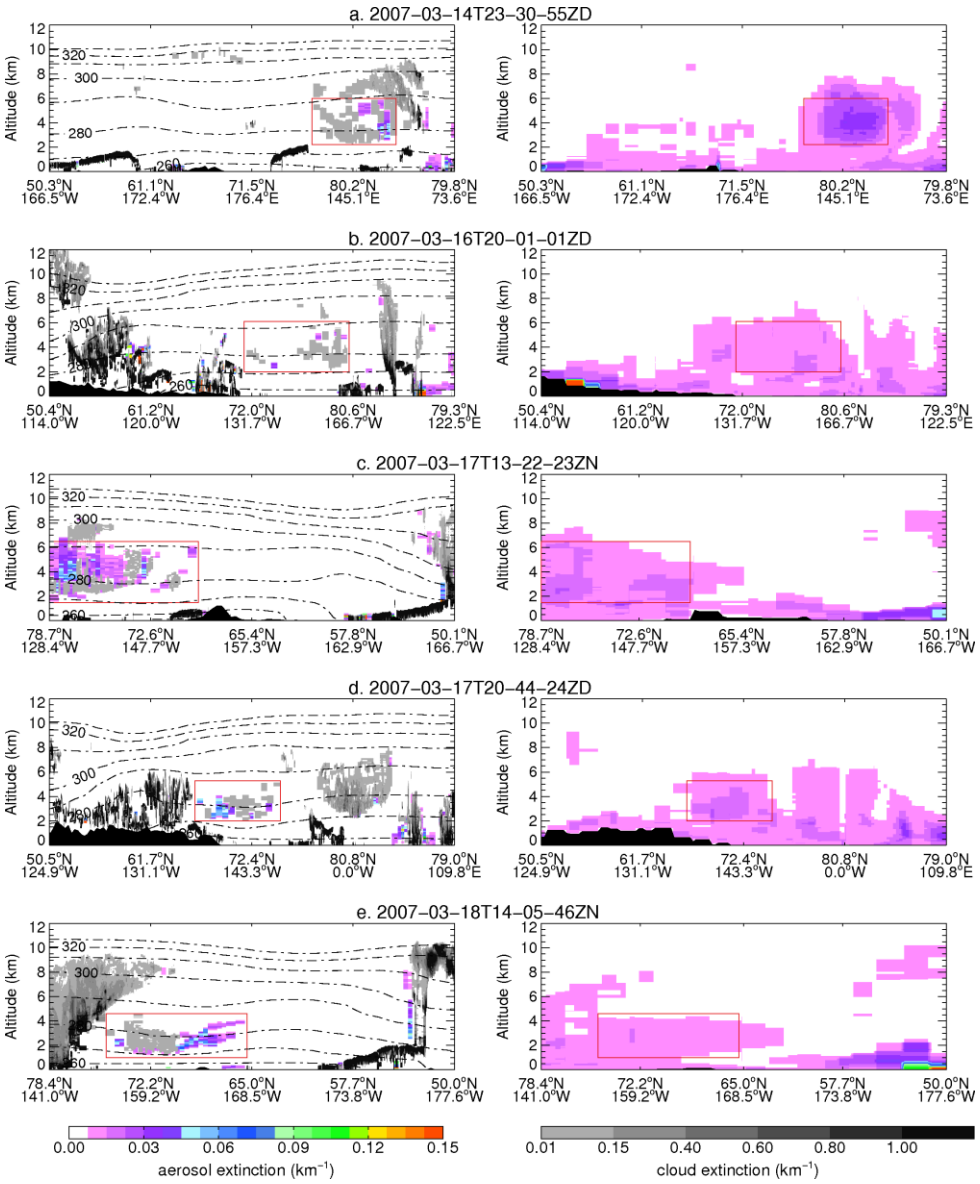

Figure 2.8: Same as Figure 2.2 for a subset of five major plume cross sections for the March 12-19 event. The red box delimits the aerosol plume cross sections, which are sometimes misclassified as clouds (see text).

2.3.2.3 Misclassification of aerosols as clouds

In this case, the haze layers with a high dust component are classified as clouds instead of aerosols in the CALIOP level 2 daytime products (Figure 2.8, panel a,b,d), but are correctly classified as aerosols in the nighttime retrievals (panels c,e). We believe that this erroneous classification is

caused by assumptions in the cloud/aerosol discrimination algorithm at high latitudes. Indeed, a feature is initially classified by the algorithm as cloud or aerosol based on the intensity of attenuated backscatter, color ratio and altitude (Liu et al, 2004). Then, aerosol layers with an IVDR value in excess of a given threshold are reclassified as clouds and denominated "CAD 101" (Liu et al., 2009). The IDVR threshold is latitude-dependent: 0.15 (50-60°N), 0.10 (60-70°N), 0.05 (70-82°N). The procedure was implemented to reduce misclassification of cirrus clouds and ice-crystal precipitation (also known as diamond dust) as aerosols (Liu et al., 2009). On March 12-17, the IVDR of aerosol layers observed by CALIOP range from 0.03 to 0.09 (Table 2.2), values which are common for winter/spring Arctic aerosols (Ishii et al., 2001). As IDVR often exceeds the 0.05 threshold, aerosol layers poleward of 70ºN are misclassified as cloud CAD 101. Thus, the same coherent aerosol feature is classified as either aerosol or cloud solely depending on its latitude (Figure 2.8, panel e). The misclassification is more frequent under daytime conditions (69% of the layers are misclassified) compared to nighttime conditions (32% of the layers are misclassified). The CAD 101 backtrajectories follow very closely the backtrajectories associated with correctly classified layers. Observations from the CloudSat satellite for the CAD 101 layers do not indicate any condensed water phase, further confirming the misclassification (not shown).

The most recent version of the CALIOP algorithm, v3.01, does not use the CAD 101 classification anymore, but instead incorporates latitude and depolarization ratio into a five dimensional probability density function (Liu et al., 2010). Relative to v2.01, fewer misclassification occur under nighttime conditions for this case study. However, daytime misclassification of aerosol layers as clouds persists.

2.3.2.4 Comparison between observed and modeled haze layers

There is good agreement between GEOS-Chem and CALIOP on the horizontal and vertical location of the plumes (Figures 2.6 and 2.8). The model shows that dust accounts for 20% of the AOD of this haze event. This is somewhat lower than expected based on the high IDVR observed by CALIPSO. We attribute this to a model underestimate of dust emissions during this event. Indeed, when compared to MODIS AOD observations over the Sea of Japan, where the dust/pollution mixture had accumulated at the onset of the transport event, GEOS-Chem is a factor of 2 too low.

Though we can compute GEOS-Chem mean plume AOD (0.052) we can not directly compare it to CALIOP because of the misclassification. Instead, we compare attenuated backscatter from the Level-1 profile data. We select all cloud free regions of the plumes (>320 km) listed in Table 2.2. We then average the attenuated backscatter profiles horizontally and smooth them with a running mean. We subtract the molecular attenuated backscatter from the measured attenuated profile, to obtain the particulate attenuated backscatter profile assuming a lidar ratio of 50 sr (Vaughan et al., 2004). In order to convert modeled extinction profiles into backscatter profiles we use the following lidar ratios: 70 sr for sulfate, BC, and organic carbon; 40 sr for dust; and 20 sr for sea salt (Winker et al., 2009). The extinction threshold is not applied in this case because we horizontally average the backscatter over a large domain, thus enhancing the signal-to-noise ratio.

The resulting attenuated aerosol backscatter (β′), integrated over the altitude interval where CALIOP observes the plume, are 1.21±0.60 for CALIOP and 0.73±0.25 for GEOS-Chem (Table 2.2). The model β′ is lower than observations by ~ 40%, which is consistent with a model underestimate of the amount of dust in the plume.

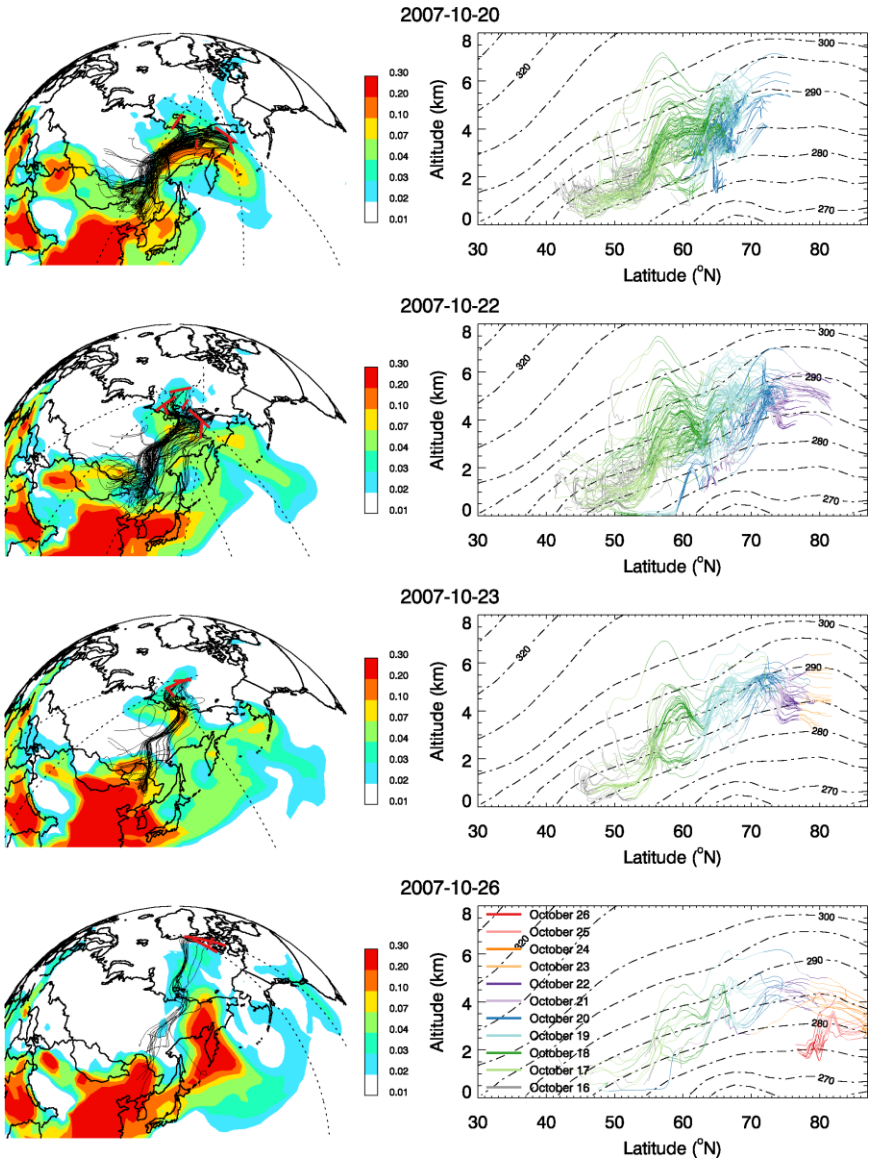

Figure 2.9: Same as Figure 2.1, but for the October 20-27, 2007 event. The potential temperature contours are zonally and temporally averaged in the longitude interval (100ºE, 180ºE) from October 17, 0Z until the time when the last plume was observed, for each day.

2.3.3 October 20-27 export episode

This last episode occurred in mid-autumn, a time that is not typically associated with elevated Arctic Haze levels. This is the time of the year when the Siberian anticyclone begins to build up at the end of the Monsoon season.

2.3.3.1 Morphology and optical properties of the observed haze layers

Figure 2.9 shows the location of the observed layers and their associated backtrajectories. The first plume cross section was observed above the northeastern Siberian sector of the Arctic. Part of the plume then traveled across the Arctic Ocean and it was last observed by CALIOP on October 27, near the Canadian islands of the Northwest Territories. The aerosol layers have a mean thickness of 1 km, and are initially observed at 3-5 km altitude, subsiding to 2-3.5 km after October 25 (Table 2.3). Values of IVDR and color ratio are very similar to those of the February case study, indicating pollution aerosols and low dust levels.

2.3.3.2 Meteorology

Figure 2.10 illustrates the synoptic situation during the export event. The ascent is associated with the early development of a mid-latitude cyclone triggered by a deep trough in the middle troposphere. A low-pressure center is seen at the surface on October 17, 2007 in the lee of the Yablonovyy mountain range, near the border between northeastern China and Russia (L in Figure 2.10, right panels). The build-up of the polluted airmass in the source area was favored by weak surface winds and anticyclonic conditions during the preceding two days. The aerosols were lifted up to the free troposphere and were carried northward along the downstream ridge. The backtrajectories (Figure 2.9) indicate that the aerosols original in NE China, with 4% of trajectories coming from the Gobi desert. Precipitation occurred during most of the transport; 50% of the precipitable water fell in the first 3 days (October 16-18), and 30-40% in the following four days (October 19-22), continuing more sporadically until October 25. For this event, we find export efficiencies of 13% for sulfate, 10% for BC, and 25-40% for dust in GEOS-Chem. These low export efficiencies for sulfate and BC are consistent with prolonged precipitation.

Table 2.3: Summary of the 21 Arctic aerosol layers observed by CALIOP during the October 20-27 export event. Refer to Table 2.1 for the legend.

		CALIOP					GEOS-Chem	
Date	Location of endpoints (Latitude; Longitude)	Length (km)	Mean Altitude (km)	IVDR	Color Ratio	AOD (plume | col.[b])	AOD w/o TH (plume | col.[b])	AOD w/ TH (plume | col.[b])
10-20 14.51 N	59.4ºN; 174.9ºE | 64.2ºN; 178.5ºE	560	3.0	0.030	0.29	0.07 | 0.07	0.03| 0.06	0.00| 0.00
10-20 16.30 N	64.5ºN; 154.0ºE | 66.9ºN; 156.3ºE	280	2.9	0.021	0.24	--[c]	--[c]	--[c]
10-20 18.09 N	70.9ºN; 136.8ºE | 76.0ºN; 147.9ºE	660	5.1	0.031	0.28	0.09 | 0.09	0.05| 0.07	0.02| 0.02
10-20 23.52 D	62.0ºN; 179.2ºW | 69.1ºN; 173.9ºE	840	3.5	0.029	0.34	0.07 | 0.07	0.02| 0.05	0.00| 0.00
10-21 17.13 N	70.6ºN; 150.2ºE | 73.8ºN; 155.9ºE	400	5.1	0.032	0.28	0.03| 0.03	0.02| 0.05	0.00| 0.00
10-21 18.52 N	72.1ºN; 127.8ºE | 78.6ºN; 147.6ºE	900	5.2	0.026	0.26	0.08| 0.08	0.05| 0.06	0.01| 0.01
10-22 00.35 D	67.0ºN; 165.5ºE | 74.1ºN; 154.4ºE	880	4.7	0.029	0.34	0.05| 0.05	0.02| 0.04	0.00| 0.00
10-22 02.14 D	72.9ºN; 132.3ºE | 75.3ºN; 126.6ºE	320	3.8	0.029	0.30	0.02| 0.02	0.02| 0.05	0.00| 0.00
10-22 16.17 N	64.1ºN; 156.7ºE | 69.6ºN; 162.7ºE	660	2.7	0.023	0.23	0.02| 0.02	0.02| 0.03	0.00| 0.00
10-22 17.56 N	74.8ºN; 147.5ºE | 77.7ºN; 156.9ºE	400	5.2	0.028	0.23	0.03| 0.03	0.02| 0.04	0.00| 0.00
10-22 19.35 N	73.5ºN; 119.9ºE | 79.2ºN; 139.8ºE	800	4.3	0.030	0.25	0.03| 0.03	0.03| 0.05	0.00| 0.00
10-22 21.14 N	80.8ºN; 129.1ºE | 81.6ºN; 172.5ºE	720	4.7	0.031	0.27	0.06| 0.06	0.03| 0.05	0.00| 0.00
10-23 01.18 D	76.1ºN; 138.2ºE | 78.6ºN; 128.2ºE	360	4.2	0.025	0.31	0.02| 0.02	0.01| 0.06	0.00| 0.01
10-23 20.18 N	78.5ºN; 125.2ºE | 81.8ºN; 169.4ºE	880	4.2	0.028	0.25	0.01| 0.01	0.04| 0.05	0.00| 0.00
10-23 21.57 N	81.4ºN; 164.6ºE | 81.7ºN; 134.7ºE	480	4.6	0.030	0.24	0.02| 0.03	0.03| 0.05	0.00| 0.00
10-25 13.30 N	79.4ºN; 127.2ºW | 81.2ºN; 64.4ºW	1120	2.9	0.036	0.25	0.04| 0.04	0.01| 0.03	0.00| 0.00
10-26 10.56 N	74.2ºN; 109.0ºW | 81.7ºN; 58.2ºW	1360	2.7	0.027	0.19	0.01| 0.01	0.01| 0.02	0.00| 0.00
10-26 12.34 N	77.7ºN; 122.7ºW | 81.8ºN; 77.6ºW	960	3.4	0.032	0.26	0.01| 0.01	0.01| 0.03	0.00| 0.00
10-26 16.38 D	76.2ºN; 92.1ºW | 80.2ºN; 112.9ºW	640	2.9	0.030	0.34	0.02| 0.02	0.01| 0.03	0.00| 0.00
10-27 17.22 D	61.4ºN; 81.4ºW | 73.4ºN; 95.8ºW	1440	2.2	0.042	0.31	0.06| 0.06	0.01| 0.03	0.00| 0.00
10-27 19.01 D	73.4ºN; 120.5ºW | 78.5ºN; 137.3ºW	720	2.4	0.031	0.22	0.04| 0.04	0.01| 0.04	0.00| 0.00
Mean[a]	--	730[a]	3.8[a]	0.030±0.004[a]	0.27±0.04[a]	0.041| 0.041[a]	0.022| 0.042[a]	0.002| 0.002[a]

(a) All mean aerosol properties given in the chart are weighted by the length of the cross-section.
(b) Column values are intended from 2-10 km, since low clouds obscure the surface during most scenes.
(c) Values are not given because the aerosol layer is completely overcast by clouds.

After October 25, the plume began to subside, following the spatially inhomogeneous pattern of low and high pressure systems over the Arctic. Backtrajectories indicate a steady cooling in potential temperature of ~1.5ºC/day, similar to the cooling rate recorded for the springtime export events.

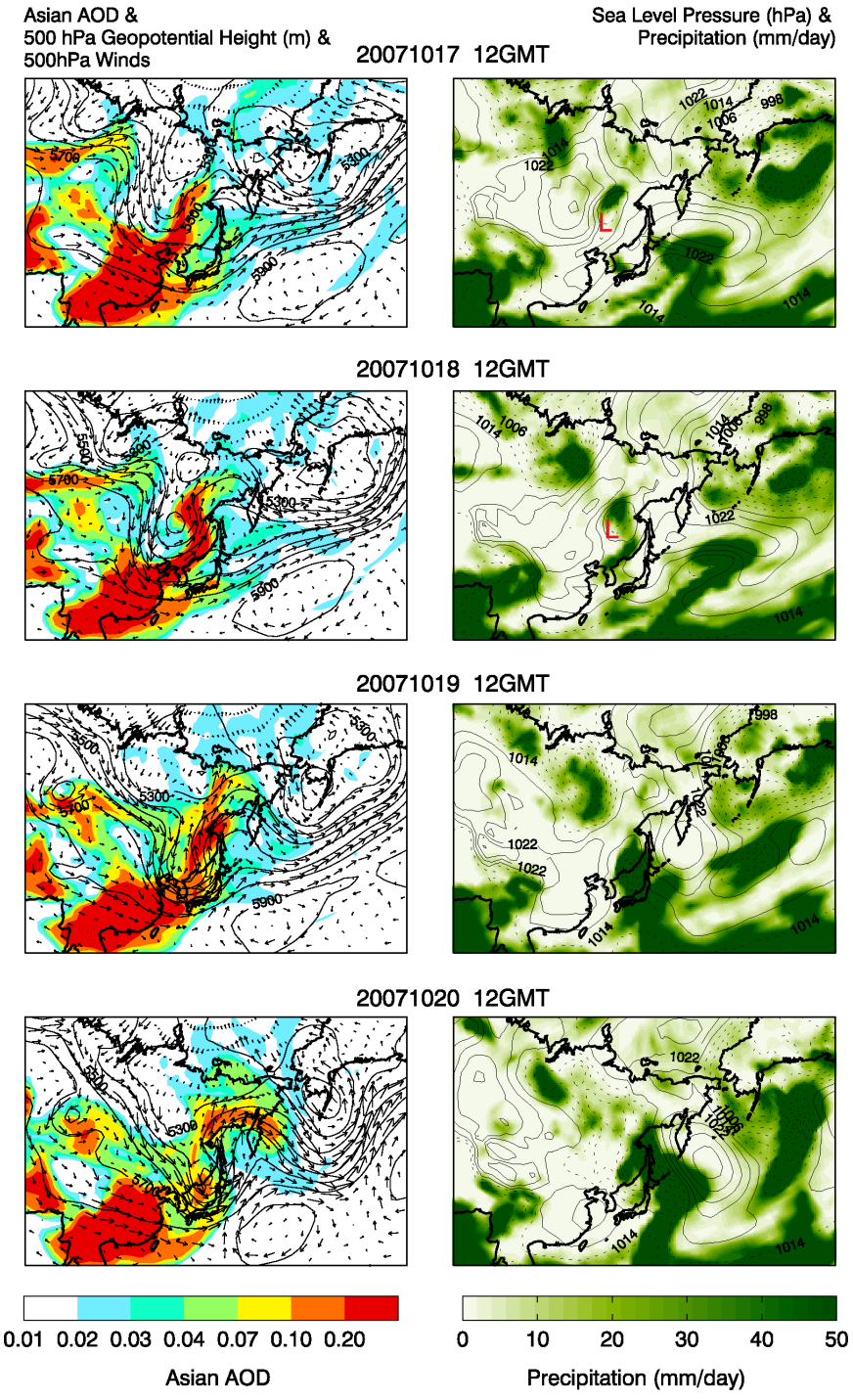

Figure 2.10: Synoptic situation during the initial stages of the export event of October 20-27. Conventions are the same as in Figure 2.3.

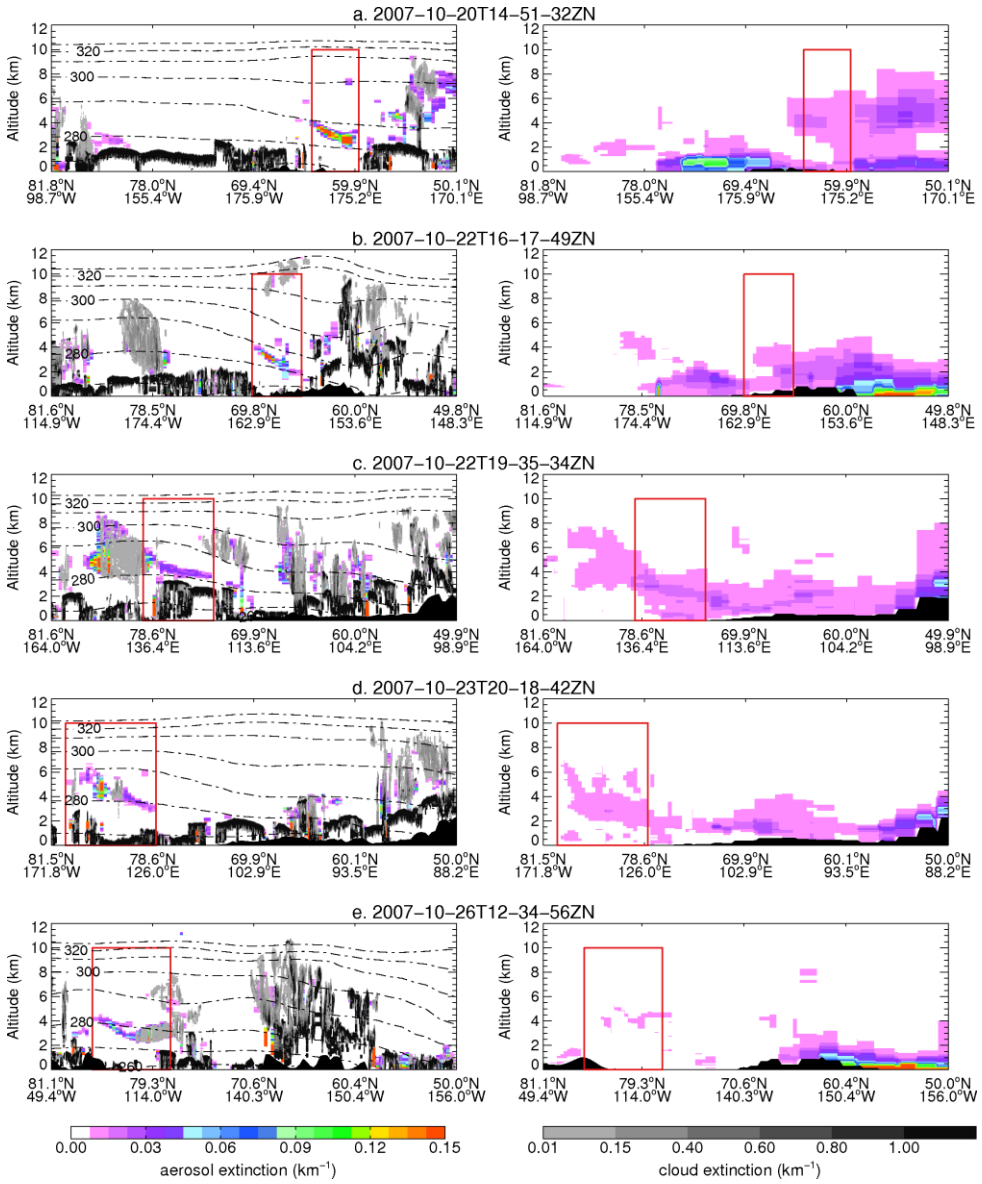

Figure 2.11: Same as Figure 2.2, for a subset of five major plume cross sections for the October 20-27 event.

2.3.3.3 Comparison between observed and modeled haze layers

Figure 2.11 shows five plume cross sections observed during this event. Ice clouds are often observed within the aerosol enhancement (panels b,c in Figure 2.11). The model generally reproduces the location of the aerosol layers throughout the 10-day duration of the event. Even 9-

10 days after the export began, the model is able to reproduce the thin aerosol layers in the Beaufort Sea, although the magnitude of the subsidence undergone by the plume seems to be underestimated (Figure 2.11, panels d and e). GEOS-Chem underestimates the observed extinction in the plumes (model AOD=0.022, observed AOD=0.04, Table 2.3). For the column AOD, we restrict our comparison to the 2-10 km altitude range because of extensive low level cloud cover. The resulting modeled 2-10 km AOD is 0.042, which compares well to the CALIOP column AOD of 0.04. However, if we apply the CALIOP sensitivity threshold to the model, the 2-10 km AOD decreases to 0.002 as the model values are often below the sensitivity threshold of CALIOP (Table 2.3). This is likely to be due to numerical mixing leading to excessive dilution over the course of this transport event. Indeed, Rastigejev et al. (2010) demonstrated that CTMs tend to dilute pollution plumes as a result of numerical diffusion and stretching of the plume in complex geophysical flow.

2.4 Discussion

In all three export events documented here, the initial phase of the transport was strongly meridional, confined between 120ºE-180ºE, with a weak or absent zonal component. Transport was rapid (3-4 days to reach the Arctic) and took place at 3-7 km altitude. These characteristics are consistent with the rapid transport pathway from East Asia described by Stohl (2006). Once in the Arctic, plumes generally travel slowly, and often migrate toward the northeast. In GEOS-Chem, the dominant aerosol component in the plumes is sulfate in all cases, representing 80% of the extinction. Dust accounts for 15-18% of the extinction, and BC for the rest. This is consistent with the CALIOP classification of the observed aerosols layers, with 75% being “clean continental”, 15% “polluted continental”, and the remaining 10% as “polluted dust” and “smoke”.

Intense precipitation took place in the initial phase of export for the two springtime cases. For the autumn case, precipitation occurred weakly during most of the transport to the Arctic. As

a result of these wet processes, we derived export efficiencies of 10-20% for sulfate, 10-20% for BC, and 30-40% for dust in GEOS-Chem. These values are consistent with the study of Park et al. (2005), who used aircraft observations in Asian outflow to derive an export efficiency at 4-6 km altitude of 6-21% for SO_x (SO_4^{2-} + SO_2) and 27-38% for BC. Sulfate is scavenged most efficiently during the initial strong uplift, while more BC survives this early phase when it is hydrophobic. Following Park et al. (2005), we assume a 1-day conversion timescale from fresh hydrophobic BC conversion to hydrophilic BC. Relative to sulfate and BC, dust displays the least scavenging as it is emitted at higher altitudes and latitudes in deserts of the Gobi, Takla Makan, and inner Mongolia regions (Shao and Deng, 2006).

Our case studies illustrate that in order for an Asian airmass to travel to the Arctic two conditions must be satisfied: 1) a lifting mechanism has to be present and, 2) a favorable synoptic pattern leading to meridional transport must persist for at least 3-7 days. Here, the lifting mechanism was associated with a low-pressure center accompanying the genesis or decay of a mid-latitude cyclone. Late winter and spring are the most active cyclogenesis periods in East Asia. NE China, with storm tracks originating in the lee of the Altai-Sayan mountains and along the East Asian coastline (Chen et al., 1991). In addition, meridional transport from Asia maximizes in winter/spring because of the frequent occurrence of blocking patterns in the 120ºE-150ºE longitude band (Barriopedro et al., 2006).

Figure 2.12 illustrates the 500 hPa geopotential height anomalies (left panels) and sea level pressure anomalies (right panels) corresponding to the first three days of transport for each case study examined here. In all three cases a positive anomaly in geopotential height and sea level pressure is located in the NW Pacific, accompanied by a negative anomaly over Eastern Siberia or Northern China.

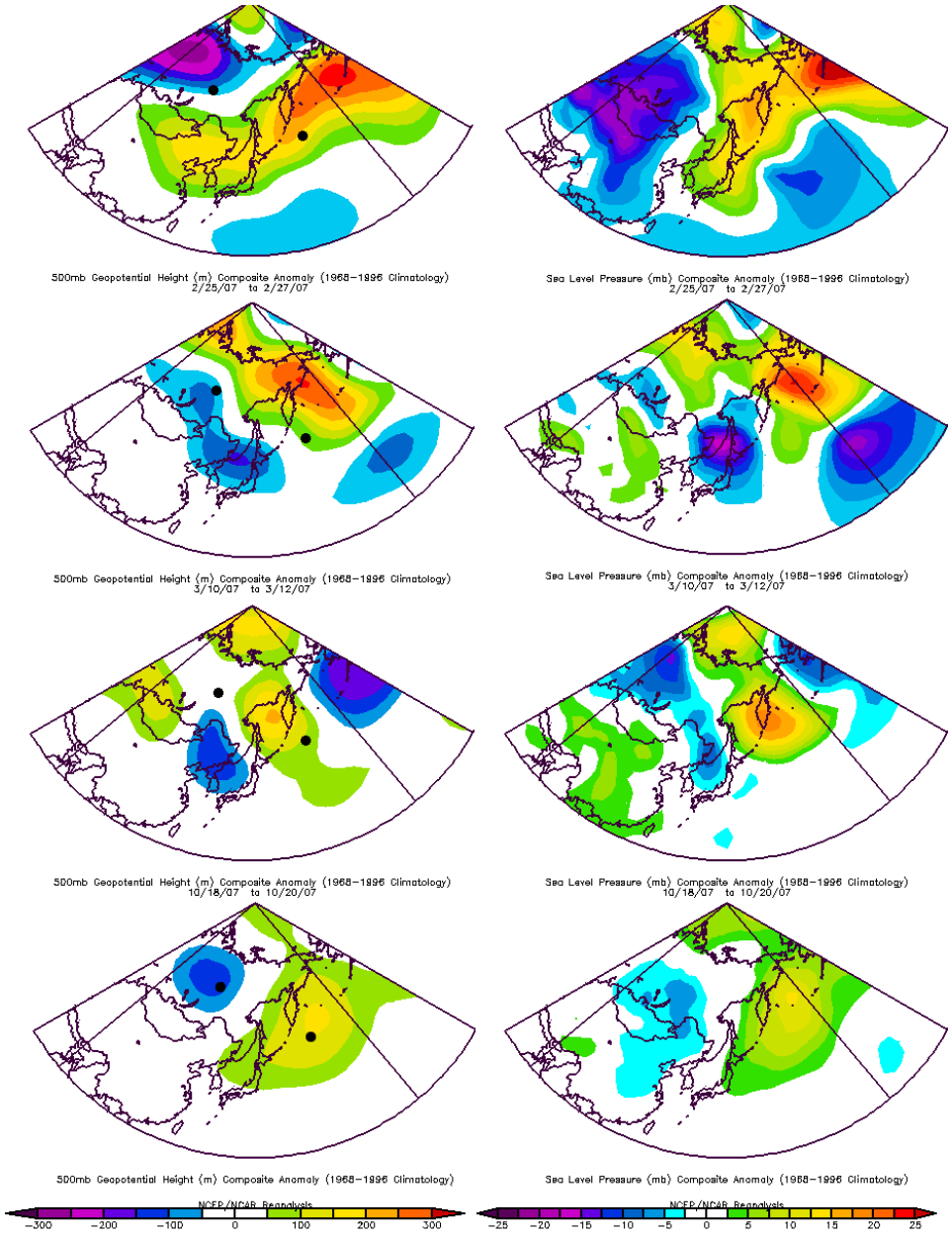

Figure 2.12: 500 hPa Geopotential height anomaly pattern (left panels) and Sea Level Pressure anomaly (right panels) for the 3-day initial stage of export to the Arctic of the three case studies discussed here: February 25-27, March 10-12, and October 18-20. Bottom panels: composite of all eleven episodes observed by CALIOP in 2007-2009. Two circles indicate the location of the two poles used to define the AME index. Images provided by the NOAA/ESRL Physical Sciences Division, Boulder Colorado from their Web site at http://www.esrl.noaa.gov/psd/.

The anomaly pattern for the two spring case studies shows a clear blocking configuration. The October case study displays a trough-ridge configuration. By inspection of the CALIOP 2008 and 2009 observations, we identified eight additional Asian export events (Table 2.4). These events display similar 500 hPa geopotential height anomalies, with either a blocking pattern or a trough-ridge configuration favoring poleward transport. By compositing all 11 events, we find a clear east-west dipole pattern in the anomalies (Figure 4.12, bottom panel).

Table 2.4: Sign of the WP and PNA indices during the early stages of the nine major events observed by CALIOP during the period 2007-2009.

Date[a]	WP[b]	PNA[b]	AME[b]
28 Feb. - 4 Mar, 2007	-	-	++
12 Mar.- 19 Mar, 2007	-	~0	++
20 Oct. - 27 Oct, 2007	~ 0	+	+
12 Mar. - 13 Mar, 2007	~ 0	+	+
14 Mar. - 17 Mar, 2008	+	~0	++
20 Mar. - 22 Mar, 2008	-	-	++
03 Dec. - 07 Dec., 2008	-	+	++
15 Dec. - 18 Dec., 2008	+	~0	++
22 Dec. - 25 Dec., 2008	+	-	++
14 Mar. -16 Mar., 2009	~0	-	++
20 Mar. - 27 Mar., 2009	-	~ 0	++

(a) The dates correspond to the times when Arctic haze events are observed by CALIOP.
(b) A double sign indicates absolute values of the index greater than two standard deviation during the 3-day initial phase of export. Near zero values are those whose absolute values within ±0.5 standard deviations.

Now, we examine how these anomaly patterns relate to atmospheric teleconnection indices, in particular the Western Pacific (WP) and the Pacific North American (PNA) indices, which are leading modes of low-frequency variability over the North Pacific (Wallace and Gutzler, 1981). Table 2.4 summarizes the sign of the WP and PNA indices during the initial stage of export for the eleven major episodes observed by CALIOP in 2007-2009. The WP index is negative in 5 out of 11 episodes, with near zero or positive values in the remaining 6 episodes. The PNA index is negative during 4 out of 11 events.

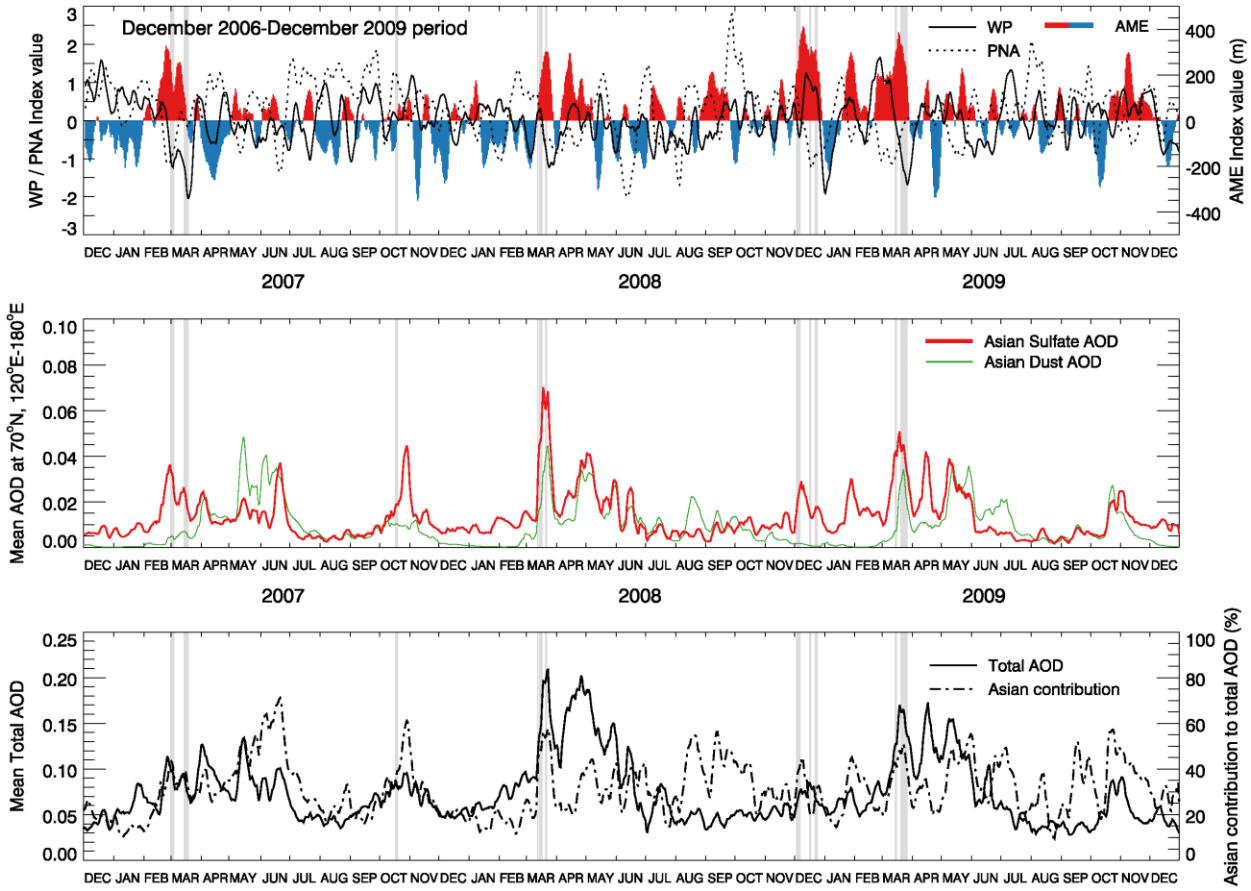

Figure 2.13: Time series of meteorological indices and Asian AOD for December 2006-December 2009. Top panel: WP, PNA, and AME (red=positive, blue=negative) indices. The WP index is based on Wallace and Gutzler (1981) and the PNA index is obtained from http://www.cpc.noaa.gov/products/precip/CWlink/daily_ao_index/history/history.shtml. See text for the definition of the AME index. A two-day lag is applied to all indices. Middle panel: Asian Sulfate and Asian Dust AOD calculated by GEOS-Chem at 70ºN averaged between 120ºE and 180ºE. Bottom panel: Total AOD at 70ºN averaged between 120ºE and 180ºE and fraction of the total contributed by Asia. All timeseries are smoothed with a 7-day running mean. The vertical grey bars show the 11 instances when CALIOP intercepted Asian plumes over the Arctic.

Three-year time series of daily WP and PNA index values are contrasted to the variability in Asian transport to the Arctic, which we define as the model Asian anthropogenic sulfate AOD at 70ºN averaged between 120ºE and 180ºE (Figure 2.13, top and middle panel). The WP index

displays little to no correlation with Asian Sulfate AOD, with correlation coefficients below 0.2 (Table 2.5). The PNA index shows more success at capturing the variability in the Asian Sulfate AOD time series, especially in winter and summer. The negative correlation coefficients in Table 2.5 are consistent with strong blocking activity in the central North Pacific occurring during negative phases of PNA (Wallace and Gutzler, 1981).

Table 2.5: Correlations of WP, PNA and AME index defined in the text with the Asian anthropogenic sulfate AOD at 70ºN averaged between 120ºE and 180ºE.

Seasons	Index[a]		
	WP	PNA	AME
DJF	-0.01	-0.45	**0.76**[b]
MAM	-0.08	-0.35	**0.63**
JJA	-0.19	-0.47	0.07
SON	0.17	-0.17	0.26
Entire timeseries (Dec 2006-Dec 2009)	-0.13	**-0.38**	**0.47**

(a) Timeseries are smoothed with a 7-day running mean. A 2-day lag is applied to all indices.
(b) Values in bold are significant at 95% confidence level.

We define a new empirical meteorological index by calculating the difference in 500 hPa geopotential height anomalies between two points (160ºE, 47.5ºN and 120ºE, 60ºN), near the east-west centers of action in the anomaly composites of Figure 2.12. We call this index the Asian Meridional Export (AME) index. All 11 events are associated with positive values of AME (Table 2.4, Figure 2.13). During winter and spring the AME index is strongly correlated with the anthropogenic Asian time series (r=0.76 and r=0.63, Table 2.5). The correlation of AME with the Asian anthropogenic AOD peaks at a lag of 2 days, which corresponds to the transport time from the mid-latitudes to 70ºN. The strength and persistence of meridional transport, as measured by

AME, captures 40-60% of the variance in the modeled Asian anthropogenic AOD at 70ºN in winter/spring. The AME index thus appears to be a good predictor of export of Asian pollution to the Arctic. During summer and autumn, the correlation between AME and Asian Sulfate AOD disappears as both time series display much less variability (Figure 2.13). This reflects a more zonal configuration of geopotential height with a diminished frequency of blocking patterns in the Northern Pacific in summer/early autumn (Lejenas and Økland, 1983), leading to reduced outflow of pollution from East Asia to the Arctic.

Finally, we use the GEOS-Chem model to examine Asian export to the Arctic in a broader context. We find that 6 major export episodes occur each year, with half these events taking place between March and June, in phase with positive values of the AME index (Figure 2.13). Sometimes, events occur in winter (February 2007, December 2008, January 2009) and autumn (October 2007 and 2009). Transport during spring events takes place at 4-8 km altitude, while it is restricted to altitudes below 2 km during winter. Winter and early spring episodes are dominated by sulfate, with dust making a significant contribution in late spring to early summer, consistent with the seasonality of Asian dust storms (Shao and Deng, 2006). In some export events, the contribution from Asian dust can exceed that of Asian sulfate. Over the Siberian sector, Asian sulfate and dust account for 33% of the total AOD in GEOS-Chem, on average (Figure 2.13, bottom panel). During major transport episodes, the Asian contribution increases to 50-70%, with a constribution increasing with altitude: 55-75% at 2-5 km altitude and 60-80% at 5-10 km.

2.5 Conclusions

We used observations from the space borne lidar onboard CALIPSO satellite together with the GEOS-Chem chemical transport model, and lagrangian backtrajectories to follow the evolution of three aerosol export events from East Asia to the Arctic in 2007. Two of the export episodes took

place in early spring, the time when Arctic Haze is at its climatological peak, whereas the third occurred in autumn. Haze layers were detected at altitudes of 2-8 km, exhibited a poleward tilt following potential temperature surfaces. Individual layers had a mean thickness of ~1.5 km. We found good agreement between model simulations and observations as to the geographical location, thickness, and altitude of the haze layers.

The mean observed optical depth of aerosol layers was 0.04 (cases 1 and 3) with depolarization ratio consistently around 0.03; in the second springtime case the AOD was not available due to the misclassification of aerosols as clouds. In this case, we found a mean integrated attenuated backscatter of 1.21×10^{-3} sr^{-1}, and higher values of the depolarization ratio, in the 0.05-0.07 range. Values of color ratio are found to be mostly between 0.2 and 0.3 in all cases.

The dominant source region for the aerosol layers is NE China. In 5-10% of the individual aerosols layers, backtrajectories indicate an origin in the Gobi desert. The export pathway followed by the mixture of pollution and dust was similar in all three case studies. Pollutants first accumulated in the shallow boundary layer and were then exported to the free troposphere by a developing cyclone or a waning cyclone approaching from the west. The polluted airmass then ascended rapidly ahead of the cold front, accompanied by significant precipitation in these early stages of transport. This was followed by rapid meridional transport to the Arctic mediated by either a blocking high in the western Pacific (spring export events) or a pronounced ridge (autumn export event). Once the ascent was complete, potential temperature slowly but steadily decreased at a rate of ~1.5ºC/day. Subsidence accompanied this radiative cooling, although it took place less gradually. No plume was observed to reach the surface.

In the export episode that took place in March, the CALIOP layer classification algorithm misclassifies a large number of aerosol layers as clouds. The misclassification occurs because the

presence of dust poleward of 70ºN is interpreted as ice crystals by the algorithm. The misclassification is more pronounced for daytime compared to nighttime retrievals.

We examined the relationship between the Western Pacific and Pacific North American indices and the frequency of occurrence of major aerosol export episodes from East Asia. While the WP index shows no correlation with export episodes, the PNA index displays a negative correlation, consistent with strong blocking activity occurring during negative phases of the PNA.

We defined an empirical index, the Arctic Meridional Export (AME), based on a composite of the anomaly pattern of 500 hPa heights of 11 major export events in 2007-2009. AME correlates well with enhanced export of Asian pollution to the Arctic during winter (r=0.76) and spring (r=0.63), and is thus more successful than the PNA and WP indices at capturing the variability of these export events.

Simulations with the GEOS-Chem model showed that 6 major export events from Asia to the Arctic occur each year. These events maximize during March-June, with a secondary maximum in October-November. The AOD contribution of Asian pollution and dust aerosols increases to 50-70% during these events, compared to a mean background contribution of 33%.

CALIOP measurements provide a potential method of resolving the discrepancies among CTMs in that it can provide constraints on the vertical location and amount of aerosols transported to the Arctic. The model calculated plume AOD and backscatter fall within the uncertainties range of the CALIOP measurements (±40%). The sharper boundaries of the aerosol layers observed by CALIOP are partly a result of the altitude dependent sensitivity of the instrument. The CALIOP detection accuracy however is sensitive to the illumination conditions which affect the signal-to-noise ratio. Our case studies took place under favorable conditions for retrievals, since the transport was rapid (and consequently the plumes underwent little dilution), and occurred mainly at

nighttime. As the sun rises over the Arctic it becomes more problematic to detect faint pollution aerosol plumes transported over long distances and to track them over time. This aspect has to be carefully considered if one aims at constructing a satellite-based long-term climatology of the vertical distribution of haze layers over the Arctic.

Chapter 3

SPATIAL AND SEASONAL DISTRIBUTION OF ARCTIC AEROSOLS OBSERVED BY THE CALIOP SATELLITE INSTRUMENT (2006-2012)

This chapter was published in Atmospheric Chemistry and Physics under the title:

Di Pierro, M., Jaeglé, L., Eloranta, E. W., and Sharma, S.: Spatial and seasonal distribution of Arctic aerosols observed by the CALIOP satellite instrument (2006–2012), Atmos. Chem. Phys., 13, 7075-7095, doi:10.5194/acp-13-7075-2013, 2013.

3.1 Introduction

Transport of anthropogenic aerosols to the Arctic has been studied since the early 1980s (e.g., Rahn and McCaffrey, 1980; Barrie et al., 1981; Rahn, 1981) and leads to the phenomenon of Arctic Haze, the human-caused reduction in visibility at high latitudes. Arctic Haze is characterized by a marked seasonal cycle in aerosol concentrations at the surface, with a maximum in winter/early spring and a minimum in summer (Law and Stohl, 2007; Quinn et al., 2007). The winter/spring maximum is due to enhanced transport combined with weaker removal in the Arctic (Shaw, 1995). The summer minimum has been attributed to the isolation of the Arctic atmosphere caused by reduced transport from mid-latitudes at this time of year (e.g., Stohl, 2006), although recent studies have highlighted the importance of efficient summertime wet removal processes over the Arctic (Garrett et al., 2011; Bourgeois and Bey, 2011; Browse et al., 2012).

Considerable effort has been devoted to understanding the sources and transport pathways of Arctic pollution. Transport of pollution aerosols from Europe and the Former Soviet Union (FSU) was the main source of Arctic aerosols in the 1980s (Rahn and Lowenthall, 1984; Raatz and Shaw, 1984; Barrie et al., 1989). However, since the first source-attribution studies were conducted, the geographical distribution of the emission of aerosols from fossil-fuel combustion has changed dramatically (Novakov et al., 2003). Sulfur emissions in Eastern Europe and Russia have been decreasing following the introduction of cleaner combustion technologies in Europe and the demise of the FSU, whereas East and South Asian emissions have increased over the past 30 years, driven by rapid economic growth and higher energy consumption (Stern, 2005). Ground-based measurements of sulfate aerosol concentrations in March/April have decreased by 27-63% between 1990 and 2003 across a range of Arctic sites, and appear to have leveled off (Quinn et al., 2007). This negative trend has been attributed to the decrease in anthropogenic emissions from Eurasia (Quinn et al., 2009; Gong et al., 2011; Hirdman et al., 2011). Recent modeling studies show that despite declining emissions, Europe and Russia continue to constitute the largest contributors of Arctic sulfate and black carbon (BC) aerosols at the surface (Shindell et al., 2008), due to their vicinity and favorable transport patterns to the Arctic (Stohl, 2006). Measurements of BC in snow across the Arctic (Hegg et al., 2010) as well as modeling simulations (Wang et al., 2011) suggest a large contribution from agricultural biomass burning during spring.

The 2008 International Polar Year (IPY) saw a suite of coordinated aircraft campaigns aimed at improving the understanding of the factors controlling changes in Arctic atmospheric composition and climate. The National Aeronautics and Space Administration (NASA) Arctic Research of the Composition of the Troposphere from Aircraft and Satellites (ARCTAS) campaign occurred in April (ARCTAS–A) and July (ARCTAS-B) of 2008 over the North American Arctic

(Jacob et al., 2010). The spring campaign was conducted in parallel with the National Oceanic and Atmospheric Administration (NOAA) Aerosol Radiation and Cloud Processes affecting Arctic Climate (ARCPAC) campaign (Brock et al., 2011). During these springtime campaigns, several dense biomass burning plumes from agricultural and forest fires in Russia were sampled over the Alaskan and Canadian Arctic (Warneke et al., 2009; Fisher et al., 2010). Source attribution studies have determined that fossil fuel burning in East Asia was the dominant source of pollution during ARCTAS-A, representing roughly 40% of Arctic CO at all altitudes (Fisher et al., 2010; Bian et al., 2013), although European and Russian sources also contributed significantly at low altitudes (30%). Wang et al. (2011) reported that sulfate aerosols contributed to 50-70% of aerosol mass, with organic aerosols accounting for another 30-40% at all altitudes. Fisher et al. (2011) found that the single largest source of sulfate aerosols at the surface is central Russia and Kazakhstan in winter-spring, whereas East Asia contributes the most above 5 km. The modeling study of Bourgeois and Bey (2011) indicates that Europe and Siberia dominate the annual budgets of column BC and sulfate aerosols. Biomass burning events systematically affect the springtime aerosol budgets and background concentration levels and April 2008 stands out as characterized by unusually high fire activity (Warneke et al., 2010). Brock et al. (2011) observed that the seasonality of Arctic haze is driven by changes in the background aerosols concentration rather than the frequency of occurrence of dense smoke layers.

The summer 2008 IPY measurements showed that the East Asian contribution to Arctic CO and aerosols was small, indicating inefficient transport as well as enhanced wet scavenging of aerosols (Matsui et al., 2011; Bian et al., 2013). Despite high plume dilution and stronger wet removal in summer, several aerosol plumes were traced to both fossil fuel and biomass burning origins, and all showed a preponderant component of highly oxygenated organic carbon

compounds (>70%) with relatively larger sulfate fractions for plumes originating in industrialized regions (Schmale et al., 2011).

In addition to fossil fuel and biomass burning sources, the Arctic aerosol budget is also influenced by natural sources. Thin lofted layers of mineral dust were documented as early as the 1970s (Rahn et al., 1977). Greenland ice-core records spanning the recent past (1790-2000) show large spikes of deposited sulfate associated with episodic explosive volcanic eruptions (McConnell et al., 2007). These ice cores also show that biomass burning constitutes a significant, though highly variable, source in summer.

Pollution enters the Arctic following different pathways determined by the persistence and seasonality of large-scale circulation patterns. Carlson (1981) and Iversen (1984) introduced the concept of Polar Dome, a dome-shaped closely packed set of constant potential temperature surfaces (isentropes) wrapped around the Arctic. As transport within the Arctic tends to occur at near-constant potential temperature, the Polar dome forces air aloft to follow the isentropes, effectively acting as a surface barrier to intrusions of air from outside. However, during winter considerable diabatic cooling may occur in an air mass in contact with cold, snow-covered surfaces (Klonecki et al., 2003), thus trapping aerosols below the temperature inversion and allowing their transport over long distances. This is a common low-level pollution transport pathway from Eurasia in winter and early spring.

Transport aloft requires that gaseous and aerosol pollutants first be injected from the planetary boundary layer into the free troposphere and is thus more episodic. Warm conveyor belts in mid-latitude cyclones constitute such a mechanism, but are accompanied by considerable wet scavenging. Free tropospheric transport via this pathway dominates the total transport from North

America and East Asia because of the lower latitudes and higher potential temperatures of these regions compared to sources located in Europe and Russia (Klonecki et al., 2003; Stohl, 2006).

Although surface observations span more than 3 decades at a few sites such as Barrow (Alaska), Alert (Canada) and Karasjok (Norway), the Arctic aerosol burden is not well characterized in space and time (Quinn et al., 2007). Aircraft campaigns provide a snapshot of the detailed vertical distribution of Arctic aerosols, but only over a limited time-period and region. For example, airborne measurements of aerosol properties were conducted during the Tropospheric Ozone Production about the Spring Equinox Experiment (TOPSE) from February to May 2000 over the North American Arctic (Browell et al., 2003; Scheuer et al., 2003). The measurements highlighted the strong spatial inhomogeneity of Arctic aerosol mixing ratios and documented a steady increase in number concentration in the middle-upper troposphere throughout the campaign, providing indications that the annual aerosol maximum occurs later aloft than at the surface.

The SAGE II and III satellite instruments used solar occultation to retrieve aerosol extinction in the Arctic troposphere above 6 km altitude (Treffeisen et al., 2006). An April-May aerosol extinction maximum was observed in the upper troposphere, followed by a rapid drop in mid-summer to much lower values. Thus SAGE provided the first multi-year dataset of Arctic aerosols in the upper troposphere. However, SAGE retrievals were not available in the middle and lower troposphere because of limitations associated with the presence of clouds along the long horizontal line of sight of the instrument.

The NASA and Centre National d'Études Spatiales (CNES) Cloud-Aerosol Lidar and Infrared Pathfinder Satellite Observation (CALIPSO) satellite joined the A-train polar-orbiting constellation on April 28, 2006 and began collecting data in June 2006 (Winker et al., 2009).

CALIPSO carries the Cloud-Aerosol Lidar with Orthogonal Polarization (CALIOP) instrument, which measures the attenuated backscatter at 532 nm and 1064 nm with a vertical resolution of 30 to 60 m. Because it is an active remote sensing instrument, CALIOP can retrieve aerosol and cloud profile information during both daytime and nighttime, and, unlike passive remote sensing instruments, it is not affected by the highly reflective surfaces present in the Arctic. Thus, CALIOP has the potential to provide a wealth of information on the vertical and horizontal distribution of Arctic aerosols. Two limitations of CALIOP are its narrow footprint (~100 m) and its relatively low sensitivity to faint aerosol layers that frequently occur over the Arctic.

CALIPSO has been used in the Arctic to follow the evolution of aerosol plumes over timescales of 4-10 days (deVilliers et al., 2010; Di Pierro et al., 2011) and in conjunction with the CloudSat satellite to study the optical properties of mixed-phase and ice clouds and haze (Gayet et al., 2009; Grenier et al., 2009). Devasthale et al. (2010) present a 4-year CALIPSO-based study of the spatial distribution of Arctic aerosols. They find that the largest fraction of the detected aerosol layers occurs below 1 km and maximizes in winter (65%), due to the development of strong surface-based temperature inversions, whereas in spring and summer a relatively larger fraction of aerosol layers is detected in the free troposphere. The occurrence of smoke aerosol, associated with biomass burning, reaches an annual maximum in the summer (13% of total aerosol layers) and is below 5% in all other seasons.

In this study, we examine the ability of CALIOP to provide information on the horizontal and vertical distribution of Arctic aerosols for 2006-2011. Our study however differs from that of Devasthale et al. (2010) in that we provide an analysis of the seasonal evolution of aerosol extinction. We account for the different performance of the CALIOP instrument when it operates under daytime and nighttime conditions. Furthermore we compare CALIOP retrievals to both

ground-based and aircraft-based measurements to evaluate the robustness of CALIOP measurements over the Arctic. In Section 2 we present a description of the CALIOP dataset. Section 3 documents a detailed comparison of CALIOP retrievals against surface and aircraft in situ measurements of aerosol extinction over the Arctic as well as against ground-based lidar retrievals of aerosol backscatter. This is followed by a discussion of the horizontal, vertical and temporal variations of Arctic aerosol extinction in 2006-2012 (Section 4). Finally, section 5 presents our conclusions.

3.2 Space-borne CALIOP lidar

CALIOP measures the attenuated backscatter intensity at 532 nm and 1064 nm. The 532 nm channel is polarization-sensitive, allowing the measurement of the two orthogonally polarized components of the signal. From the measured signal, which after geolocation and calibration is denominated Level-1, a series of nested algorithms find atmospheric features at increasing horizontal averaging (Winker et al., 2009; Young and Vaughan, 2009). These features are then classified as clouds or aerosols, and their sub-type (clean continental, clean marine, dust, polluted continental, polluted dust and smoke) is determined. Liu et al. (2009) describe the cloud/aerosol separation algorithm and assess its performance. Omar et al. (2009) describe the aerosol type classification algorithm. The inversion to obtain the AOD at both wavelengths is then initiated by assigning an extinction-to-backscatter ratio (called lidar ratio), as a function of the aerosol type. The resulting data product is called Level-2.

The CALIOP 532 nm Version 3.01 calibration has been validated against aircraft measurements by the NASA Langley Airborne High Spectral Resolution Lidar (AHSRL) instrument for a wide seasonal and latitude range covering diverse aerosol and cloud conditions (Rogers et al., 2011). CALIOP's attenuated backscatter shows a very small negative bias relative

to AHSRL both at nighttime (-2.7% ± 2.1%) and daytime (-2.9% ± 3.9%) but lies within the uncertainties of AHSRL (Rogers et al., 2011). No seasonal, latitudinal or vertical dependencies were found. Over the Arctic, CALIOP attenuated backscatter values were within 10% of AHSRL measurements for all validation flights.

An important aspect of CALIOP's performance is its sensitivity to illumination conditions. Daytime retrievals are less accurate than nighttime retrievals because they are affected by the noise from scattering of solar radiation in the field of view of the detector (Winker et al., 2009; Rogers et al., 2011). Daytime retrievals thus have a higher backscatter sensitivity threshold (~0.5 Mm^{-1} sr^{-1} at sea level) compared to nighttime retrievals (~0.4 Mm^{-1} sr^{-1}). Both thresholds decrease exponentially with altitude (Winker et al., 2009, 2013), such that at 8 km altitude their values are ~0.3 Mm^{-1} sr^{-1} and ~0.2 Mm^{-1} sr^{-1} for daytime and nighttime respectively. Over the Arctic, especially in the middle and upper troposphere, thin aerosol layers often have backscatter values below these thresholds and can thus go undetected by CALIOP. The difference in sensitivity between day and night leads to complications in the interpretation of spring and summer retrievals over the Arctic when only daytime measurements are available from CALIOP. We address this issue in more detail in section 3.2.3.

In this study, we use version 3.01 Level-2 Cloud and Aerosol Layer data at 5 km horizontal resolution between June 2006 and October 2011. Between November 2011 and May 2012, we use version 3.02. No differences in the inversion algorithm were introduced between the two versions. The CALIPSO orbit inclination of 98.2° provides coverage up to 81.8°N latitude. We grid the daily CALIOP Level-2 5 km orbit segments onto a 2° latitude by 2.5° longitude horizontal grid for all latitudes poleward of 59°N, with 200 m resolution in the vertical. For each grid-box we calculate the aerosol detection frequency (*f*), which is the ratio of the number of detected layers over the

sum of detected layers and clear air. We also extract the backscatter (β) and extinction (b_{ext}) of the detected layers along with their standard deviation. The "gridded extinction", $\overline{b_{ext}}$, is then defined as the product between the aerosol detection frequency and the extinction of the detected layers, $f \times b_{ext}$. The "gridded backscatter", $\bar{\beta}$, is defined similarly as $f \times \beta$. We will refer to these two gridded products as the standard extinction and backscatter.

This gridding approach assumes that all layers that are undetected by CALIOP (clear air) have an extinction of 0 Mm^{-1}. The same approach was used by Winker et al. (2013), who notes that this assumption likely leads to an underestimate of the true extinction as undetected aerosol layers could have an extinction between 0 Mm^{-1} and the CALIOP detection threshold. This approach thus yields a lower bound estimate of the true extinction. An alternative approach would be to assign to clear air extinction values equal to the CALIOP detection threshold. This would result in an upper bound estimate. We will examine the impact of these assumptions in section 3.3.

3.2.1 CALIOP data selection

We screen the data by selecting only aerosol retrievals with an absolute value of the cloud aerosol distinction (CAD) confidence function greater than 50. CAD values measure the confidence in the algorithm classification of an atmospheric feature as either a cloud or an aerosol (Liu et al., 2009). CAD values vary between -100 for a feature that is unambiguously classified as an aerosol layer to +100 for a feature that is unambiguously classified as a cloud layer. We found that using larger CAD threshold values (up to |CAD|=90) does not affect our results significantly. We apply a further screening by using the Quality Control (QC) flag and exclude aerosol retrievals that yield unphysical solutions or where the retrieval algorithm had to adjust the initially selected lidar ratio. In these cases the retrieved extinction is not accurate and the uncertainty cannot be estimated

(Winker et al., 2009; Young and Vaughan, 2009). We also exclude aerosol layers with unrealistically high extinction values (>500 Mm^{-1}).

In Version 3.01 an underestimate of aerosol extinction at low levels present in data Version 2 was corrected by extending the aerosol layer base to 90 m above the surface. However this correction leads to unrealistically low extinction at the surface (Koffi et al., 2012). To correct this artifact we apply the same correction as in Koffi et al. (2012) by further extending the lowest aerosol layer to the surface if the height above the surface is less than 10% of the layer thickness.

Clouds are generally optically thicker than aerosols and can significantly, if not completely, attenuate the lidar signal and thus reduce CALIOP's ability to detect faint features below them. In our study we consider both cloud-free CALIOP profiles, as well as profiles above the highest cloud top detected. In a recent study, Yu et al. (2010) used an alternate cloud screening method, considering cloud-free profiles and allowing thin cirrus (optical depth <0.1) with cloud base greater than 7 km. Using one year of observations we compared results following our approach ("above clouds") to the Yu et al. (2010) approach. We find that the two selection methods yield gridded extinctions that are within 10% at all altitudes, but our "above clouds" approach allows us to retain 3 times as many CALIOP layers between 3 and 8 km. In order to increase the number of CALIOP observations, our results will be based on the "above clouds" selection method.

3.2.2 Diamond dust screening

During the months of December-February, we found that 5% of the time CALIOP retrieved very high values of aerosol extinctions (>300 Mm^{-1}) poleward of 70°N and below 2 km altitude. This distribution is consistent with the reported frequency of occurrence of diamond dust (Intrieri et al., 2004). These anomalously high extinction occurrences could thus be associated with the misclassification of diamond dust as aerosol in the CALIOP retrieval algorithm. The CALIOP

feature classification algorithm employs the measured depolarization ratio to help discriminate between clouds and aerosols and is designed to classify diamond dust as 'cloud'. However, mixtures of aerosols with small quantities of ice crystals are not infrequent (Bourdages et al., 2009) and can exhibit low depolarization ratios but elevated backscatter returns (Hoff, 1988). Under these circumstances the depolarization ratio may be ineffective in helping to correctly identify diamond dust. We eliminate these diamond dust events misclassified as aerosols by removing aerosol layers with extinction values greater than 350 Mm^{-1} occurring below 2 km between September and May. This results in discarding fewer than 4% of aerosol layers.

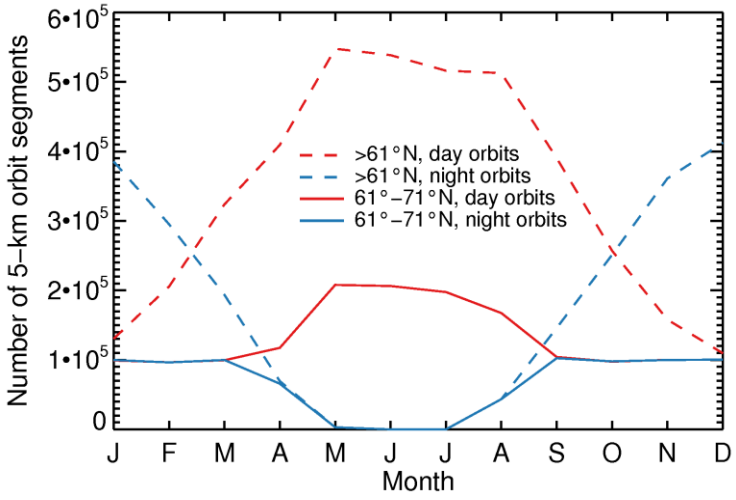

Figure 3.1: Number of CALIOP 5-km orbit segments as a function of month for the year 2007. Blue lines indicate nighttime retrievals, whereas red lines are for daytime. Solid lines correspond to the latitude interval 61°-71°N and dashed lines are for the region poleward of 61°N.

3.2.3 Combining daytime and nighttime data

Figure 3.1 shows the seasonal variation in the number of 5-km orbit segments over the Arctic (poleward of 65°N) along the night and day sides of CALIOP's orbit. Daytime orbit segments dominate between March and September, with no nighttime observations at all in May, June and

July. If we restrict the orbit segments to the lower Arctic (61-71°N), we find that over a 7-month period (September to March) the number of CALIOP daytime and nighttime orbit segments is the same. We choose this latitude band to compare daytime and nighttime aerosol retrievals for 2006-2012, as shown in Figure 3.2.

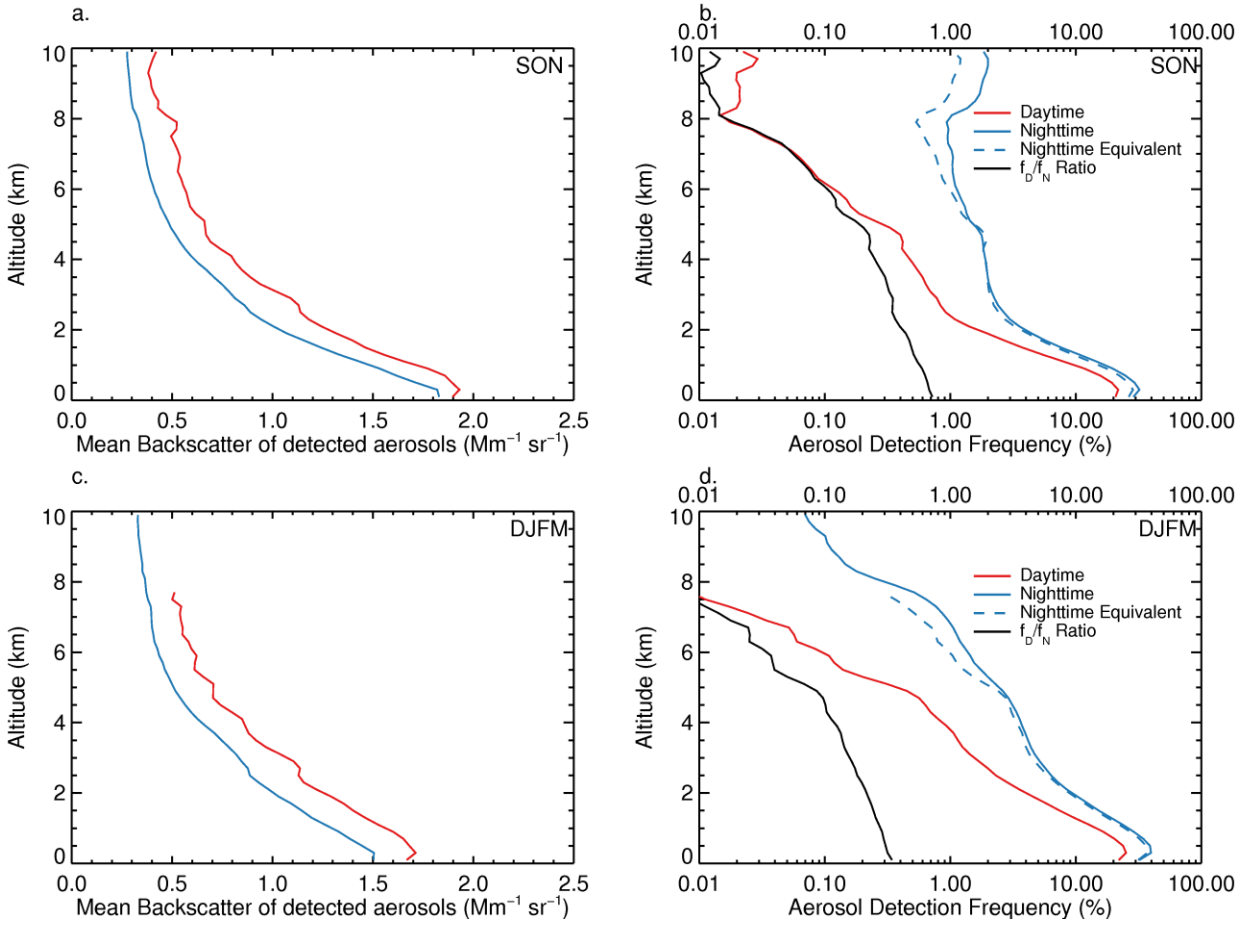

Figure 3.2: Backscatter of detected aerosol layers (a,c) and vertical profiles of aerosol detection frequency (b,d) and for 2006-2012 and latitude interval 61°-71°N. Daytime profiles are shown in red, nighttime profiles in blue. The top panels are for the months of September through November (SON), while the bottom panels are for December through March (DJFM). The black line on panels b, d shows the daytime-to-nighttime detection frequency ratio (f_D/f_N). The dashed blue line shows the nighttime-equivalent detection frequency.

We separate the months of SON and DJFM (Figure 3.2a,c). For both time periods the backscatter of detected aerosols decreases rapidly with increasing altitude, from 1.5-2 Mm^{-1} near

the surface to values <0.5 Mm^{-1} above 6 km altitude. The backscatter of detected layers is similar for daytime and nighttime orbits, with daytime backscatter being 10-15% higher than nighttime. We find much larger differences in the daytime and nighttime aerosol detection frequency (Figure 3.2b,d). For nighttime retrievals, the aerosol detection frequency decreases from 20-30% near the surface to values <1% above 5 km altitude. The daytime detection frequency is always lower and decreases much more rapidly with altitude, reaching values <1% above 2 km altitude. This indicates a much reduced ability of CALIOP to detect aerosols layers over the Arctic during daytime, especially in the free troposphere. We further consider this by examining the ratio between daytime and nighttime detection frequency (shown as a black line in Figure 3.2b, d). This ratio decreases from values of 0.4-0.8 near the surface (meaning that during the day 60-20% fewer aerosol layers are detected than at night) to <0.1-0.3 above 4 km altitude. This behavior is the result of the rapid decrease of the backscatter with altitude: a higher fraction of the faint aerosol layers at higher altitudes fall below CALIOP's daytime backscatter sensitivity threshold.

In order to exclude the possibility that a diurnal cycle in relative humidity (RH) drives the difference in extinction and aerosol detection frequency between daytime and nighttime retrievals, we compare the daily average RH for descending (daytime) and ascending (nighttime) orbits for the same spatial region and temporal period, using the retrievals from the NASA Atmospheric Infrared Sounder (AIRS) on board the A-train AQUA satellite for one year of data (2006-07). The two populations differ in the mean by RH=3% (daytime higher). We find that the random variable representing the standardized difference of the two means falls within one standard deviation from zero, indicating that the two RH populations can be considered statistically indistinguishable.

The differences in detection thresholds during day and night affect our ability to reconstruct the full seasonal cycle of aerosols over the Arctic, especially between late spring and early fall,

when daytime orbits dominate (Figure 3.1). To address this issue, we have developed an empirical method that derives a "nighttime-equivalent" gridded extinction, that is, the extinction that would be retrieved if all retrievals took place under nighttime conditions. We consider the CALIOP dataset (2006-2011) in the latitude range 61-71°N for the September-March period. For each grid-box within the domain, we calculate the ratio between daytime and nighttime detection frequency ($\frac{f_D}{f_N}$) and the mean backscatter of all detected layers (β). Figure 3.3 shows the two-dimensional frequency distribution as a function of β and the $\frac{f_D}{f_N}$ ratio. The smallest ratios occur for optically thin aerosols, consistent with Figure 3.2, whereas for optically thicker aerosols the daytime detection frequency tends to approach the nighttime detection frequency. The mean ratio for each backscatter bin is indicated by black circles in Figure 3.3. Despite considerable scatter in the frequency distribution, the mean ratio falls along a straight line. The linear total least squares fit to the points is $\frac{f_D}{f_N}$ =-0.114+0.522$\cdot\beta$, with β in Mm^{-1} sr^{-1}. We use this empirical relationship to scale the daytime detection frequency as a function of the mean backscatter of the detected layers, by taking the reciprocal of the detection frequency ratio, which we will refer to as our scaling factor, SF:

$$SF = 1/(-0.114 + 0.522 \cdot \beta) \quad \text{(Equation 3. 1)}$$

The nighttime-equivalent gridded extinction, $\overline{b_{ext}}$, is then calculated by combining the nighttime gridded extinction with the scaled daytime gridded extinction:

$$\overline{b_{ext}} = (f_N \cdot b_{ext,N} \cdot N_N + f_D \cdot SF \cdot b_{ext,D} \cdot N_D) \,/\, (N_N + N_D) \quad \text{(Equation 3.2)}$$

where the subscripts N and D indicate nighttime and daytime, b_{ext} is the mean extinction of the detected layers, f is the detection frequency of aerosol layers and N is the number of 5-km orbit segments. The scaling factor is kept in the range 1-50, and the scaled daytime detection frequency $f_D \cdot SF$ is capped at 100%. Mean values for SF range from 1.6-2 at 0-2 km to 5.5-6.2 at 4-6 km.

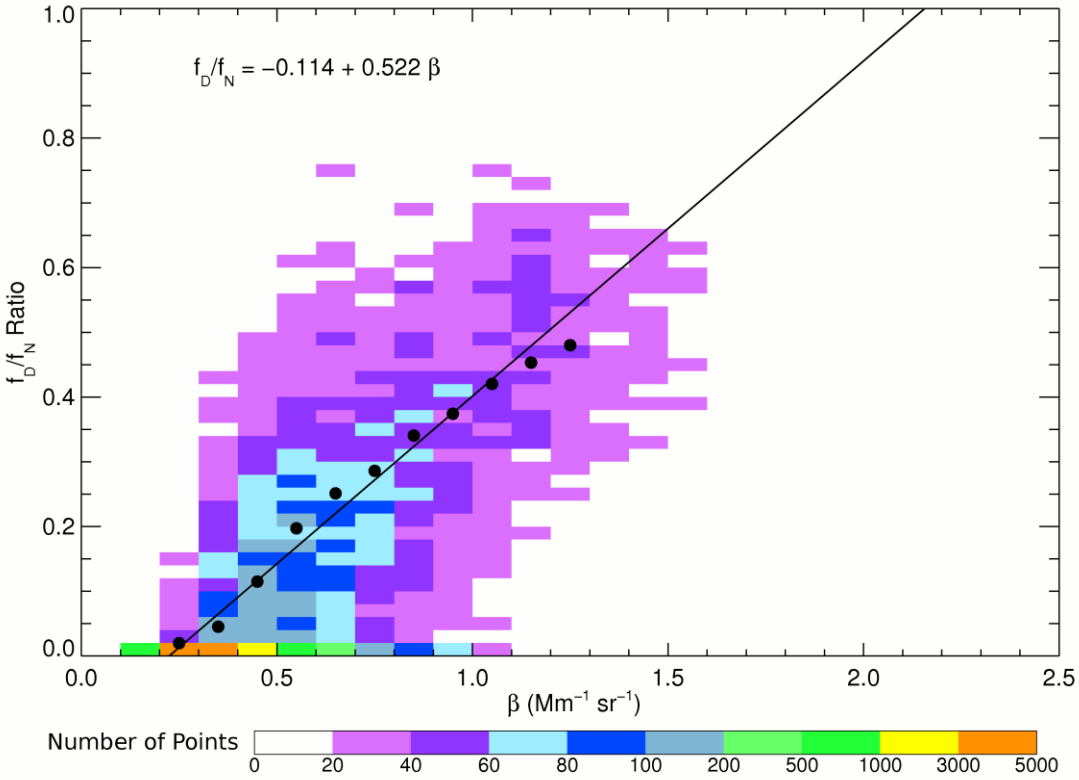

Figure 3.3: Scatterplot of the daytime-to-nighttime aerosol detection frequency ratio (f_D/f_N) as a function of the mean backscatter of the detected aerosols, β, for 61°-71°N latitude from September through March, 2006-2012. Colors represent the number 5-km orbit segments in each 2-D bin. Black circles correspond to the average value of (f_D/f_N) for each value of mean backscatter. The straight line is the weighted reduced major axis linear fit to the black circles.

In obtaining the scaling factor (Equation 3.1), we use the mean backscatter obtained from both daytime and nighttime retrievals on the x-axis of Figure 3.3. As shown in Figure 3.2, the daytime backscatter is 10-15% higher than the values retrieved at nighttime. Using only daytime backscatter in constructing Figure 3.3, leads to a much higher scatter and a less statistically robust relationship. The nighttime-equivalent approach corresponds to assuming that, for daytime retrievals, aerosols layers between the daytime and nighttime detection thresholds have the same extinction as the layers that are detected (Equation 3.2). We recognize that this results in an overestimate of the correction (10-15% during summer and less than 7% for other seasons), however small compared to the large values of the scaling factors (100-300%). The nighttime-equivalent extinction also assumes that aerosols undetected at nighttime have zero backscatter and extinction.

The nighttime-equivalent detection frequency $(f_{\mathrm{N}} \cdot N_N + f_{\mathrm{D}} \cdot SF \cdot N_D)/(N_N + N_D)$ is very close to the nighttime detection frequency (f_{N}) (Figure 3.2b,d), indicating that the linear fit derived in Figure 3.3 is reasonable and produces self-consistent results. In the next section, we compare CALIOP extinction retrievals and our empirical nighttime-equivalent extinctions to ground-based and aircraft observations over the Arctic.

3.3 Comparisons of CALIOP extinction retrievals with independent measurements

3.3.1 Surface in situ measurements

We compare the CALIOP extinctions to nephelometer measurements at Barrow (Alaska, USA) and Alert (Nunavut, Canada) (Table 3.1 and Figure 3.4).

Ambient air is drawn into the nephelometers via a heated inlet, which desiccates the aerosols by decreasing the relative humidity (RH) to values below 30%. The cut-off diameter of the inlet nozzle is 10 μm (Delene and Ogren, 2002; Garrett et al. 2011). The sample volume is then

illuminated with green light (550 nm); the scattering by aerosol particles is integrated over a broad range of angles (7-170°) to yield the scattering coefficient, b_{scat}. The absorption coefficient (b_{abs}) is also measured by a particle soot absorption photometer at both stations. The extinction coefficient is obtained by adding b_{scat} and b_{abs}. When absorption measurements are not available we assume $b_{ext} \cong b_{scat}$. This is a reasonable approximation since b_{abs} is generally less than 5% of b_{scat} for Arctic aerosols (Delene and Ogren, 2002). Whereas for Barrow the data is already daily-averaged, for Alert hourly averages are used, and we require at least 8 measurements per day to calculate the daily mean.

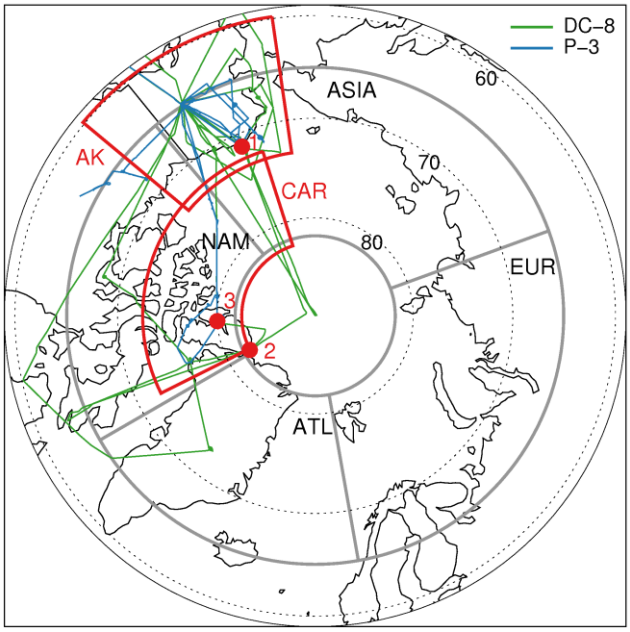

Figure 3.4: Arctic map with the location of observations used in this study. Red circles indicate the ground stations: (1) Barrow, (2) Alert, and (3) Eureka. The ARCTAS DC-8 (green) and P-3 (blue) flight tracks during April 2008 are also shown. The two regions enclosed by red lines are the domains where CALIOP is compared to ARCTAS measurements: Canadian Arctic (CAR) and Alaska (AK). Grey lines define the four Arctic sectors used in this study: European (EUR), Asian (ASIA), North American (NAM) and Atlantic (ATL).

When comparing satellite observations with ground measurements, a common problem is the coincidence in space and time between surface measurements and satellite retrievals. This is particularly exacerbated for CALIOP given its narrow footprint. Anderson et al. (2003) demonstrate that at a distance of 160 km spatial correlation between simultaneous measurements has decreased to a value of 0.8, and beyond this distance the correlation rapidly falls. We thus extract CALIOP extinctions in boxes around Alert and Barrow with mean distances from the stations of 170 km and 200 km, respectively. The box size is a compromise between the need for a statistically sufficient number of CALIOP points and the ability of the station to effectively represent the surrounding region. The box around Alert is smaller in size because more CALIOP overpasses occur in the vicinity of this high latitude station relative to the lower latitude of Barrow. These box sizes are also consistent with the temporal resolution (1 day) and the maximum temporal offset between in situ observation and satellite overpasses (~8 h) assuming a typical horizontal transport velocity of 5 m/s. In order to compare CALIOP and in situ measurements, we require a minimum of ten 5-km CALIOP orbit segments in any given day. We use the CALIOP gridded extinction for the 2 lowermost vertical levels (0-400 m).

For comparison to CALIOP, we adjust the in situ dry aerosol scattering measurements to ambient RH following Gassó et al. (2000):

$$b_{scat,amb} = b_{scat,dry}\left(\frac{100-RH}{100-RH_0}\right)^{-\gamma} \quad \text{(Equation 3.3)}$$

Where RH_0 is the relative humidity of the dry samples (30%) and RH is the ambient relative humidity, which is obtained from AIRS satellite retrievals around the stations. The parameter γ is the hygroscopicity factor and is a function of the aerosol type. Gassó et al. (2000) report average values of 0.23 for dust, 0.57 for polluted marine, and 0.69 for a clean marine aerosol. Since aerosols

at Barrow are a mixture of sea salt and pollution aerosols (Quinn et al., 2002), we choose γ=0.57, corresponding to polluted marine. We use the same γ value at Alert.

Table 3.1: Summary of in situ and CALIOP extinctions at Barrow and Alert.

	Station					
Years Location Height	Barrow 2006-2011 71.3°N; 156.6°W 8 m			Alert 2006-2008 82.5°N; 62.5°W 220 m		
Extinctions	Mean ±1σ (Mm^{-1})	Correlation r	CALIOP Bias[a]	Mean ±1σ (Mm^{-1})	Correlation r	CALIOP Bias[a]
CALIOP Standard[b]	9.9±11	0.69	-14%	4.6±5.3	0.75	+15%
CALIOP N.-Equivalent[b]	11±11	0.68	-2%	5.0±5.2	0.80	+23%
CALIOP Upper Bound[c]	23±8.3	0.65	+49%	19±2.7	0.71	+159%
In situ	16±9.1	--	--	7.3±6.9	--	--
In situ with CALIOP threshold	11±9.6	--	--	4.0±5.5	--	--

In situ extinction observations are scaled to ambient relative humidity. Three gridded CALIOP extinctions are listed: standard (assuming that clear air has an extinction of 0 Mm^{-1}), nighttime-equivalent (taking into account the day/night detection threshold and assuming that clear air has an extinction of 0 Mm^{-1}) and upper bound (assuming that clear air has an extinction equal to the CALIOP detection threshold).

a) The CALIOP bias is based on the annual mean values: 100 × (CALIOP-in situ)/in situ.

b) Correlations and biases are calculated against in situ observations with CALIOP threshold applied.

c) Correlations and biases are calculated against in situ observations without applying CALIOP threshold.

For comparison with CALIOP, we also examine the impact of applying CALIOP's nighttime backscatter sensitivity threshold to the ambient in situ observations, by setting to zero all measurements below the threshold. The extinction threshold is calculated by multiplying the

backscatter threshold by a lidar ratio of 40 sr, which is the mean value of the lidar ratio used by the CALIOP algorithm for both Alert and Barrow. Application of this threshold leads to a 30% decrease in annual-mean observed extinction at Barrow (from 16 to 11 Mm^{-1}) and a 45% decrease at Alert (from 7.3 to 4.0 Mm^{-1}) as shown in Table 3.1.

Figure 3.5 and Table 3.1 compares in situ observations at Barrow (2006-2011) and Alert (2006-2008) to CALIOP nighttime-equivalent extinctions. At Barrow, the annual-mean CALIOP nighttime-equivalent extinction (11±11 Mm^{-1}) is 30% lower than in situ observations (16±9.1 Mm^{-1}). Applying the CALIOP detection threshold to in situ observations (11±9.6 Mm^{-1}) yields much better agreement and reduces the CALIOP bias to -2%. Similar results are found at Alert, where the nighttime-equivalent CALIOP extinction (5.0±5.2 Mm^{-1}) displays a 23% positive bias compared to in situ observations after application of the CALIOP detection threshold (4.0±5.5 Mm^{-1}).

At Barrow, CALIOP captures the seasonal cycle observed by ground-based nephelometer, with a maximum in extinction in December-February and a minimum in May-August (Figure 3.5a and 3.5b). The correlation coefficient between the monthly-mean in situ and CALIOP nighttime-equivalent extinction is r=0.68. Interannual variability is relatively small. Quinn et al. (2002) found that the light extinction seasonal cycle at Barrow is controlled by sea salt in October-January, associated with influx from the Northern Pacific Ocean, and by non-sea-salt sulfate in March-June, caused by the transport of pollution from mid-latitude sources. In the summer, efficient wet scavenging and reduced inflow from mid-latitudes leads to a minimum. At Alert, CALIOP also reproduces the observed seasonal cycle, with an extinction maximum in November-March and a minimum in June-September. In summer, aerosol extinctions decrease to values that are often well below the detection limit of CALIOP.

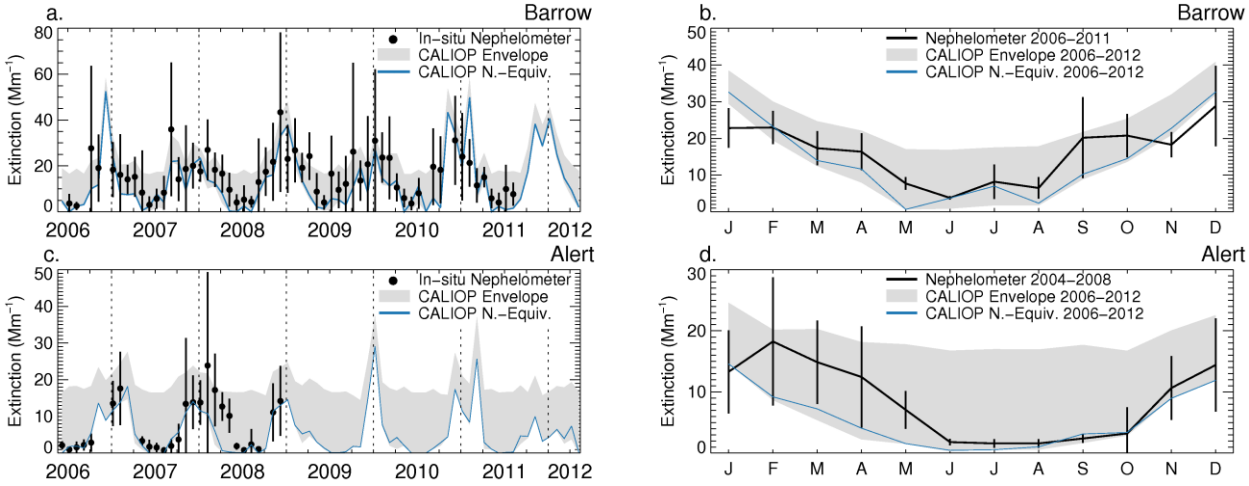

Figure 3.5: Comparison between monthly mean CALIOP 532 nm and in situ 550 nm extinctions at Barrow (top row) and Alert (bottom row). Left panels (a and c): Black full circles indicate the in situ monthly mean extinctions, with vertical bars indicating one standard deviation of the daily observations. The in situ extinctions are scaled to ambient RH. The blue line shows CALIOP nighttime-equivalent mean extinction, with grey shading indicating the envelope of CALIOP retrievals (see text). Right panels (b and d): CALIOP 2006-2012 climatological mean extinction (blue line: nighttime-equivalent; grey shading: CALIOP envelope) are compared to the in situ seasonal mean extinction (black line). For Barrow the in situ climatological mean extinction are for year 2006-2011 but for Alert we use years 2004-2008.

We note that the CALIOP extinctions tend to underestimate in situ observations during spring (March-May) by 37% at Barrow and 63% at Alert (Figure 3.5b and 3.5d). This is unlikely to be related to our assumption of a constant γ=0.57 in the conversion of in situ extinctions to ambient RH. For example, using γ=0.35 during March-May, reflecting less hygroscopic biomass burning aerosols, would only slightly reduce the CALIOP underestimate (Barrow: 28%; Alert: 56%).

We also examine the impact of not taking into account the night/day difference (SF=1) and define the "standard extinction" by setting clear air extinction to 0 Mm^{-1} (see Table 3.1 and Figure 3.5, lower bound of the grey envelope). We find that there is little difference between the CALIOP standard extinctions (Barrow: 9.9±11 Mm^{-1}; Alert: 4.6±5.3 Mm^{-1}) and nighttime-equivalent

extinctions (Barrow: 11±11 Mm^{-1}; Alert: 5.0±5.2 Mm^{-1}) because the annual mean values are dominated by the winter maxima which occur under nighttime conditions. As we will see in sections 3.3.2 and 3.3.3, the difference between the two estimates is more pronounced at higher altitudes where the aerosol layers are less dense.

Our calculated CALIOP nighttime-equivalent extinctions at Barrow and Alert represent a lower bound of the true extinctions, as we assume that when no layer is detected by CALIOP the extinction is 0 Mm^{-1}. We calculate an upper-bound CALIOP extinction at these stations by setting SF=1 and the extinction of clear air to a value equal to the appropriate (day or night) CALIOP detection threshold (see Table 3.1 and Figure 3.5, upper bound of the grey envelope). These upper-bound gridded extinctions overestimate the in situ annual-mean extinction by 50% at Barrow (upper bound: 23 Mm^{-1}; in situ: 16 Mm^{-1}) and 160% at Alert (upper bound: 19 Mm^{-1}; In situ: 7.3 Mm^{-1}). At Alert the seasonal cycle of the upper bound is weaker compared to in situ observations. In situ observations are much closer to the nighttime equivalent in the summer, showing that the true extinction of the undetected layers is much below the sensitivity threshold.

3.3.2 ARCTAS aircraft measurements

During the NASA ARCTAS campaign, nephelometers on-board the DC-8 (Anderson et al., 1998) and P-3 aircraft (Anderson and Ogren, 1998) measured aerosol scattering coefficients at 550 nm. Concurrent measurements of the scattering enhancement factor and ambient RH allow the calculation of the scattering coefficient at ambient RH, as described in Shinozuka et al. (2011). The total extinction at 550 nm is obtained by adding the scattering coefficient at ambient RH to the single particle soot photometer absorption measurements (Clarke et al., 2004).

In analyzing ARCTAS April 2008 measurements we consider two regions: the Canadian Arctic (CAR: 72.5-82.5°N, 62.3-162.3°W) and Alaska (AK: 59.8-73.3°N, 127.9-171.8°W), as

shown in Figure 3.4. Thick aerosol plumes (with CO>200 ppbv or b_{ext}>150 Mm^{-1}) are excluded from the ARCTAS dataset. We calculate the CALIOP mean extinction profiles for these two regions on the days when flights took place (9 DC-8 flights and 7 P-3 flights over AK; 5 DC-8 flights and 2 P-3 flights over CAR). Bian et al. (2013) demonstrated that the ARCTAS measurements along the flight track were representative of regional averages during spring 2008. Figure 3.6 shows the in situ extinction profiles observed during the April 2008 ARCTAS deployment over the AK region. The largest extinctions are observed near the surface (20-30 Mm^{-1}) with a secondary maximum at 3-4 km. Over the CAR region, the surface maximum reaches lower values (Figure 3.7), but the profile also displays a secondary maximum in the mid-troposphere.

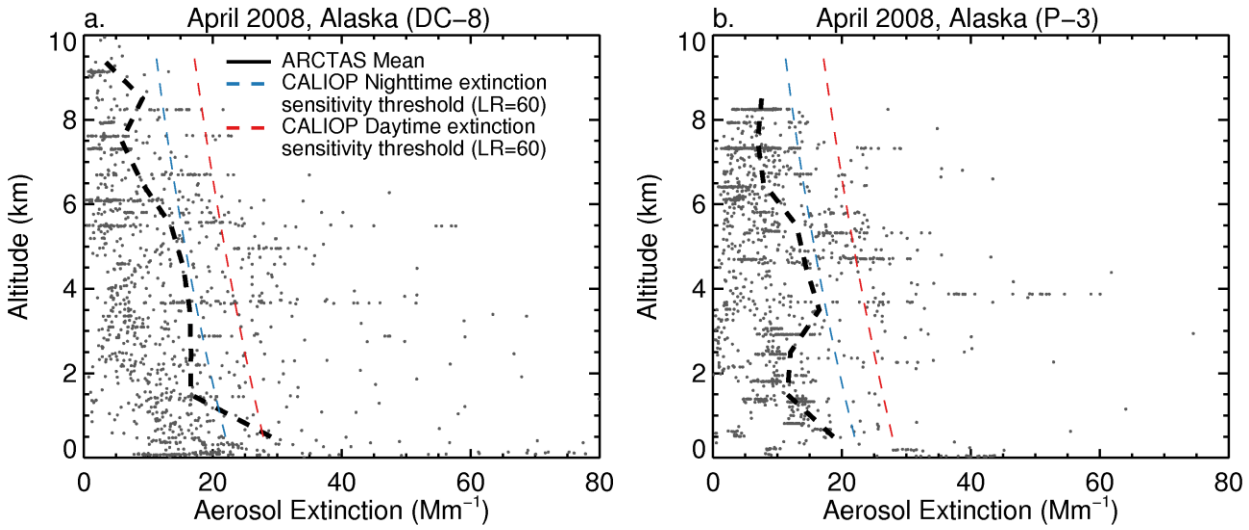

Figure 3.6: ARCTAS mean extinction profiles for April 2008 over the AK domain shown in Figure 3.4 for the DC-8 (a) and P-3 (b) aircraft platforms. The ARCTAS 1-minute average measurements are shown with grey dots, whereas their altitude-binned mean is shown with a dashed black line. All measurements are corrected to ambient RH. The CALIOP daytime and nighttime extinction detection thresholds are also shown with a red and blue dashed line respectively, assuming a Lidar Ratio of 60 sr (see text).

We compare observed in situ extinctions to the CALIOP 80-km sensitivity thresholds (Figure 3.6). In order to convert the CALIOP backscatter threshold to extinction, we use a lidar ratio of 60 sr, which is representative of the smoke aerosols prevalent during ARCTAS (Burton et al., 2012). We find that 83% of the ARCTAS observations in spring are below the CALIOP nighttime sensitivity threshold (AK: 76%; CAR: 96%). CALIOP would thus only be able to detect the strongest haze events. Figure 3.7 displays the in situ mean extinction profiles with the CALIOP 80-km nighttime backscatter sensitivity threshold applied (extinction measurements corresponding to values of backscatter below this threshold are set to zero). The resulting observed extinction profile is significantly reduced, with column integrated AOD decreasing by 45% over Alaska (from 0.12 to 0.065) and by 90% over the Canadian Arctic (from 0.065 to 0.007).

The retrieved daytime CALIOP extinction profiles during ARCTAS (red lines) have very low extinction values, typically below 5 Mm^{-1} over Alaska and below 2 Mm^{-1} over the Canadian Arctic. After we apply our scaling factor (section 3.2.3), the nighttime-equivalent CALIOP profiles (blue lines) exhibit extinction values up to 7-8 Mm^{-1}. Over Alaska, the CALIOP nighttime-equivalent mean extinction profile has a shape that is similar to the in situ observations with threshold applied: high values near the surface and a secondary maximum at 3-6 km (Figure 3.7a, b). The CALIOP nighttime-equivalent is 20% lower than in situ measurements, with a column AOD of 0.05 (in situ observations after threshold: 0.065). Over the Canadian Arctic (Figure 3.7c, d) aircraft observations were much sparser. In addition, the measured extinction was lower than over AK, causing even fewer points to survive the application of CALIOP's threshold. Despite these limitations CALIOP reproduces to some extent the shape of the profiles. We note that for the summer ARCTAS deployment, observed extinctions are so low that they are below CALIOP's threshold all the time, and are thus not shown here.

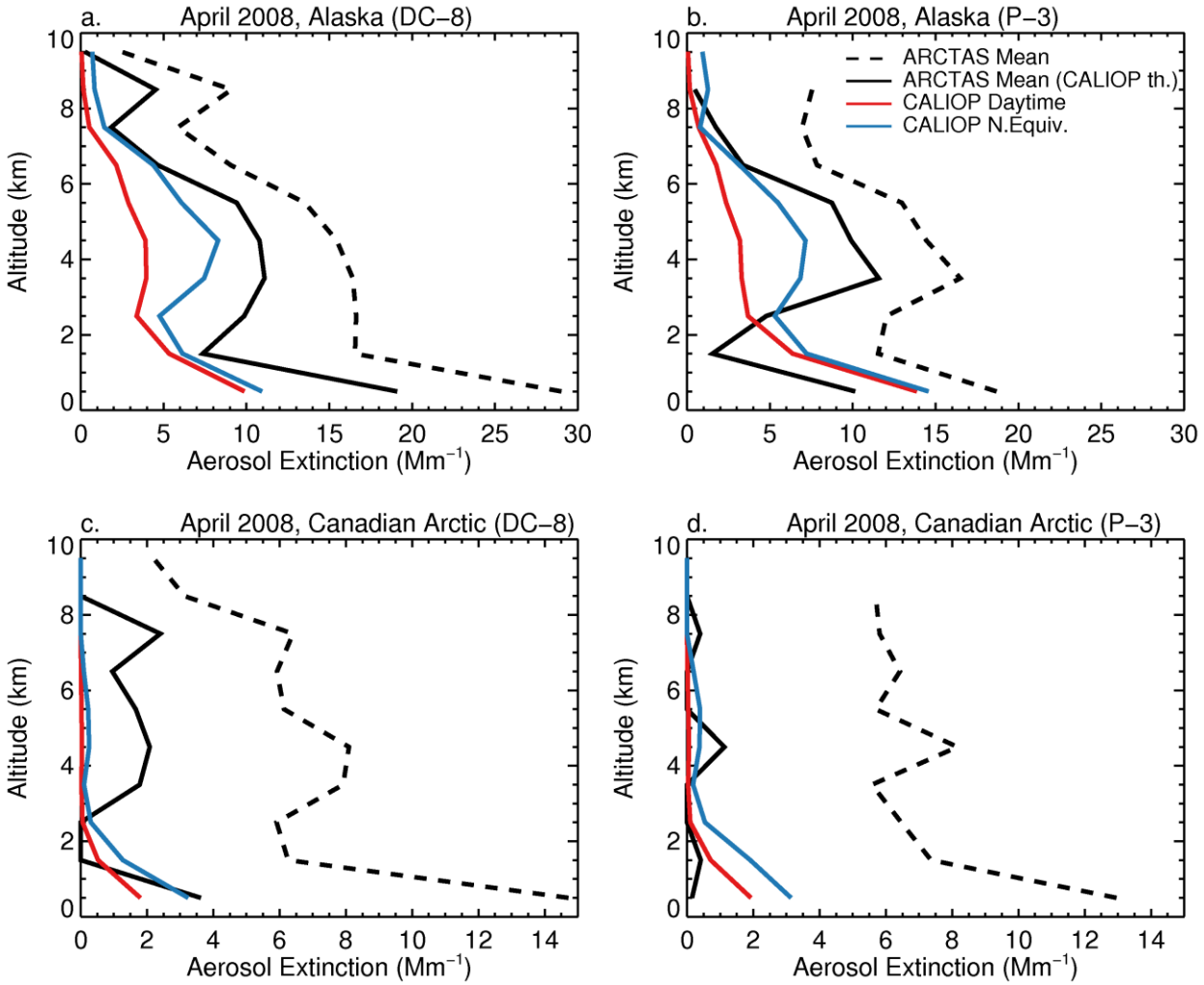

Figure 3.7: Comparison between CALIOP and ARCTAS mean extinction profiles for the DC-8 and P-3 flight days over AK (a,b) and CAR (c,d) in April 2008. In situ aircraft profiles of extinctions are shown with (solid black line) and without (dashed black line) the CALIOP nighttime threshold applied. The red line shows the CALIOP standard (daytime) mean extinction profile, whereas a blue line indicates the nighttime-equivalent mean extinction profile.

3.3.3 High Spectral Resolution Lidar at Eureka, Canada

We compare CALIOP backscatter retrievals with the backscatter measured by the High Spectral Resolution Lidar (HSRL) at Eureka, Nunavut, Canada (80.0ºN, 86.0ºW, 10 m amsl). The University of Wisconsin has operated this lidar since 2006 (Eloranta et al., 2006). A Millimeter Cloud Radar also operates at the site and we use its backscatter return to mask out clouds and precipitation. The lidar is aligned 4˚ off the zenith to avoid reflection from horizontally oriented ice crystals (HOI). In computing the HSRL mean profile we consider only clear-sky profiles for the January to April period of 2007-2009. We exclude the months of April 2007, and January-February 2008 because of data quality issues related to instrumentation failures. To discriminate aerosols from other atmospheric scatterers we apply a linear depolarization threshold of 10%. This value is consistent with previous measurements of aerosol depolarization ratio at Eureka (Ishii et al., 2001). While aerosol extinctions are also retrieved by the Eureka HSRL, the values are very noisy because of the very small field-of-view of the receiver. We thus choose to compare the HSRL backscatter to the CALIOP backscatter, averaged within ±1° latitude and ±5° longitude centered at Eureka, resulting in an average distance with the satellite footprint of less than 110 km.

Figure 3.8 shows CALIOP and HSRL vertical profiles of aerosol 180° backscatter for January-February (JF) and March-April (MA). In JF, HSRL measurements show a maximum of 0.8 Mm^{-1} sr^{-1} below 1 km, where 40% of the column-integrated backscatter resides (dashed black line, left panel). In MA the column-integrated backscatter is 40% higher than in JF. The bulk of this enhancement in backscatter (>85%) occurs above 1 km. This seasonal change in the aerosol vertical distribution is indicative of enhanced aerosol influx in the free troposphere.

Applying CALIOP's nighttime sensitivity threshold to the HSRL measurements leads to a mean 10-15% decrease in backscatter below 1 km and a larger (50-75%) decrease above 1 km

(black solid line). The nighttime-equivalent CALIOP backscatter reproduces the shape of the profiles but is systematically too low by a factor of 2-8 below 5 km. We find that the nighttime-equivalent backscatter qualitatively reproduces the MA mid-tropospheric backscatter enhancement (blue line, right panel) whereas the standard backscatter shows values similar to those observed in JF (red line, right panel). The vertical partitioning of aerosol backscatter is consistent between the two sensors: CALIOP observes 73% of the vertically integrated backscatter below 1 km in winter (HSRL with sensitivity threshold: 70%), whereas this fraction decreases to 35% in spring (HSRL with sensitivity threshold: 46%).

The CALIOP systematic underestimate could be due to the fact that too many aerosol layers above Eureka have extinctions below the CALIOP detection threshold, as was found in our ARCTAS comparison over the Canadian Arctic (Figure 3.7c,d). There could also be potential issues with our retrieval of aerosol backscatter from the HSRL measurements. When we compare the HSRL backscatter to ARCTAS observations in April 2008 above Eureka by assuming a lidar ratio of 60 sr for the in situ measurements, we find that HSRL measurements are a factor of 2 higher than in situ measurements, at all altitudes (not shown). Furthermore, the HSRL backscatter values at the surface are a factor of two higher than the ambient backscatter measured at the nearby station of Alert for 2007-2008 (Figure 3.8). Though the reason of this overestimate is not clear, we hypothesize that the presence of ice crystals mixed with aerosols might artificially elevate the backscatter retrieved by HSRL.

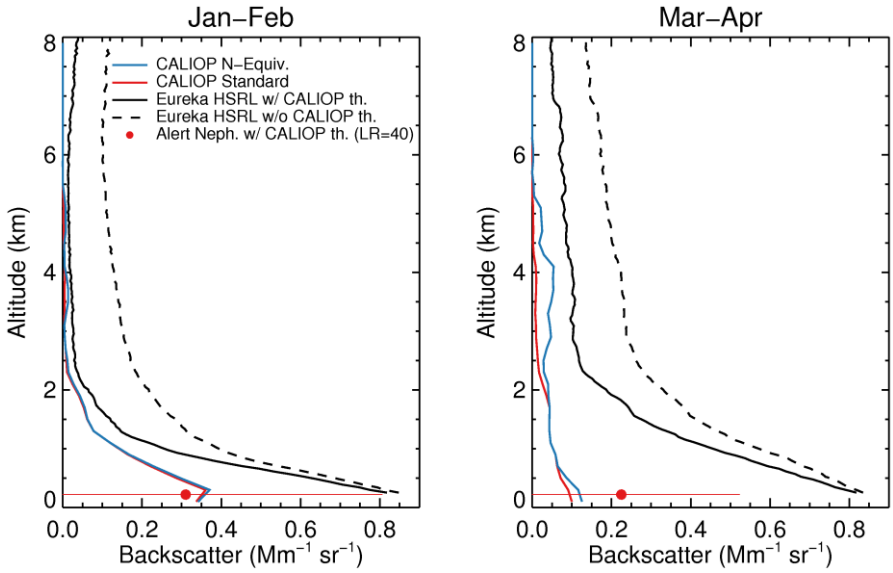

Figure 3.8: Vertical profiles of 180° backscatter observed by the ground-based HSRL lidar at Eureka, Nunavut, Canada (80.0°N, 86.0°W) for January-February (left panel) and March-April (right panel) 2007-2009. The HSRL backscatter profiles with (solid black line) and without (dashed black line) the CALIOP nighttime threshold applied are compared to the CALIOP nighttime-equivalent backscatter (blue line) and standard backscatter (red line). The median aerosol backscatter measured at the nearby station of Alert is obtained by dividing the measured extinction by a lidar ratio of 40 sr, and is shown with and without the CALIOP threshold.

In summary, our comparison of CALIOP retrievals with independent measurements of aerosol extinction demonstrates that when we take into account the CALIOP sensitivity threshold, the retrieved nighttime-equivalent extinction captures in situ observations to within 25% in most cases. At the surface, CALIOP reproduces the seasonality of Arctic aerosols as observed at Barrow and Alert. In the free troposphere, CALIOP reproduces the vertical distribution of aerosol layers and their seasonal variations as illustrated by our comparisons to ARCTAS aircraft profiles and HSRL profiles above Eureka. As a result of this sensitivity threshold and the low extinctions of aerosols over the Arctic, only a fraction of the column AOD can be retrieved by CALIOP over the Arctic (e.g. ~30% for AK and ~15% for CAR in spring, see section 3.3.2). Exactly how much depends on the column aerosol loading and the vertical distribution of extinction.

3.4 Results

3.4.1 Pan-Arctic surface extinction maximum in winter

Figure 3.9 shows the mean seasonal cycle of CALIOP nighttime-equivalent extinction in the lower (0-2 km), middle (2-5 km) and upper troposphere (5-8 km) over the Arctic for 2006-2012. The Arctic is divided into Low Arctic (59°-69°N) and High Arctic (69°-82°N). We consider four sectors: European (EUR, 10-110°E), Asian (ASIA, 110°E-140°W), North American (NAM, 140-60°W) and Atlantic (ATL, 60°W-10°E) (see Figure 4). These sectors are intended to capture the typical transport pathways for short-lived pollutants (5-8 days) following the Lagrangian trajectory studies of Eckhart et al. (2003) and Stohl et al. (2002).

In the High Arctic at 0-2 km (Figure 3.9a), CALIOP extinctions vary from a minimum of 2 Mm^{-1} to a maximum of 16 Mm^{-1} with an annual mean of 9 Mm^{-1}. The seasonal cycle is the same as at Barrow and Alert with a December-March maximum, followed by a sharp decline and a summer minimum, in agreement with the well-known seasonality of Arctic Haze. All four sectors display the same seasonal cycle. The largest extinctions are observed in the European sector during winter-spring, consistent with early studies identifying the European/Russian Arctic as the most polluted Arctic sector, because of its proximity to western Eurasian sources (Rahn and Lowenthall, 1984; Raatz and Shaw, 1984; Barrie et al., 1989). This finding is also consistent with the recent modelling intercomparison study of Shindell et al. (2008), who found that all atmospheric chemical transport models point to western Eurasia as the largest source region of aerosols and SO_2 at low altitude. CALIOP observations show that the Asian sector displays slightly lower values relative to the European sector, followed by the N. American sector. The Atlantic sector is the cleanest, with wintertime extinction values nearly a factor of 2 lower than over the European sector.

The Low Arctic at 0-2 km (Figure 3.9b) displays higher CALIOP extinctions (annual mean: 14±3 Mm^{-1}) than the High Arctic. When extinctions are averaged over the entire low Arctic, there is no clear seasonal cycle. This lack of seasonality comes from the out-of-phase seasonal cycle in the Atlantic sector compared to the other sectors. In the European, Asian, and N. American sectors there are two maxima: one in December-January and another in July. The summer peak is consistent with measurements of particle number and volume concentration in the planetary boundary layer at the Zotino Tall Tower Facility (ZOTTO) in the Siberian Low Arctic (60.8°N, 89.35°E), which show a June-July maximum in median particle number concentration (June-July: 900 cm^{-3}; November-February: 520 cm^{-3}) and comparable volume concentrations between summer and winter (Heintzenberg et al., 2011). In the Atlantic sector, the seasonality is reversed with a summer minimum and a December-March maximum, corresponding to elevated sea salt aerosol concentrations generated by high winds during winter (see section 3.4.2).

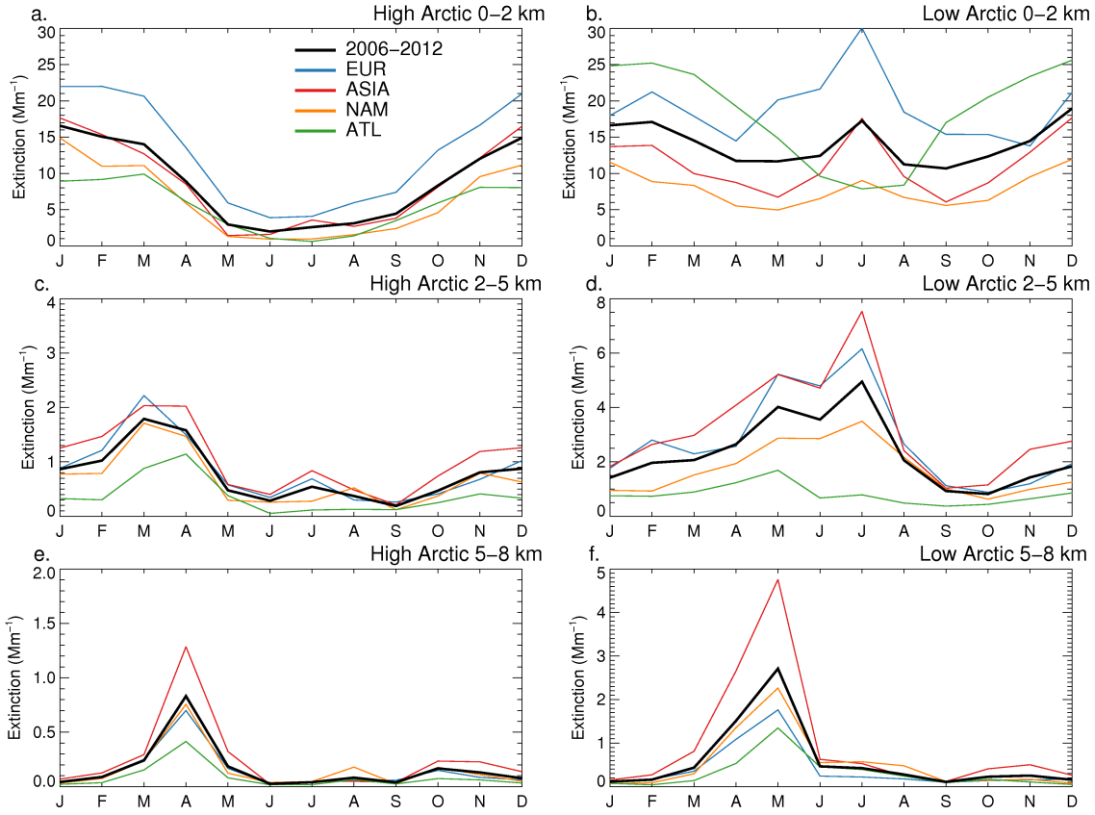

Figure 3.9: Seasonal cycle of monthly CALIOP aerosol nighttime-equivalent extinction at 0-2 km (top panels), 2-5 km (middle panels) and 5-8 km (bottom panels) averaged over 2006-2012. Left panels (a,c,e) are for the High Arctic (59°-69°N); panels on the right (b,d,f) are for the Low Arctic (69°-82°N). The black line corresponds to the mean extinction for the entire High and Low Arctic regions, while colored lines are for the individual Arctic sectors defined in Figure 3.4.

Figure 3.10 shows the seasonal mean (2006-2012) horizontal distribution of CALIOP extinction for different altitude ranges. The main feature in the lower troposphere is the large-scale winter (DJF) maximum in extinction (25-40 Mm^{-1}) extending throughout northern Russia. This enhancement is associated with low-level transport of pollution aerosols induced by the meridional circulation along the Siberian anticyclone (Barrie, 1986). An enhancement in extinction is also seen over the central-Russian Arctic (5-7 Mm^{-1}) at 2-5 km, which could indicate that a fraction of Eurasian pollution is lifted into the free troposphere by cyclones moving along the western

periphery of the Siberian anticyclone (Raatz and Shaw, 1994). Another winter surface maximum is located over the Norwegian Sea and is due to sea salt aerosols produced by the strong wind speeds (Figure 3.10). During spring at 0-2 km, extinction values decrease across the entire Arctic, reaching 5-15 Mm^{-1} in the High Arctic.

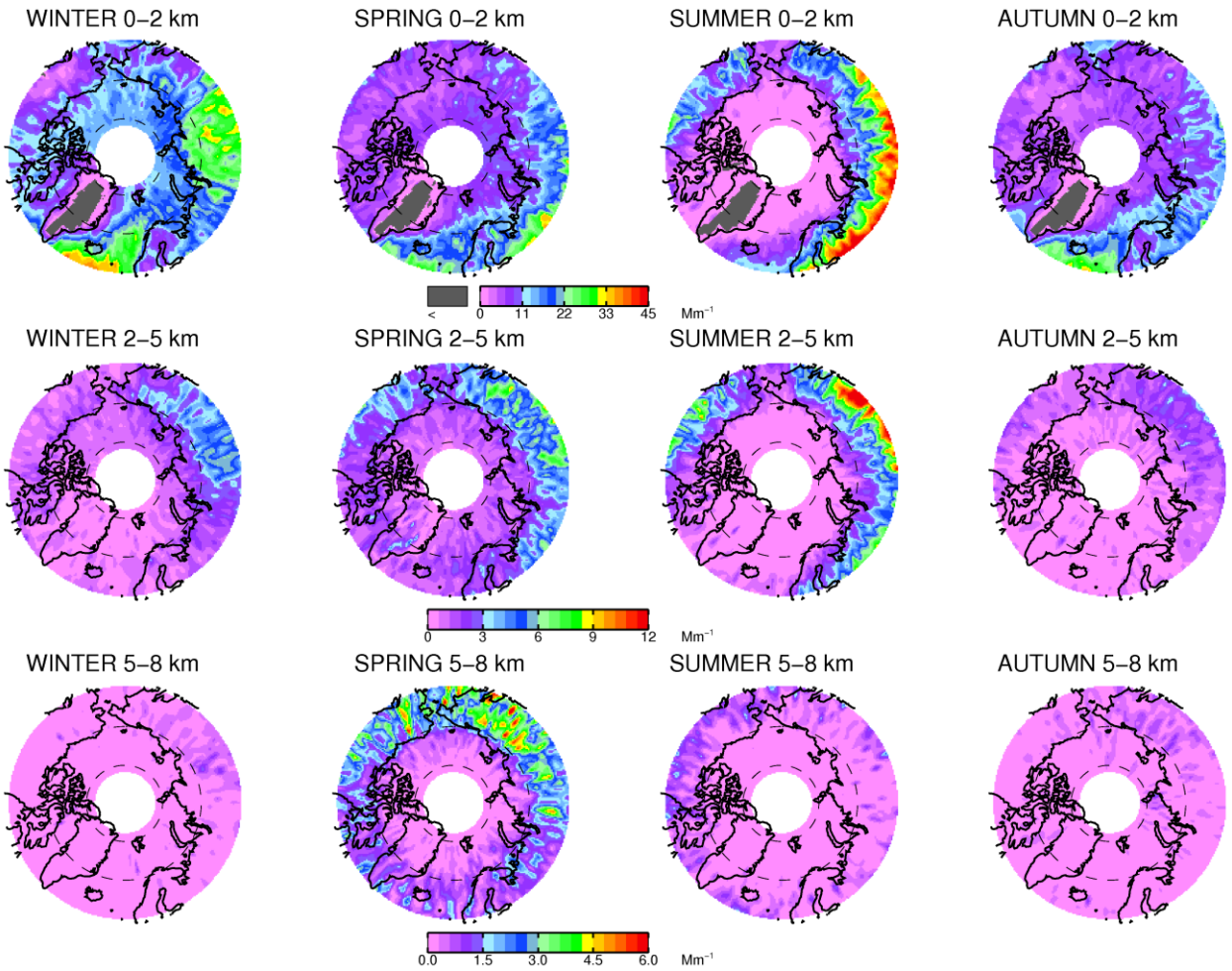

Figure 3.10: Spatial distribution of the 2006-2012 seasonal mean CALIOP nighttime-equivalent extinction. Maps are shown at 0-2 km (top panels), 2-5 km (middle panels) and 5-8 km (bottom panels) for winter (DJF), spring (MAM), summer (JJA) and autumn (SON). Note that the color scale saturation values are lowered at higher altitudes. Dashed lines mark the 70˚N and 80˚N latitude circles.

Figure 3.11 shows the mean nighttime-equivalent extinction vertical profiles by sector and season for the Arctic poleward of 65°N. Extinction peaks in the lowest 0.5 km in all sectors and seasons but is highest in winter, with mean values of 40 Mm^{-1} for the European sector, and 30 Mm^{-1} for the Asian and North American sectors. Because of the strong stratification of the lower atmosphere in winter and late autumn, extinction drops rapidly with altitude in these seasons. In both winter and autumn, two thirds of the column AOD is found below 1 km.

3.4.2 Summertime extinction maximum in the Low Arctic due to biomass burning

As noted in Section 3.4.1, CALIOP observes high aerosol extinctions in July in the lower troposphere over the Low Arctic. This July peak is associated with the summertime maximum in forest fires emissions in the boreal regions of Asia and North America (van der Werf et al., 2006) as well as with a maximum in fire intensity (Giglio et al., 2006; Ichoku et al., 2008). Indeed, we find that the CALIOP classification algorithm identifies most of these aerosols layers as ”smoke” (not shown).

The summer surface peak in the Low Arctic appears to extend to the middle troposphere (Figure 3.9d and Figure 3.10), indicating efficient vertical mixing of boreal forest fire emissions, and a variety of smoke injection heights. This is also reflected by the shape of extinction profiles in summer, which display a convex shape in all land sectors (Figure 3.11). At 0-2 km in July, CALIOP extinctions over the European sector exceed the extinctions in the Asian sector (Figure 3.9b). This is reversed at 2-5 km altitude, where we find larger extinction enhancements in the Asian sector compared to the European sector (Figure 3.9d, and Figure 3.10). Retrievals of smoke plume height from space by the Multi-angle Imaging SpectroRadiometer (MISR) over North America show that plumes originating from burning of boreal forests and shrubland are generally thicker, longer and more elevated than those found over regions characterized by temperate forests

(Val Martin et al., 2010). In the Asian and North American sectors, significant burning takes place within the Arctic, and involves the burning of boreal forests. In the European sector on the other hand, emissions maximize at lower latitudes (45-60°N) and altitudes, where the dominant biome consists of temperate forests and grassland, and is characterized by fuel loads that are a factor 10-20 lower than those found in the boreal regions (Van der Werf et al., 2006). This contrast in vegetation burned and burning heights could thus explain the different vertical distribution of aerosols in the Low Arctic for different sectors.

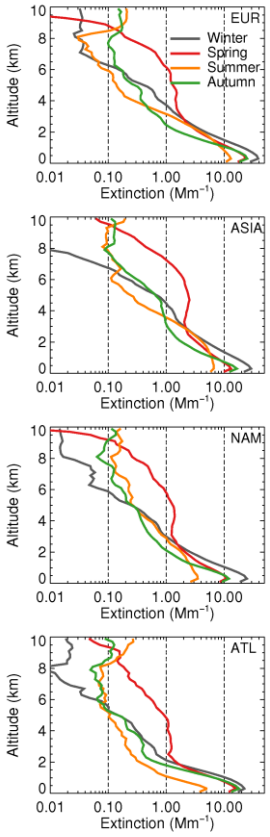

Figure 3.11: Mean seasonal vertical profiles of CALIOP nighttime-equivalent extinction for the four Arctic sectors poleward of 65°N (from top to bottom): European, Asian, N. American, Atlantic.

3.4.3 Summertime extinction minimum over the High Arctic: efficient scavenging and slow transport

During summer over the High Arctic, CALIOP extinctions display the lowest aerosol loading (Figure 3.9a, c, e). This occurs at all altitudes and for all sectors, as also illustrated in Figure 3.11. However, in the Low Arctic extinction reaches an annual maximum during the summer (Section 3.4.2; Figure 3.9b, d). This leads to a strong meridional gradient in aerosol extinction between 60°N and 70°N (Figure 3.10).

These very low summertime extinctions over the High Arctic could be associated with efficient wet scavenging that takes place during transport from lower to higher Arctic latitudes. Indeed, the modelling study of Browse et al. (2012) found that summertime stratocumulus drizzle causes a factor 10 decrease in sulphate concentrations at the surface between 60°N and 70°N. Matsui et al. (2012) examined the transport efficiency to the Arctic of BC relative to CO, contrasting spring and summer. They found a factor of 17-20 decrease in the BC transport efficiency between spring and summer, which was due to higher precipitation over the latitudes 45-70°N during summer. In addition to efficient wet removal, the poleward withdrawal of the Polar Front is also likely to play a role in preventing transport to the High Arctic in summer, since the Arctic landmasses constitute a heat source rather than a heat sink (Stohl, 2006). Furthermore, the combination of low aerosol burden and CALIOP's high daytime detection threshold leads to very few aerosol layers being detected in the summer, and might thus further exacerbate the CALIOP aerosol extinction gradient between Low and High Arctic.

3.4.4 Springtime aerosol extinction maximum in the middle and upper troposphere

In the High Arctic middle troposphere (2-5 km), the CALIOP extinction maximum occurs in March (0.9-2.3 Mm^{-1}), with values a factor 2-3 higher than the annual average (Figure 3.9c). At

higher altitudes (5-8 km), the peak occurs in April, reaching values of 0.4-1.3 Mm^{-1} (Figure 3.9e). We thus see a progressive shift of the extinction maximum with altitude, from January at 0-2 km, to March at 2-5 km, to April at 5-8 km. The springtime middle and upper tropospheric enhancement is apparent in the extinction profiles as well (Figure 3.11).

This Arctic spring maximum in the middle and upper troposphere is consistent with meridional transport of pollution from mid-latitudes along stable isentropes (Stohl, 2006; Klonecki et al., 2003). Late winter to early spring marks a maximum in cyclonic activity (Klein, 1958; Chen et al., 1991). Cyclones ventilate the planetary boundary layer and inject pollutants into the free troposphere, where they can be rapidly transported over large distances. Once in the free troposphere, a blocking pattern represents a favorable configuration for rapid isentropic poleward transport (Iversen and Joranger, 1985; Di Pierro et al., 2011). The January to March period exhibits the highest frequency of blocking patterns in the northern hemisphere (Lejenas and Okland, 1983).

We find high springtime extinctions over most of the Russian and Alaskan Arctic at 2-5 km (Figure 3.10). This is consistent with outflow from East Asia. In a previous study using CALIOP observations and a chemical transport model, we examined several Asian long-range transport events reaching the Arctic 3-4 days after export from the boundary layer (Di Pierro et al., 2011). Transport occurred at 3-6 km following a strongly southerly pathway over Eastern Siberia and Alaska. Spring is also the season when the occurrence frequency of dust storms is maximum in East Asia (Shao and Dong, 2006). In particular, dust lifted from the Taklimakan desert follows a north-westward route and is injected at altitudes above 5 km (Sun et al., 2001; Yumimoto et al., 2009). Asian dust could thus potentially reach the Arctic upper troposphere during spring. Indeed, we find that the upper tropospheric April-May CALIOP extinction maximum is particularly strong in the Asian sector (Figures 3.9 and 3.10).

Our results are consistent with observations obtained during the TOPSE aircraft campaign, showing increasing fine particle sulphate mixing ratios with altitude as the season progressed from February to May over the American sector (50°N-86°N) (Scheuer et al., 2003). Similarly, Browell et al. (2003) found a 5-fold increase in aerosol number concentration at 4-6 km between February and May during TOPSE. The late spring maximum was also reported by Treffeisen et al. (2006) based on the SAGE satellite retrievals. They attributed it to increased transport from the mid-latitudes at this time of year.

3.4.5 Interannual variability

Among the factors that affect aerosol mass concentration variability on interannual timescales, transport and emissions have been found to play the greatest role and account for 75% of the observed variability at the surface in the High Canadian Arctic (Gong et al., 2010). Biomass burning emissions display a strong interannual variability, especially in boreal environments (van der Werf et al., 2006). Episodic volcanic eruptions at high latitudes can also contribute to the variability in aerosol loading. Changes in meteorology can affect the efficiency of transport to the Arctic from mid-latitudes, but also the scavenging efficiency en route.

Figure 3.12 shows a timeseries (5-day mean) of CALIOP extinction as a function of altitude for the four Arctic sectors poleward of 65°N, while Figure 3.13 shows the monthly variation in CALIOP extinctions over the High and Low Arctic for the six individual years in our record. There appears to be relatively little interannual variability near the surface, with higher variability in the middle and upper troposphere.

In the middle and upper troposphere, spring of 2008 stands out with much larger CALIOP extinctions relative to the multi-year mean. These anomalously high aerosol extinctions were caused by smoke produced during wild and agricultural fires in Russia and Kazakhstan (e.g.,

Warneke et al., 2009; Fuelberg et al., 2010). July 2010 displays some of the largest summertime extinctions observed by CALIOP (Figure 3.13). The enhancements took place over the European and Asian Arctic (Figure 3.12), and are consistent with the wildfires that occurred throughout western Russia during the 2010 heat wave. Witte et al. (2011) reported that Moderate Resolution Imaging Spectroradiometer (MODIS) AOD and fire counts over that region during July and August 2010 were a factor of ~7-8 larger with respect to their 2002-2009 average.

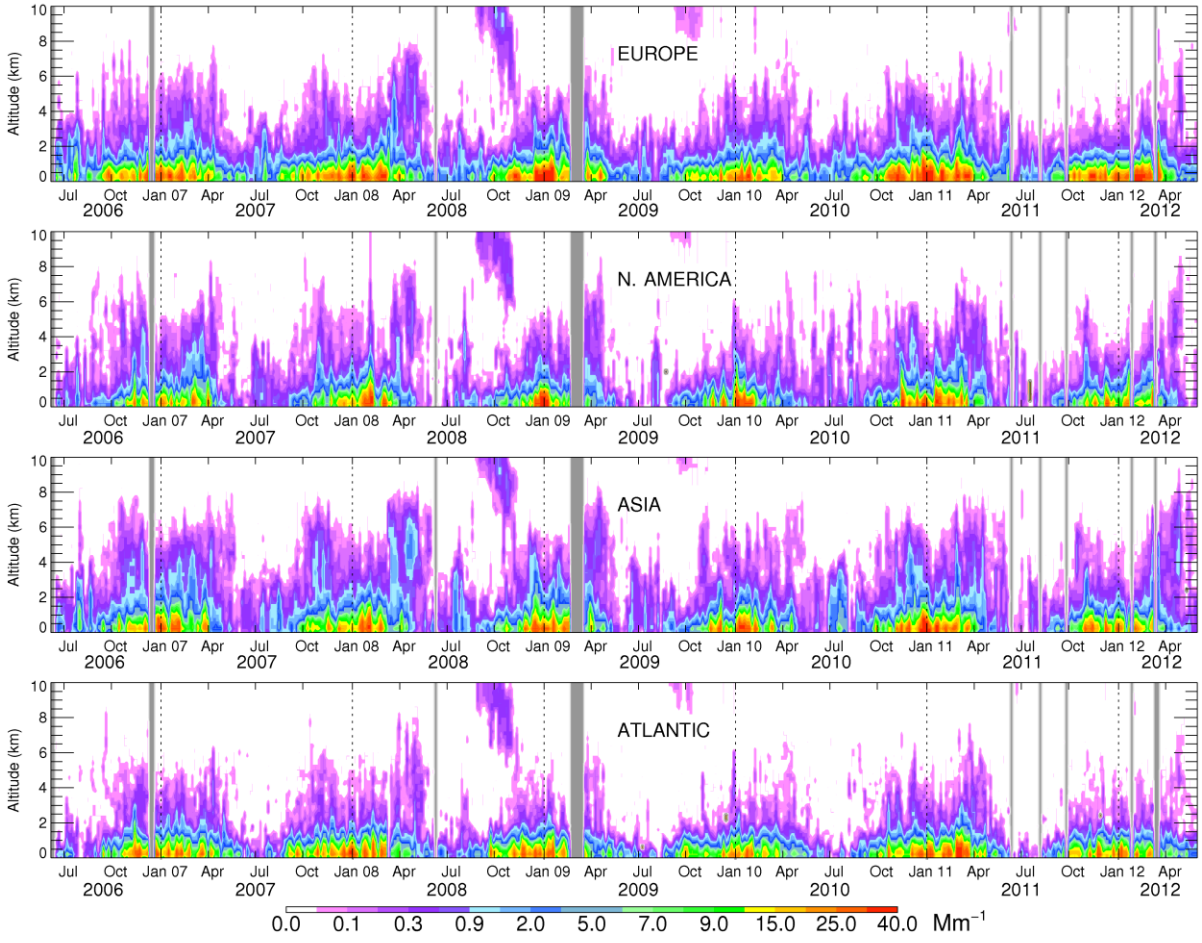

Figure 3.12: Timeseries of 5-day mean nighttime-equivalent CALIOP extinction as a function of altitude for the four Arctic sectors poleward of 65°N. Grey vertical bars indicate CALIOP data gaps.

Figure 3.12 and 3.13b illustrate the influence of the August 2008 Kasatochi volcanic eruption in the central Aleutian Islands, Alaska. The plume of the Kasatochi eruption reached the lower stratosphere, with smaller plumes reaching up to 18-20 km (Martinsson et al., 2009), followed by mixing subsidence. As can be clearly seen in Figure 3.12, the Kasatochi sulfate aerosol plume appears in the Arctic lower stratosphere/upper troposphere in August 2008 and then slowly descends down to 6-7 km altitude, with an extinction maximum occurring at 5-8 km in the High Arctic in October 2008 (Figure 3.13e). Figure 3.12 also exhibits a small aerosol extinction enhancement in September-October 2009 at 8-10 km, which we link to subsidence from the lower stratosphere following the June 2009 Sarychev volcano eruption in the Kuril Islands, Russia (Kravitz et al., 2010).

Particularly low extinctions are observed by CALIOP in November 2009-May 2010 in the High Arctic throughout the troposphere (Figure 3.13, left column). This was followed by a period with higher extinctions in November 2010-May 2011. Variations in atmospheric circulation seem to have controlled these changes. During the first period, the Arctic Oscillation (AO) and the North Atlantic Oscillation (NAO) reached an unusually strong minimum in the winter of 2009-10 (Cohen et al., 2010; Seager et al., 2010). Both indices describe a redistribution of atmospheric mass between the Arctic and the sub-tropics, with the positive phases of AO/NAO associated with lower than usual sea level pressure over the Arctic and higher sea level pressure over the North Atlantic. These very strong negative values were maintained for most of 2010 and then starting in late 2010 both indices increased, reaching positive phases of AO and NAO in spring 2011 (http://www.cpc.ncep.noaa.gov/). The changes in these indices track changes in CALIOP extinctions, with reduced transport with low aerosol extinctions during negative phases of the NAO/AO and enhanced transport with high aerosol extinctions during positive phases of the

NAO/AO. This is consistent with the findings of Eckhart et al. (2003) and Duncan and Bey (2004) who showed that positive phases of the North Atlantic Oscillation (NAO) and Arctic Oscillation (AO) promote enhanced pollution transport to the Arctic from Europe and North America particularly in winter and spring.

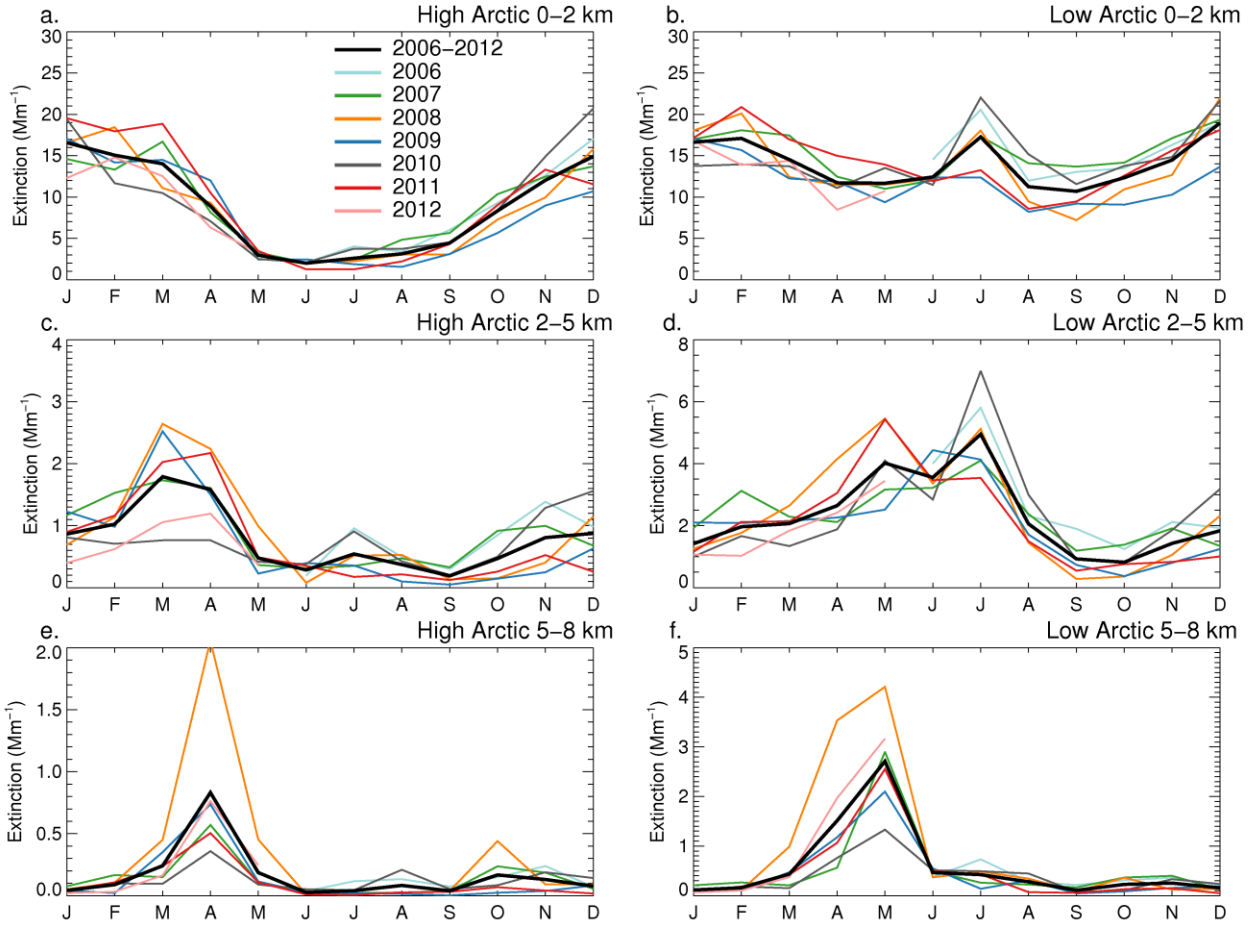

Figure 3.13: Same as Figure 3.9, but colored lines are for CALIOP nighttime-equivalent extinction for individual years between 2006-2012. The black lines correspond to the 6-year average (2006-2012) seasonal cycle of extinction.

3.5 Conclusions

We present a 6-year altitude-resolved distribution of aerosol extinction over the Arctic, retrieved from the CALIOP lidar on board the CALIPSO satellite between June 2006 and May 2012. As the lower CALIOP detection sensitivity during daytime significantly impacts the retrieval of optically thin Arctic aerosol layers, we developed an empirical methodology to take into account this sensitivity, allowing us to reconstruct the full seasonal cycle of Arctic aerosols through the definition of a nighttime-equivalent extinction.

We compared the CALIOP nighttime-equivalent extinction to in situ measurements of aerosol extinction at Barrow (Alaska) and Alert (Canada). CALIOP was able to reproduce the observed magnitude of the extinction to within 25% and captured the seasonal variation at both sites. The nighttime-equivalent extinction was also compared to extinction profiles measured during the NASA ARCTAS aircraft campaign in April 2008. Roughly 80% of the measurements fell below CALIOP sensitivity threshold, more so in the Canadian High Arctic (96%) than over Alaska (76%). When the CALIOP sensitivity threshold was applied to in situ measurements, the observed column AOD was reduced by 50% and we found that CALIOP nighttime-equivalent extinction reproduced the altitude of the observed extinction maxima while capturing 80% of the column AOD.

Additionally, we used the HSRL lidar at Eureka (80°N, 86°W) to validate the seasonal evolution of aerosol 180° backscatter profiles observed by CALIOP during 2007-2009. Although a quantitative comparison is inconclusive as the HSRL backscatter appears to be biased high by a factor of two compared to in situ observations collected in April 2008 during the ARCTAS campaign over the High Canadian Arctic, it is nonetheless able to successfully reproduce the shape of the backscatter vertical profiles measured during the campaign. In relative terms, CALIOP and

HSRL agree as to the fraction of column-integrated backscatter found near the surface (0-1 km) in winter (70-73%) and in the free troposphere (1-8 km) in spring (35-46%).

The 6-year CALIOP extinction observations enabled us to map the spatial distribution of the pan-Arctic surface aerosol maximum during winter. At high Arctic latitudes (>69°N) near the surface, CALIOP extinctions exhibit a strong peak in December-March and a summer minimum in all Arctic sectors. The largest values in winter extinction maximum are centered over the central Russian Arctic. This is consistent with enhanced low-level transport of Eurasian pollution to the Arctic induced by meridional transport along the Siberian Anticyclone. In the Low Arctic near the surface, extinctions over the Asian, European and N. American sectors exhibit a summer maximum in addition to the winter maximum. The summer enhancements are due to transport of biomass burning aerosols from boreal forest fires. During summer, CALIOP extinctions display a sharp drop between 60°N to 70°N. This gradient is likely the result of enhanced wet deposition combined with reduced transport from mid-latitudes as the polar front retreats poleward.

There is a progressive shift of the CALIOP extinction maximum with altitude, from January at 0-2 km, to March at 2-5 km, to April at 5-8 km. The springtime peak extinction in the middle and upper troposphere is consistent with increased insentropic transport of pollution exported from the boundary layer by mid-latitude cyclones. Meridional transport is favored by blocking patterns, which maximize in January-March. The Asian sector shows the highest extinctions in the middle and upper troposphere, as cyclones and blocking patterns become more frequent in spring favoring the uplift and northward transport of pollution from East Asia. Enhanced mineral dust transport from the deserts of northern China and Mongolia could also be contributing.

Widespread agricultural fires in Russia and Kazakhstan took place during spring 2008, when CALIOP extinctions displayed anomalously high extinctions in the mid-troposphere compared to the 2006-2012 seasonal mean. The highest extinction anomaly in the summer record is linked to the intense wildfires that broke out in western Russia in July 2010. A protracted period of below-average extinctions was observed from August 2009 through May 2010 in the low and middle troposphere, which we link to a persistent and strong negative Arctic Oscillation event.

Our understanding of the processes controlling the emissions, transport and deposition of aerosols over the Arctic remain highly uncertain. Indeed, several recent studies have highlighted very large differences among chemical transport models over the Arctic (Textor et al., 2006, 2007; Shindell et al., 2008). Removal processes (wet and dry deposition) are particularly poorly constrained over the Arctic, which results in the inability of models to reproduce the observed seasonality of aerosol concentrations and their individual components (Liu et al., 2011; Bourgeois and Bey, 2011). Our multi-year spatial and temporal distribution of CALIOP extinctions over the Arctic will provide a new tool to validate these processes in global models.

Chapter 4

MODELING OF THE SPATIAL AND VERTICAL DISTRIBUTION OF ARCTIC AEROSOLS

4.1 Introduction

The Arctic is a receptor region for aerosol and gaseous pollution because local anthropogenic sources are relatively small (Shaw, 1995; Law and Stohl, 2007). The processes controlling the transport, emissions, chemical transformations and removal of Arctic aerosols are highly uncertain and poorly constrained by observations. Textor et al. (2007) investigated the source of model differences and compared global aerosol simulations with harmonized emissions from 16 aerosol models. They found that the fraction of the global aerosol burden associated with polar regions varied considerably across models, with a spread of a factor of 10. This is much larger than the globally averaged differences in total aerosol burden, which displays a ±20% spread. Water uptake magnifies the inter-model spread of aerosol dry global burden by a factor of 3, which has important consequences for aerosol sinks and total burden (Textor et al., 2006). Shindell et al. (2008) have recently performed a specific model comparison exercise for the Arctic, to shed some light on the key processes that determine this large model spread. They found that none of the models involved was able to reproduce the seasonal cycle and mean annual concentration of sulfate and black carbon at Alert and Spitsbergen correctly. Simulated concentrations spanned an order of magnitude. The inter-model spread of the sensitivity of the Arctic aerosol burden to emissions in source

regions varied by two orders of magnitude and was larger at higher altitudes than at lower altitudes. Wet removal processes appeared to be responsible for most of the model diversity in the concentrations of sulfate in the Arctic. This conclusion has been further supported by the studies of Bourgeois and Bey (2011), Browse et al. (2012), and Wang et al. (2013) who obtained improved simulations of Arctic aerosols by improving wet and dry deposition schemes in their models.

Our ability to better constrain the various processes affecting the aerosol life cycle in the Arctic critically relies upon the availability of observations. Aircraft campaign provide a wealth of measurements, though they generally cover short periods of time. Routine measurements in the Arctic include ground-based aerosol mass concentration and composition, ground-based measurement of aerosol optical properties (e.g. scattering, absorption) as well as size distribution and hygroscopicity measurements at some stations. Additionally, automated sun-photometers from the Aerosol Robotic Network (AERONET) measure the column aerosol optical depth with good accuracy at several visible wavelengths and provide important constraints on the aerosol burden during the illuminated portion of the year (Holben et al., 1998).

The CALIOP instrument on board the CALIPSO satellite is particularly well-suited for investigating the Arctic. In Chapter 3, we used 6 years of observations of aerosol extinction from CALIOP to examine the spatial and vertical distribution of Arctic aerosols. We found a stronger seasonal cycle in the High Arctic than in the Low Arctic, with a maximum in December-March and very clean conditions in the summer. In the Low Arctic, in contrast, a secondary maximum comparable in magnitude with the winter maximum is observed in July. We found that an important entry way for aerosol pollution is the central Russian Arctic and that the long-range transport of biomass burning and pollution aerosols from Asia dominates the aerosol extinction in spring and summer in the free troposphere. Although the interannual variability of the near-surface

aerosol extinction was found to be small in the High Arctic, we found that the largest observed departures from the 6-year mean occurred throughout the atmospheric column and that they were associated with the largest fluctuations of the Arctic Oscillation during the period considered.

In this chapter, we use the GEOS-Chem chemical transport model (Section 4.2) to better understand the origin and fate of Arctic aerosols. In Section 4.3 we evaluate a 5-year GEOS-Chem aerosol simulation against ground-based observations of aerosol composition and extinction at several Arctic sites. We also compare the model simulation to aircraft aerosol extinction profiles obtained during the ARCTAS aircraft campaign as well as aerosol column optical depth observations at AERONET stations. Then, in Section 4.5, we examine the ability of the model to capture the horizontal and vertical distribution of aerosol extinction as retrieved by CALIOP. After a synthesis of the model evaluation (Section 4.5) we investigate the hypothesis of a missing sea-salt source from sea ice (Section 4.6). Summary and conclusions are presented in Section 4.7.

4.2 Model description

We use the GEOS-Chem global chemical transport model version 9-01-03 (http://geos-chem.org) to simulate coupled aerosol-oxidant tropospheric chemistry. The model is driven by GEOS-5 assimilated meteorological data from the NASA Goddard Earth Observing System (GEOS) with 6-hour temporal resolution, 72 vertical levels, and 0.5° latitude by 0.667° longitude horizontal resolution, re-gridded to a 2°x2.5° horizontally and 47 vertical levels (up to 0.01 hPa) for input to GEOS-Chem. We initialize the model with a 1-year spin up followed by a 5.5 year simulation between June 2006 and December 2011.

The aerosol simulation includes the sulfate-nitrate-ammonium system (Park et al., 2004), organic aerosols (Heald et al., 2011), black carbon (Wang et al., 2011), dust (Fairlie et al., 2007) and sea-salt aerosols (Jaeglé, 2011). The gas-aerosol equilibrium partitioning of total nitrate and

total ammonia is computed using the ISORROPIA II thermodynamic module (Fountoukis and Nenes, 2007) as implemented in GEOS-Chem by Pye et al. (2009). Formation of secondary organic aerosols by reversible partitioning of terpene, isoprene, and aromatics oxidation products is described in Liao et al. (2007) and Henze et al. (2006, 2008). The simulation of black carbon assumes that 80% of emitted BC is hydrophobic, with an e-folding time to conversion to hydrophilic of 1 day.

Global anthropogenic sources are from the EDGAR 3.2FT2000 inventory (Olivier and Berdowski, 2001) for the year 2000. These emissions are overwritten by more recent regional inventories where available: over Asia by the inventory of Zhang et al. (2009) for 2006, over the US by the EPA National Emission Inventory (NEI) for 2005, over Canada by the Criteria Air Contaminant (CAC) for 2005 from Environment Canada (http://www.ec.gc.ca/inrp-npri/), and over Europe by the European monitoring and evaluation programme (EMEP) for 2005. These emissions are scaled to individual years based on available government statistics and trends of surface concentrations and deposition fluxes for those regions where the EDGAR baseline emissions are overwritten (van Donkelaar et al., 2008). Beyond these regions, NOx, SOx and CO are scaled according to CO_2 trends from the Carbon Dioxide Information Analysis Center (http://cdiac.ornl.gov/) following Bey et al. (2001) and Park et al. (2004). For our simulation, scale factors are for year 2006 and are held constant thereafter.

Wet deposition of soluble aerosols follows the scheme of Liu et al. (2001) and includes rainout (in-cloud) and washout (below-cloud) scavenging in convective updrafts and large-scale precipitation. Wang et al. (2011) implemented improvements in the washout parameterization by separating hydrometeors into rain and snow. The scheme calculates the washout rate constant k in the form $k=aP^b$, where P is the precipitation rate (mm h^{-1} water equivalent), and coefficients a and

b account for scavenging by impaction, interception and diffusion. These coefficients are specified based on the type of precipitation (rain or snow) and the aerosol size distribution (accumulation or coarse mode). Accumulation-mode coefficients are used for all aerosols except sea-salt and dust for which the coarse mode coefficients are used. The resulting washout rate constant of snow is 5-25 times larger than for rain for *P* between 0.01-1 mm h^{-1}. Rainout is parametrized based on the areal fraction of a 3-D grid box that experiences precipitation (Liu et al. 2001, with minor corrections by Wang et al., 2011).

Dry deposition is based on the resistance-in-series scheme of Wesely (1989) as implemented by Wang et al. (1998). Aerosol deposition to snow/ice assumes a constant dry deposition velocity of 0.03 cm/s (Fisher et al., 2011).

Optical properties in GEOS-Chem are calculated from the aerosol mass concentration (Martin et al., 2003). For each aerosol specie, the aerosol optical depth (AOD) scales linearly with the aerosol mass according to the formula Tegen and Lacis (1996):

$$AOD = \frac{3}{4}\frac{Q_{ext}M}{\rho\, r_{eff}} = \alpha\, M$$

Where Q_{ext} is the extinction efficiency, ρ is the density of the aerosol, r_{eff} is the effective radius and M the column mass loading in g/m^2. The aerosol species are assumed in external mixing state and the total AOD is then the summation over all aerosol species of each individual AOD.

Each species is assigned a dry refractive index. r_{eff} is calculated by assuming a size distribution, defined by the geometric radius and standard deviation, for each aerosol specie. For sulfate, organic carbon and black carbon, the size distribution consists of a single mode. For sea-salt, two modes exist: accumulation and coarse mode. For dust, there are four modes to reflect the large size variability of size of this primary aerosol. The extinction efficiency is then calculated

from Mie theory assuming spherical shape, and is tabulated at various relative humidities (RH). For the calculation of aerosol optical properties, GEOS-Chem caps the maximum RH at 90%, on the low end of the model distribution (Textor et al., 2006). Figure 4.1 shows the variation of α with RH for the six aerosol species simulated by GEOS-Chem. The contribution of liquid water to the AOD is thus partitioned to each individual species according to its hygroscopicity. For RH>50%, accumulation mode sea-salt is the most efficient light scatterer.

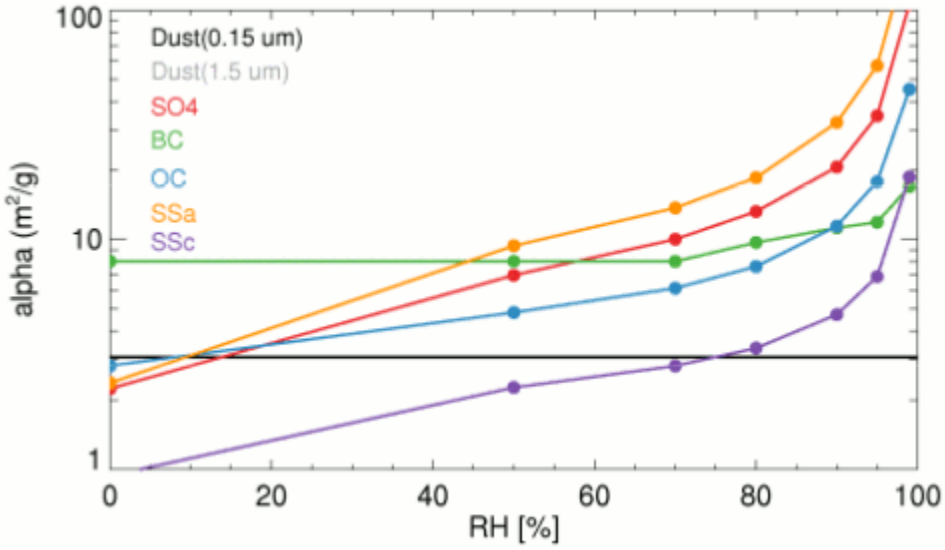

Figure 4.1: Mass extinction coefficient for the GEOS-Chem aerosols at 550 nm and RH=0%.

FlexAOD (http://wiki.seas.harvard.edu/geos-chem/index.php/FlexAOD) is a versatile post-processing tool designed for the GEOS-Chem output. Like GEOS-Chem, it uses Mie Theory to calculate the optical properties. It takes as input from GEOS-Chem the RH and aerosol mass concentrations fields and allows to make different choices for the parameters prescribed by GEOS-Chem to calculate the AOD (e.g. index of refraction, effective radius, etc.). It thus allows the user to re-calculate the AOD without having to re-run the model. In addition, it allows to calculate

certain optical properties that are not a standard GEOS-Chem output (e.g. AOD at multiple wavelengths, single scattering albedo, 180° backscatter, etc.). We use FlexAOD to calculate the 180˚ backscatter at 532 nm, which is needed to apply the CALIOP sensitivity threshold. We also use it to calculate the 550 nm aerosol extinction using a fixed RH for comparison with nephelometer measurements (Section 4.3.2). We ran a sensitivity simulation using updated hygroscopic growth factors based on recent measurements in the European Arctic (Zieger et al., 2013). We briefly discuss the results of this sensitivity simulation in Section 4.3.4.

The GEOS-Chem model has been extensively compared to observations in numerous studies (see publications at http://acmg.seas.harvard.edu/geos/geos_pub.html). For example, the export efficiency of black carbon in the Asian outflow was studied by Park et al. (2003). Over the continental U.S. GEOS-Chem has been used to establish a relationship between observed aerosol concentrations and retrieved aerosol optical depth from satellites (van Donkelaar et al., 2006). Ford et al. (2012) used GEOS-Chem together with satellite retrievals to interpret the aerosol vertical distribution across the Northern Hemisphere. Of particular relevance to our work, GEOS-Chem was used to help interpret observations collected during the 2008 International Polar Year in three recent studies. Fisher et al. (2011) found that southwest Russia and Kazakhstan contribute 30% of the sulfate and ammonium concentrations near the surface in the high Arctic in winter and less in spring (5-15%), and that aerosols originating there are more acidic than those originating in Europe. Wang et al. (2011) focused on estimating the radiative forcing of BC deposition and its seasonal variation. They found roughly equal contributions from anthropogenic and biomass burning aerosols to the BC radiative forcing in spring (+0.6 W/m^2 each) and a large interannual variability of snow BC concentration in spring. These studies show a much greater regional forcing in the eastern Arctic, and potentially larger ecological impacts from acidic deposition in the North

American Arctic and Siberia. GEOS-Chem was able to reproduce the vertical profile and magnitude of organic aerosol concentrations observed during the ARCTAS campaign during spring and summer 2008 to within a factor of 2 (Heald et al., 2011).

4.3 Model evaluation against in situ and AERONET observations

4.3.1 Comparisons with aerosol mass concentrations observations at the surface

In this section, we compare GEOS-Chem with in situ measurements of sulfate and sea-salt concentrations observed at 5 ground sites in the Arctic (Figure 4.2, Table 4.1). Three sites are from the European Monitoring and Evaluation Programme network (EMEP), Pallas, Finland (68°N, 24°E), Oulanka, Finland (66°N, 29°E) and Zeppelin, Spitsbergen (79°N, 12°E). Measurements at Barrow, Alaska (71°N, 157°W) are from the National Ocean Atmospheric Administration (NOAA) Pacific Marine Environmental Laboratory (PMEL); at Alert, Canada (82°N, 62°W) they are from Environment Canada.

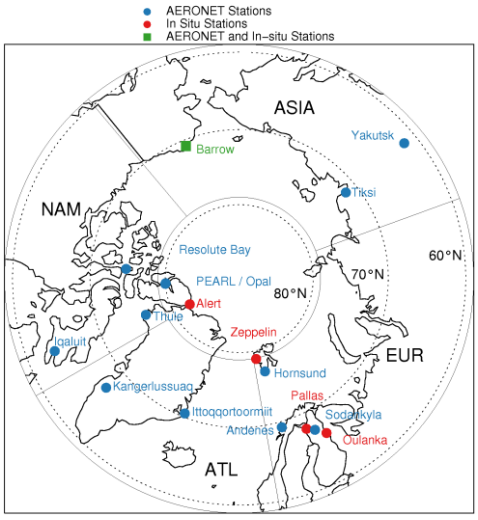

Figure 4.2: Locations of ground-based sites considered in this study: surface sites with in situ observations (red circles) and AERONET stations (blue circles). At Barrow (green square), both AERONET and in situ measurements are taken. The four sectors considered for comparison with the CALIPSO dataset (EUR, NAM, ASIA, ATL) are also shown.

Table 4.1: Summary of the measurements used in this study.

Station	Location	Height AMSL (m)	Time period	Type of measurement[a]
Alert	82.5°N; 62.5°W	220 m	2006-10; 2006-08	Conc; Ext
Andenes	69.3°N;16.0°E	379 m	2008-10	AOD
Barrow	71.3°N;156.6°W	8 m	2006-08; 2006-10; 2006-10	Conc; Ext; AOD
Hornsund	77.0°N; 15.6°W	10 m	2006-10	AOD
Iqaluit	63.6°N;68.5°W	15 m	2008-10	AOD
Ittoqqortoormiit	70.5°N; 22.0°W	68 m	2010	AOD
Kangerlussuaq	67.0°N; 50.6°W	320 m	2008-10	AOD
OPAL	80.0°N; 85.9°W	0 m	2007-10	AOD
Oulanka	66.3°N; 29.4°E	310 m	2007-10	Conc
Pallas Matorova	68.0°N; 24.1°E	340 m	2007-10	Conc
Pallas Sammaltunturi	68.0°N; 24.2°E	560 m	2006-10	Ext
PEARL	80.1°N; 86.4°W	615 m	2007-10	AOD
Resolute Bay	74.7°N; 94.9°W	40 m	2006, 2008-10	AOD
Sodankyla	67.4°N; 26.6°E	184 m	2007	AOD
Thule	76.5°N; 68.8°W	225 m	2007-10	AOD
Tiksi	71.6°N; 128.9°E	0 m	2010	AOD
Yakutsk	61.7°N; 129.4°E	118 m	2006-10	AOD
Zeppelin	78.9°N; 11.9°E	474 m	2006-10	Conc; Ext

(a) Ext: In situ extinction coefficient at 550 nm; Conc: In situ aerosol mass concentration measurements; AOD: column AOD

Aerosol mass concentrations are determined by ion chromatography performed on the aerosol collected on teflon filters. At Alert, filters are changed weekly and measure the total suspended particles (Sirois and Barrie, 1999). At the EMEP sites, filters are changed daily and the aerosol cut-off aerodynamic diameter is 10 μm at ambient RH. At Barrow, the measured aerosol is separated into submicron (particle diameter <1μm) and supermicron (1-10 μm) by a Berner-type cascade impactor after the RH of the sample stream is reduced to below 40% by heating of the inlet (Quinn et al., 2000). At Barrow, the sampling frequency is ~24 hours for submicron and ~7 days for supermicron aerosols. We calculate the non-sea-salt (nss) sulfate by correcting for sea-salt sulfate using the $Na^+/SO_4^=$ ratio in sea water and Na^+ measurements, according to nss-$SO_4^=$ = $[SO_4^=]$ - 0.25$[Na^+]$. Sea-salt mass concentrations are calculated by multiplying the mass concentration of Na^+ by 3.256. All concentrations are referred to standard temperature and pressure

(273.15K, 1013 hPa). For comparison with GEOS-Chem, we define the Mean Normalized Bias (MNB) as:

$$MNB = \frac{1}{N}\sum_{i=1}^{N}\frac{M_i - O_i}{O_i}$$

GEOS-Chem is sampled in the lowest model level of the grid box where the station resides, and monthly means are used.

At all sites, observed nss-sulfate concentrations peak in late-winter/early-spring (Figure 4.3). This seasonality has been well documented and is associated with increased transport from polluted mid-latitudes and less efficient removal processes (Shaw, 1995; Quinn et al., 2007). Spring nss-sulfate concentrations are highest at the low artic sites of Oulanka and Pallas (0.9-1.1 μg/m^3, Figure 4.3h and 4.3l) because of their proximity to pollution sources and lowest at Zeppelin (0.5 μg/m^3, Figure 4.3d) a consequence of its remoteness and higher elevation than most other sites, which frequently puts it outside the boundary layer (Beine et al., 1996). Nss-sulfate concentrations sharply drop to 0.1 μg/m^3 in summer and early autumn at Alert and Zeppelin (Figure 3b, d). These two high Arctic sites exhibit a more marked seasonal cycle than do lower arctic sites, and a distinct annual maximum in spring (March-April). In the Scandinavian Arctic at Pallas and Oulanka, a smaller secondary maximum is observed in the summer (Figure 4.3h, 4.3l).

Our modeled nss-sulfate concentrations are generally in good agreement with observations. At the lower arctic sites of Oulanka and Pallas, modeled annual mean concentrations are within 20% of the observed values (Pallas, Model: 0.77±0.31 μg/m^3; Observations: 0.66±0.24 μg/m^3; Oulanka, Model: 0.95±0.39 μg/m^3; Observations: 0.80±0.25 μg/m^3). Mean annual modeled concentrations are also close to observations at Alert (Model: 0.42±0.16 μg/m^3; Obs: 0.42±0.29 μg/m^3) and within 40% at Barrow (Model: 0.52±0.19 μg/m^3; Obs: 0.36±0.19 μg/m^3). The greatest

model bias occurs at Zeppelin, where sulfate concentrations are overestimated by a factor of (Model: 0.65±0.26 μg/m^3; Obs: 0.30±0.21 μg/m^3) (Figure 4.3d).

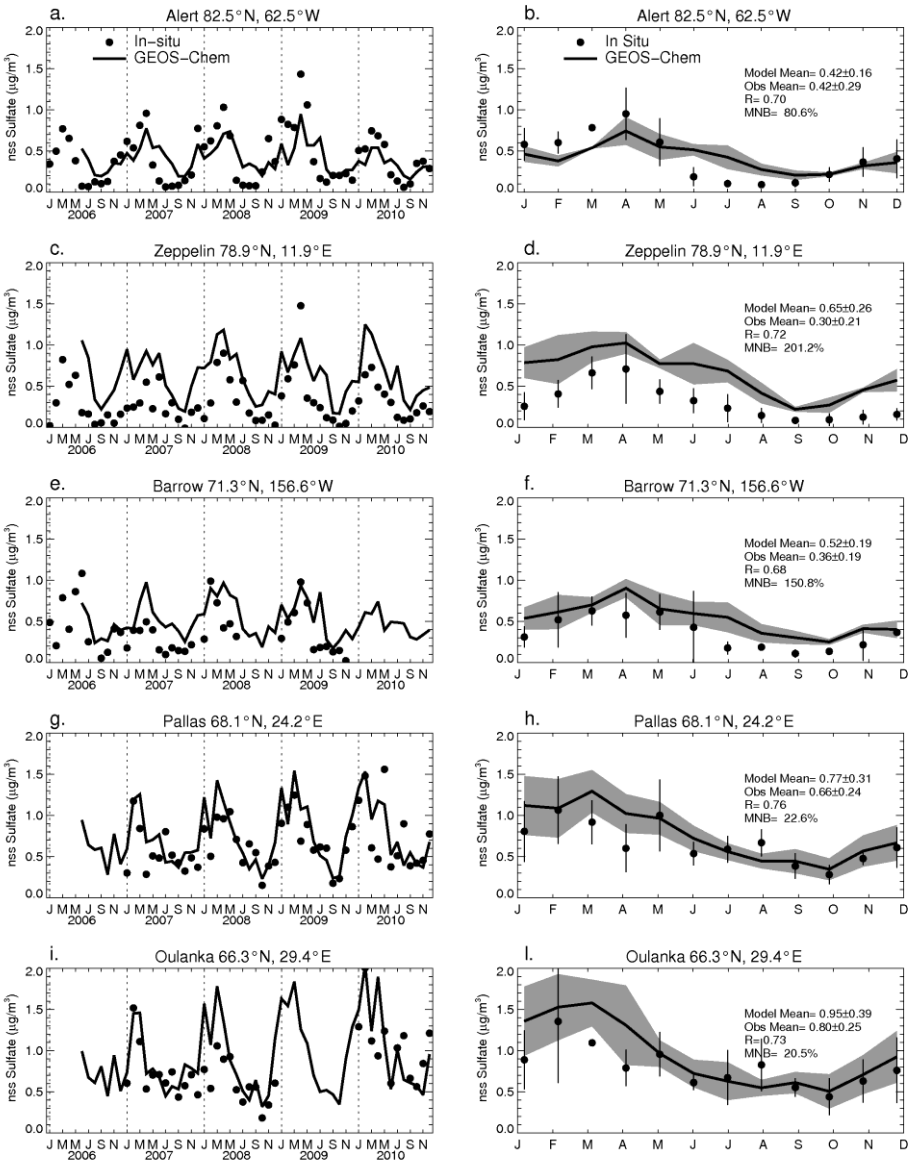

Figure 4.3: Nss-sulfate mass concentrations at 5 Arctic stations for 2006-2010. Left panels: monthly mean observations (circles) and modeled values (lines). Right panels: observed multi-year (2006-2010) monthly means (circles with monthly standard deviation) and model means (black line with grey shading indicating the standard deviation of monthly values).

The model captures the observed seasonal cycle of nss-sulfate, with monthly correlations ranging from R=0.68 at Barrow to R=0.76 at Pallas. The better model performance at the Scandinavian Arctic sites reflects the fact that these sites are mostly influenced by source regions in the European continent where emissions are particularly well constrained (Fisher et al., 2011). In summer, the model overestimates nss-sulfate by a factor 3 at Alert, Zeppelin and Barrow.

Interannual variability (Figure 4.3, left panels) is relatively small at all sites. It is greater in late winter and spring at the peak of the Arctic haze season and very small in September and October. The sites of Pallas and Oulanka show greater interannual variability in spring as they receive biomass burning smoke aerosol from agricultural burning from areas of Europe and central western Asia, whereas at Barrow larger variability is seen in summer given its proximity to boreal forest fire active regions.

Shindell et al. (2008) have performed a model intercomparison exercise which showed that none of the 13 models participating were able to reproduce the seasonal cycle and annual mean nss-sulfate observed at Alert and Zeppelin. Most models underestimated nss-sulfate concentrations by an order of magnitude in winter/spring and overestimated it by a comparable amount in the summer. While GEOS-Chem also overestimates summertime sulfate concentrations at these sites, we find that it reproduces the seasonal cycle and annual mean remarkably well compared to other models. We attribute the ability of GEOS-Chem to reproduce these observations to the improved representation of wet scavenging of aerosols by snow, which is generally not taken into account in most models. Similar results were found by Browse et al. (2012), who compared a chemical transport model with aerosol microphysics to observations in northern Finland as well as Barrow, Alert and Zeppelin. They found that suppressing in-cloud scavenging of soluble aerosols at temperatures below -15°C and at the same time including stratocumulus drizzle scavenging greatly

reduces their model wintertime underestimate while decreasing the summer burden by a factor 3-5.

Observed sea-salt concentrations peak in winter (Figure 4.4). This has been attributed to increased sea-salt production associated with spray and bubble breaking produced by higher surface wind conditions in the northern oceans, followed by transport into the Arctic (Quinn et al., 2003; Tomasi et al., 2007). Higher concentrations are observed at the coastal sites of Alert, Zeppelin and Barrow (winter mean: 1.1-1.7 μg/m^3, Figure 4.4b, d, f) than in the mainland Scandinavian Arctic (winter mean 0.5-0.7 μg/m^3, Figure 4.4l, n). Sea-salt generally decreases in summer as surface wind speed subsides. At Barrow, another peak occurs in early autumn due to coarse mode sea-salt transported from nearby open-ocean sources when sea ice cover is at its minimum (contrast Figures 4.4f, h). Quinn et al. (2003) found that sea-salt aerosols dominate aerosol mass concentrations and control light extinction at Barrow from November through March.

While these observations have a 10 μm diameter cut-off of for sea-salt aerosols, our model simulation includes sea-salt aerosols with a dry aerosol radius up to 8 μm (corresponding to a 30 μm diameter at ambient RH). As aerosol mass is dominated by a few large aerosols, this leads to a large overestimate compared to these observations (Figure 4.4). We conducted a sensitivity simulation and found that reducing the dry aerosol radius to 3 μm (corresponding to the observed cut-off diameter) results in a factor 3 in coarse-mode sea-salt mass concentrations. We thus scale the modeled mass concentration of coarse sea-salt by a factor 0.33 and discuss the resulting comparison to observations. Modeled concentrations are in good agreement with observations in the mainland Scandinavian Arctic. The seasonal cycle at Pallas (Figure 4.4i, 4.4l) is particularly well reproduced (Pallas, Model: 0.39±0.20 μg/m^3; Obs.: 0.50±0.19 μg/m^3). The Mean Normalized Bias at Pallas is -16%. At Alert the model is a factor of 10 too low. GEOS-Chem simulates the late

spring to early autumn concentrations at all Alert, Barrow and Zeppelin. It also captures the marked concentration increase from July to October at Barrow. However the model fails to reproduce the high sea-salt concentrations that are observed from November to April at Alert and Barrow (Figure 4.4b, f). Figures 4.4g, h show the measured submicron sea-salt mass concentrations at Barrow and compare it with GEOS-Chem accumulation-mode sea-salt. From May to October, supermicron aerosols control total sea-salt mass, whereas from November to April it is the submicron aerosols that controls the total concentration. The model captures well the submicron sea-salt concentrations from July to September but largely underestimate submicron concentrations from November to April. Thus, the sea-salt underestimate seen in the annual mean at Barrow (Model: 0.62±0.86 μg/m^3; Obs.: 1.29±0.72 μg/m^3) is largely associated with the submicron fraction (Model: 0.12±0.11 μg/m^3; Obs.: 0.71±0.54 μg/m^3).

Submicron sea-salt aerosols are particularly efficient at scattering light at visible wavelengths. In GEOS-Chem, they represent the most efficient scatterer at RH>50% (Figure 4.1). The large model underestimate in winter has therefore important implications for GEOS-Chem's ability to reproduce the observed light extinction in winter. The comparison between observed and modeled light extinction is the subject of the next section.

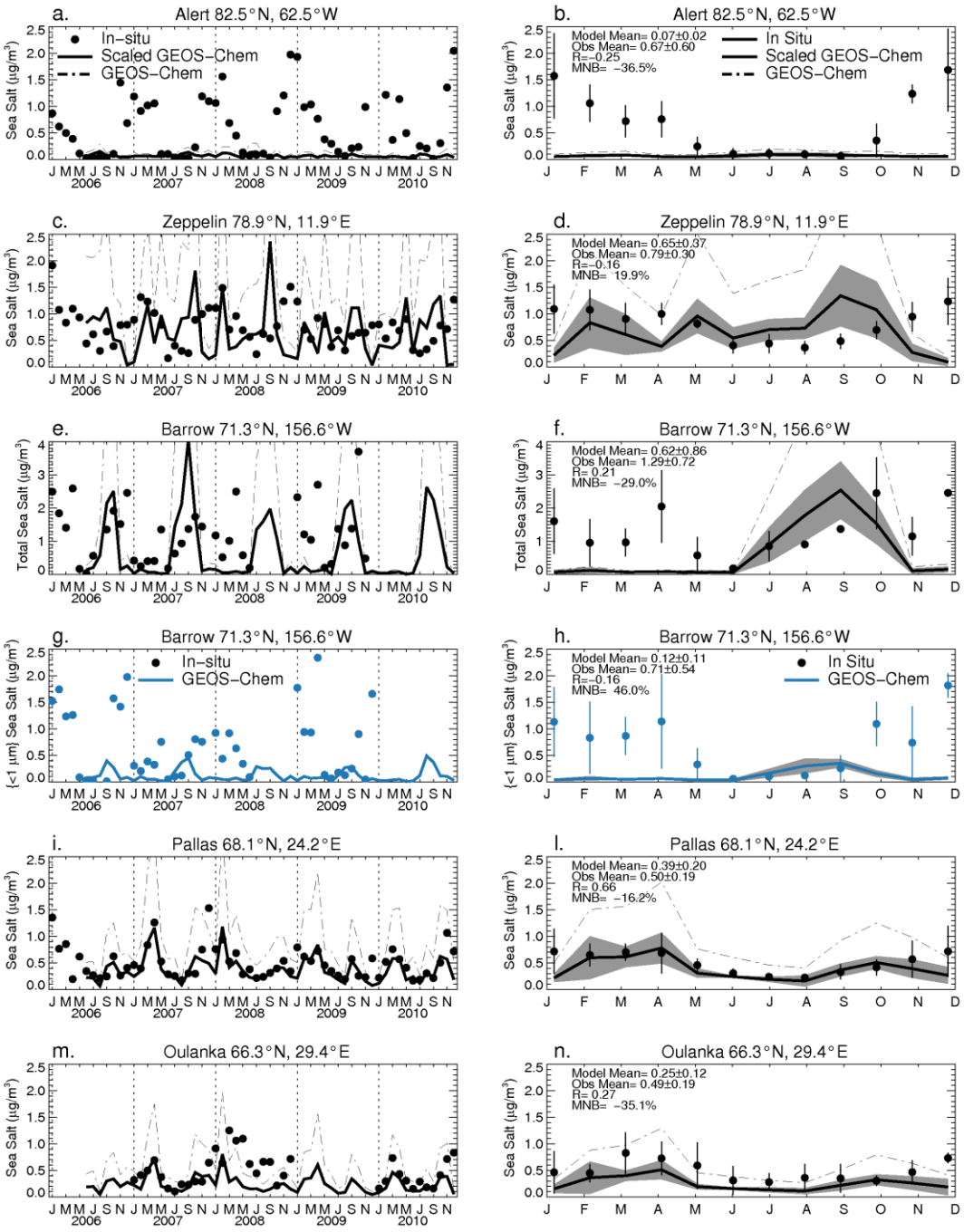

Figure 4.4: Same as Figure 4.3 but for sea salt mass concentrations. A dash-dot black line shows the GEOS-Chem total sea-salt concentrations before the coarse mode concentrations are multiplied by a factor 0.33 to estimate the 0-10 μm mass concentration. Blue colors are used for the sea-salt submicron fraction (accumulation mode for GEOS-Chem).

4.3.2 Comparison with in situ extinction measurements at the surface

We compare the simulated 550 nm dry extinction to in situ measurements of scattering and absorption at Barrow, Alert, and Pallas. Scattering is measured by nephelometers. Ambient air is drawn into the nephelometers via a heated inlet, which desiccates the aerosols by decreasing RH to values below 30-40%. The cut-off diameter at the inlet is 10 μm (Delene and Ogren, 2002; Garrett et al. 2011). The sample volume is then illuminated with green light (550 nm); the scattering by aerosol particles is integrated over a broad range of angles (7-170°) to yield the scattering coefficient, b_{scat}. The absorption coefficient (b_{abs}) is also measured by a particle soot absorption photometer at Barrow and Alert. The extinction coefficient is obtained by adding b_{scat} and b_{abs}. When absorption measurements are not available we assume $b_{ext} \cong b_{scat}$. This is a reasonable approximation since b_{abs} is generally less than 5% of b_{scat} for Arctic aerosols (Delene and Ogren, 2002). Whereas for Barrow the data is already daily-averaged, for Alert hourly averages are used, and we require at least 8 measurements per day to calculate the daily mean. At Pallas we use the scattering coefficient to approximate the extinction. Mean single scattering albedos measured at a coastal Norwegian site in the vicinity of Pallas are greater than 0.91 (Montilla et al., 2011) indicating that this approximation introduces an error that is less than 10%.

For comparison to observations, we calculate the modeled extinction coefficient using a fixed RH of 40%, which is the RH upper limit inside the nephelometer inlet for Barrow and Alert. For Pallas however, the nephelometer internal RH is recorded, and shows a marked seasonal cycle and consistently lower values winter (RH=5-15%) than in summer (RH=30-40%). At that station, we use RH=15% for October to April, RH=30% in May-June, and RH=40% in July to September for comparison to observations.

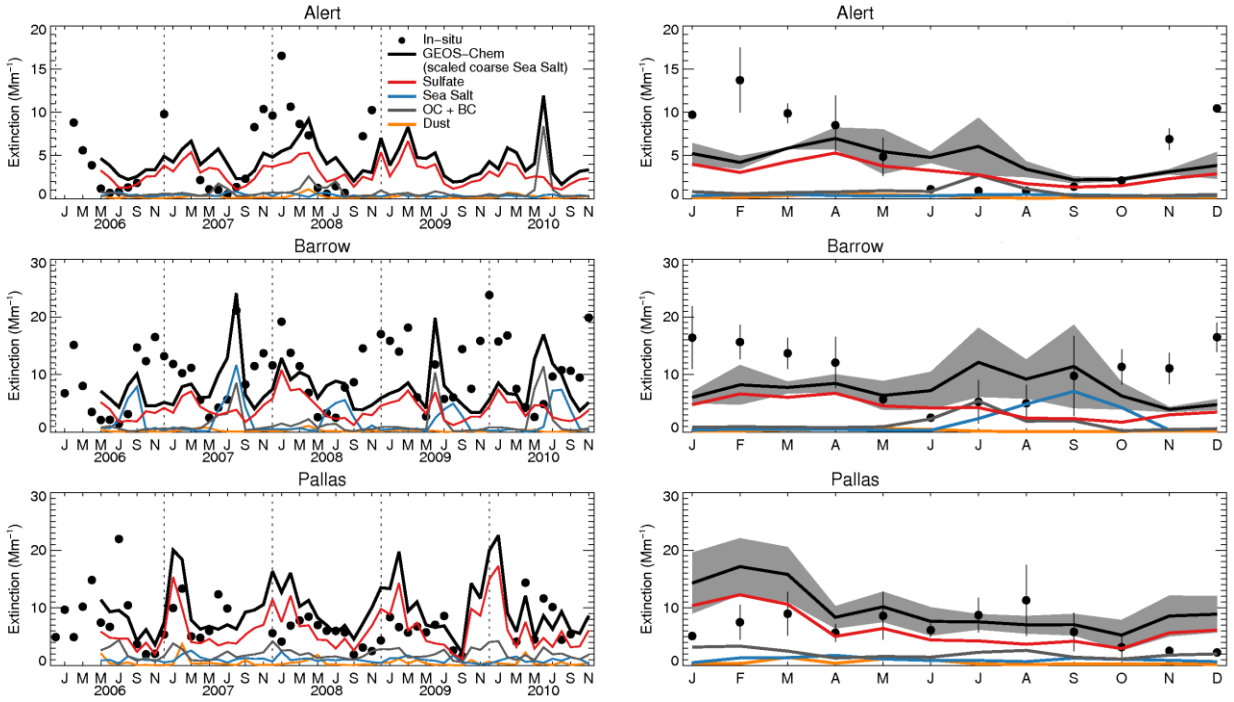

Figure 4.5**:** Comparison of 550 nm light extinction at Alert (top), Barrow (middle) and Pallas (bottom). Left plots show monthly mean observed extinction (black circles) and modeled total extinction (black line) broken down by aerosol species (colored lines). At least 5 days are required to calculate the monthly mean for the observations, and the model is sampled only on days with observations. Plots on the right show the multi-year means. The monthly inter-annual standard deviations are indicated by error bars for the observations and a gray shading for the model. We used the period 06/2006 to 12/2010 to calculate the model standard deviations and in situ observations at Barrow and Pallas. For observations at Alert we use 2004-2008.

At Alert and Barrow, the observed extinction shows a winter-spring maximum and a summer minimum (Figure 4.5, top and middle rows), similar to the seasonality of nss-sulfate (Figure 4.3b, d). December to April mean extinction are slightly higher at Barrow (14 Mm^{-1}) than at Alert (11 Mm^{-1}). The difference between these two sites is much larger during summer, with 5 Mm^{-1} observed at Barrow compared to 1 Mm^{-1} at Alert. At Pallas (Figure 4.5, bottom row), extinction is generally higher and more variable in summer than in winter (Aaltonen et al., 2006),

due to the inflow of smoke aerosols from eastern Europe and Russia in summer and efficient wet removal from the North Atlantic storm track in winter.

At Alert and Barrow, the modeled annual-mean extinction values (Alert: 4.4 Mm^{-1}; Barrow: 7.6 Mm^{-1}) are close to observed values (Alert: 5.9 Mm^{-1}; Barrow: 10 Mm^{-1}). However, the model fails to simulate the seasonal cycle of extinction at these stations. Extinction in autumn and spring is well simulated but large discrepancies occur in winter and summer. In winter, GEOS-Chem underestimates extinction by a factor 2-3 (Figure 4.4). We believe that this is related to the underestimate of sea-salt concentrations (section 4.3.1). Indeed, at Barrow GEOS-Chem underestimates the fine mode sea-salt by ~1 $\mu g/m^3$ during winter-spring. Given the mass extinction efficiency of accumulation mode sea-salt in the model at 40% RH is α =7 m^2/g (Figure 4.1), this corresponds to an extinction underestimate of 7 Mm^{-1}, an amount comparable with the magnitude of the model underestimate at Barrow.

In summer, the model overestimates the observed extinction at Barrow and Alert by a factor of 2-5. Part of this could be due to the GEOS-Chem sulfate concentration overestimate (Figure 4.3) but could also be caused by the assumption of a size distribution constant in time for sulfate. Measurements of Arctic aerosol size distributions show a transition from late spring to summer from accumulation-mode to smaller and less efficient at scattering Aitken-mode particles (Engvall et al., 2008). Quinn et al. (2002) measured the Ångström exponent (a proxy for particle size) at Barrow and found a seasonal cycle indicative of smaller aerosol in summer than in winter. They found however that the mass scattering efficiency of nss-$SO_4^=$ does not vary much during the course of the year, indicating a fairly constant size distribution in time. Thus it is unlikely that the summer transition causes an overestimate of sulfate extinction. Following a similar argument as it was previously done for sea-salt at Barrow, the sulfate extinction model overestimate at Alert is

found to be 1-2 Mm^{-1}, which is insufficient to close the gap with observations (3-5 Mm^{-1}). Another possibility is that the model overestimates organic carbon concentrations at these sites.

At Pallas, the modeled extinction agrees with the observations in the summer. However, between November and March, the model is a factor 2-3 higher than observations. Given that the GEOS-Chem model reproduces the observed sulfate and sea-salt mass concentrations, it is unclear why there is such disagreement with the observed extinction. One possible explanation is that aerosol scattering measurements are taken at Pallas Sammaltunturi (560 m amsl), which lies on top of a hill (Aaltonen et al., 2006), whereas aerosol concentrations measurements are taken at the lower elevation site of Pallas Matorova (340 m amsl, Table 4.1). We speculate that when strong wintertime inversions occur, the higher elevation site could be sampling cleaner free tropospheric air (and thus a lower extinction) than the site in the valley below. As the model is sampled at the surface, its concentrations are consistent with the lower elevation site.

Model simulations indicate that sulfate generally dominates light extinction at all stations (Figure 4.5). During summer, organic aerosols transported from biomass burning regions have an extinction comparable to sulfate, with the exception of the July to October at Barrow, when and local sea-salt sources exert a larger influence on total light extinction. Organic carbon contributes to extinction a comparable amount as sulfate at Barrow and Alert. Between August and October at Barrow, sea-salt dominate the modeled extinction.

4.3.3 Comparison with in situ extinction measurements during ARCTAS

In this section, we compare the GEOS-Chem extinction profiles to the in situ extinction profiles measured during NASA's ARCTAS (Arctic Research of the Composition of the Troposphere from Aircraft and Satellites) campaign, which took place in April and July 2008 (Jacob et al., 2010). We use in situ scattering and absorption measurements taken on board the DC-8 aircraft. The

scattering coefficient was measured via nephelometer (Anderson et al., 1998) and corrected to ambient RH as described in Shinozuka et al. (2011). The extinction is obtained by adding the scattering coefficient at ambient RH to the single–particle soot photometer absorption measurements (Clarke et al., 2004). Figure 4.6 shows the DC-8 flight tracks during the spring and summer campaigns.

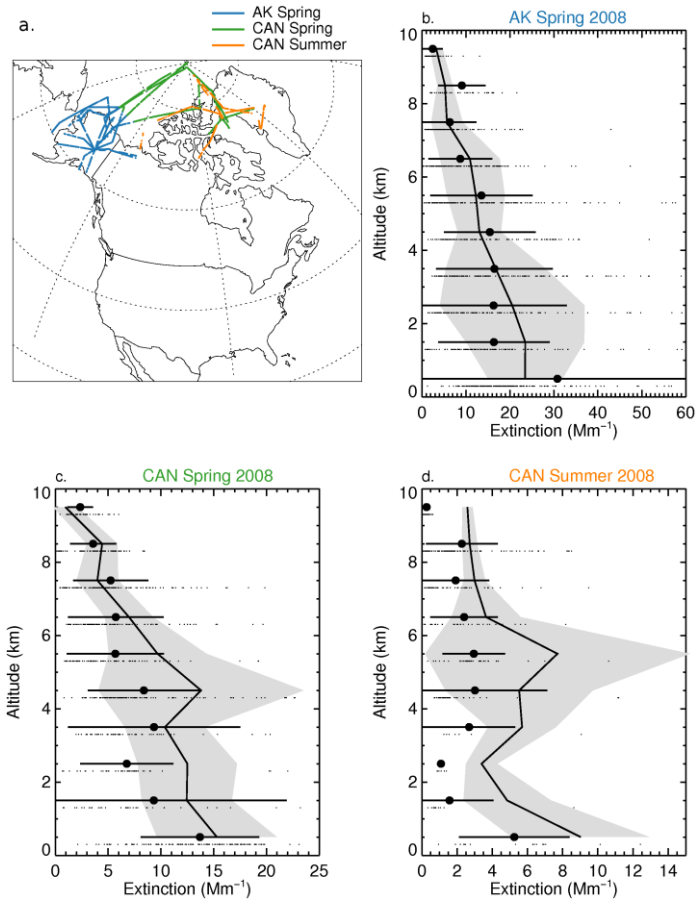

Figure 4.6: Extinction profiles measured on-board the DC-8 during the ARCTAS campaign in April and July 2008. (a) DC-8 flight tracks for the Alaskan (AK) region in April (blue), the high Canadian Arctic (CAN) in April (green) and July (orange). (b) Mean vertical extinction profile over AK in April. Observations are shown with filled dots with horizontal bars marking the standard deviation of 1-min averaged observations. The black solid line shows the mean modeled extinction profile sampled along the flight track, with the gray shading indicating the standard deviation of the model. Dense plumes (measured [CO]>200 ppbv) are excluded from the comparison. (c) Same as (b) but for CAN in spring. (d) Same as (b) but for CAN in July.

During spring 2008, the measured extinction was largest near the surface and generally decreased with height both over the Alaskan and Canadian Arctic (denoted as AK and CAN on Figure 4.6b, c). A secondary peak is observed at 4 km (AK: 17 Mm^{-1}; CAN: 10 Mm^{-1}) caused by long-range transport of agricultural crop burning smoke in Russia and Kazakhstan (Warneke et al., 2009). We extract GEOS-Chem extinction profiles by sampling the model along the aircraft flight tracks. GEOS-Chem captures the shapes of the extinction profiles over both Alaska and the Canadian Arctic during spring and is within one standard deviation of the observations at all altitudes. Fisher et al. (2011) used GEOS-Chem to study the sources of arctic sulfate and ammonium throughout the troposphere during the springtime ARCTAS campaign. They found that both observed and simulated sulfate and ammonium concentrations profiles were relatively flat except for a small enhancement at 2-5 km, which is qualitatively in agreement with our extinction comparison over both AK and CAN. In their study, anthropogenic emission from East Asia were found to explain 30-40% of the sulfate and ammonium above 2 km, with biomass burning explaining a quarter of ammonium at 2-5 km.

During summer in the CAN region, the observed extinction is a factor 2-6 lower than in spring. The observed extinction peaks at 4-5 km (3 Mm^{-1}), associated with the specific targeting of smoke plumes from north American forest fires during the ARCTAS summer campaign (Bian et al., 2013). GEOS-Chem captures the magnitude and altitude of this peak and the shape of the extinction profile, although the modeled extinction is higher than observed at all altitudes which results in a factor of 2 overestimate of column AOD. The shortness of the summer campaign (4 days) and the specific targeting of smoke plumes however do not permit a more robust determination of any model bias through comparisons with in situ observations.

4.3.4 Comparison with AERONET

The Aerosol Robotic Network is a global network of remotely operated sun-photometers (Holben et al., 1998) which provides measurements of the column AOD at multiple wavelengths during daytime. Here we use the level-2 column AOD at 550 and 500 nm, interpolated to 532 nm for comparison with GEOS-Chem assuming an inverse wavelength relationship. The typical AOD uncertainty is $<\pm 0.01$ under clear-sky conditions (Holben et al., 1998). We compare model and observed column AOD at the 13 AERONET stations located north of 60°N (Figure 4.2).

Figure 4.7 shows the observed seasonal cycle of AOD at 12 AERONET stations (we combine the stations of PEARL and OPAL since they are nearly co-located). The record length spans 1 to 4 years, depending on the site (Table 4.1). The availability of sunlight dictates the length of the measurement season, and thus lower latitude sites (e.g. Yakutsk) span a longer period than high latitude ones (e.g. PEARL). Observed AOD values at AERONET sites range from 0.05-0.06 at sites in the high Arctic and Greenland (PEARL/OPAL, Thule, Ittoqqortoormiit, Kangerlussuaq) to 0.09-0.12 at the lower Arctic sites of Barrow, Andenes, and Yakutsk. The Siberian station of Yakutsk exhibits the highest observed AOD.

GEOS-Chem reproduces the March to September mean and daily variability of the column AOD to within 20% at nearly all sites (Figure 4.7). The MNB ranges from -0.5% at Yakutsk to +33% at Iqaluit but is within 20% at most sites. Correlations of daily timeseries are close to 0.7 at stations with longer records in the eastern Arctic (e.g. PEARL/OPAL, Thule), and are generally lower for stations with short records (e.g. Tiksi and Ittoqqortoormiit) and in the western Arctic (Barrow, Resolute Bay).

Figure 4.8 shows the daily time series of modeled and observed AOD at a subset of four AERONET stations. These stations show a large day-to-day and interannual variability, which are

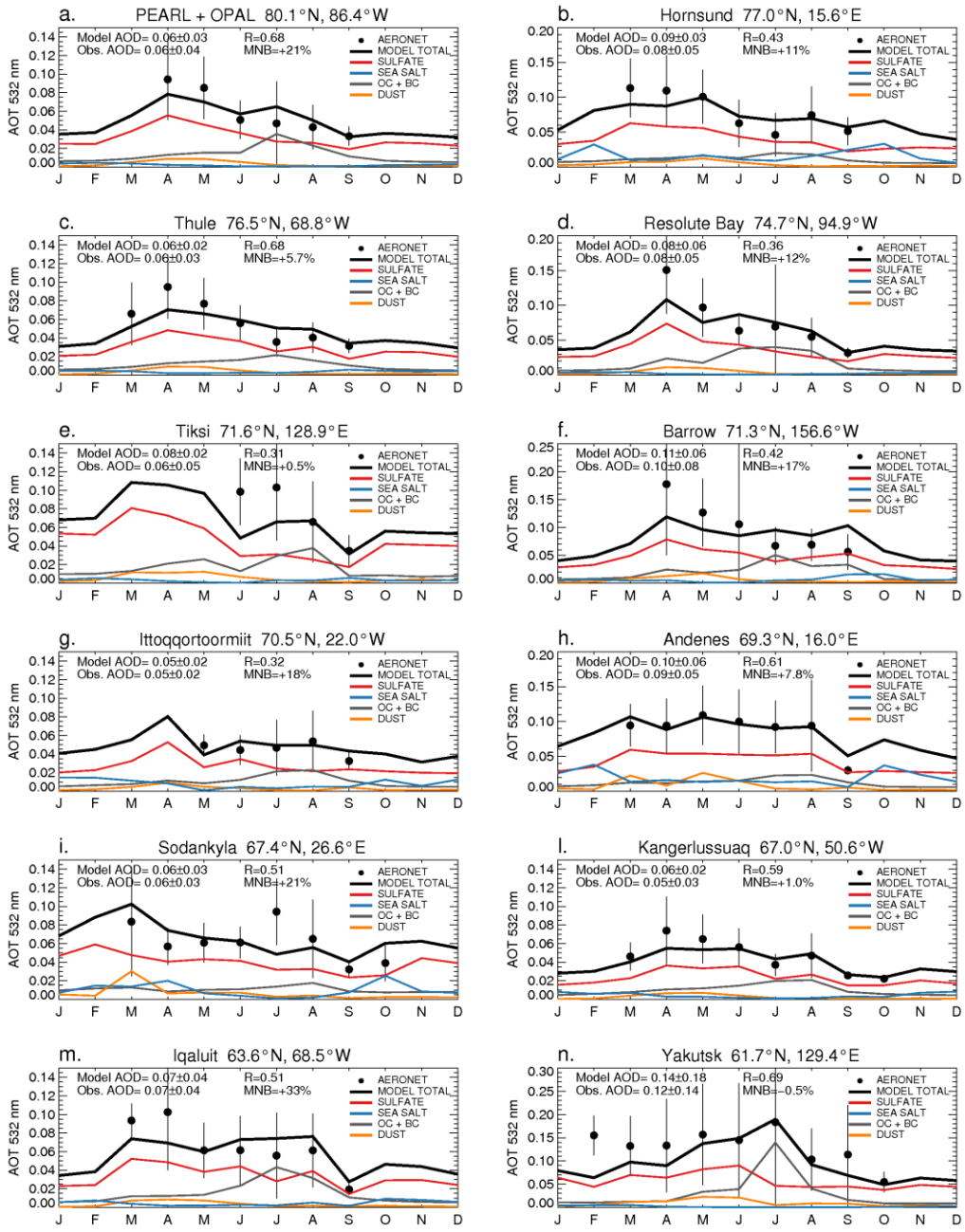

Figure 4.7: Multi-year monthly mean column AOD at AERONET stations (locations indicated in Figure 4.1). Full circles show the observed multi-year monthly mean column AOD, with vertical bars indicating the standard deviation of daily observations. GEOS-Chem column AOD is indicated by a black line. Colored lines indicate the column AOD associated with the various aerosol species. Also shown are the correlation coefficients between daily modeled and observed values (R), the mean normalized bias (MNB) and the annual observed and modeled means and standard deviations at all sites.

well captured by GEOS-Chem. Variability of daily observations is smaller at the higher Arctic latitudes (PEARL and Barrow, Figure 4.8a, b) than at lower latitudes (Andenes and Yakutsk, Figure 4.8c, d). The lower latitude sites also show a large variability in summer possibly reflecting the relative closeness of these sites to biomass burning sources (van der Werf et al., 2009). The model does not reproduce the sulfate column AOD maximum 1-2 months after the volcanic eruptions of Kasatochi (August 7, 2008) and Sarychev (June 2009), which is evident in Figure 4.8a, c, d.

Besides reproducing the annual mean and temporal variability, GEOS-Chem successfully simulates the seasonal cycle of the column AOD. The seasonal cycle exhibits a spring maximum at higher latitude sites (Figure 4.7a,b,c,d,f) and is flatter at lower Arctic sites, with often comparable AODs in spring and summer (Figure 4.7g,h,i,l,n). We cluster the AERONET stations by geographic location and season. We combine Andenes, Sodankyla and Hornsund in a "Europe" cluster. Similarly, we define "Siberia" contains Tiksi and Yakutsk and "North America" Iqaluit, Kangerlussuaq, Ittoqqortoormiit, Barrow, Thule, OPAL, PEARL and Resolute Bay. We exclude the months of September and October 2008 and July –October 2009 because of the high model bias due to the volcanic eruptions.

Table 4.2 shows a summary of the comparison for monthly mean column AOD by geographical sector and season. The model underestimates column AOD in spring (MNB=-16%) and overestimates it in summer (MNB=+15%). The model bias is smaller for the European cluster than the North American and Siberian clusters in both seasons, although correlations are also significantly smaller there. The Siberian cluster shows a consistently negative bias in both seasons though stronger in spring (-21%) than in summer (-9%) and high correlations (R=0.79-0.85).

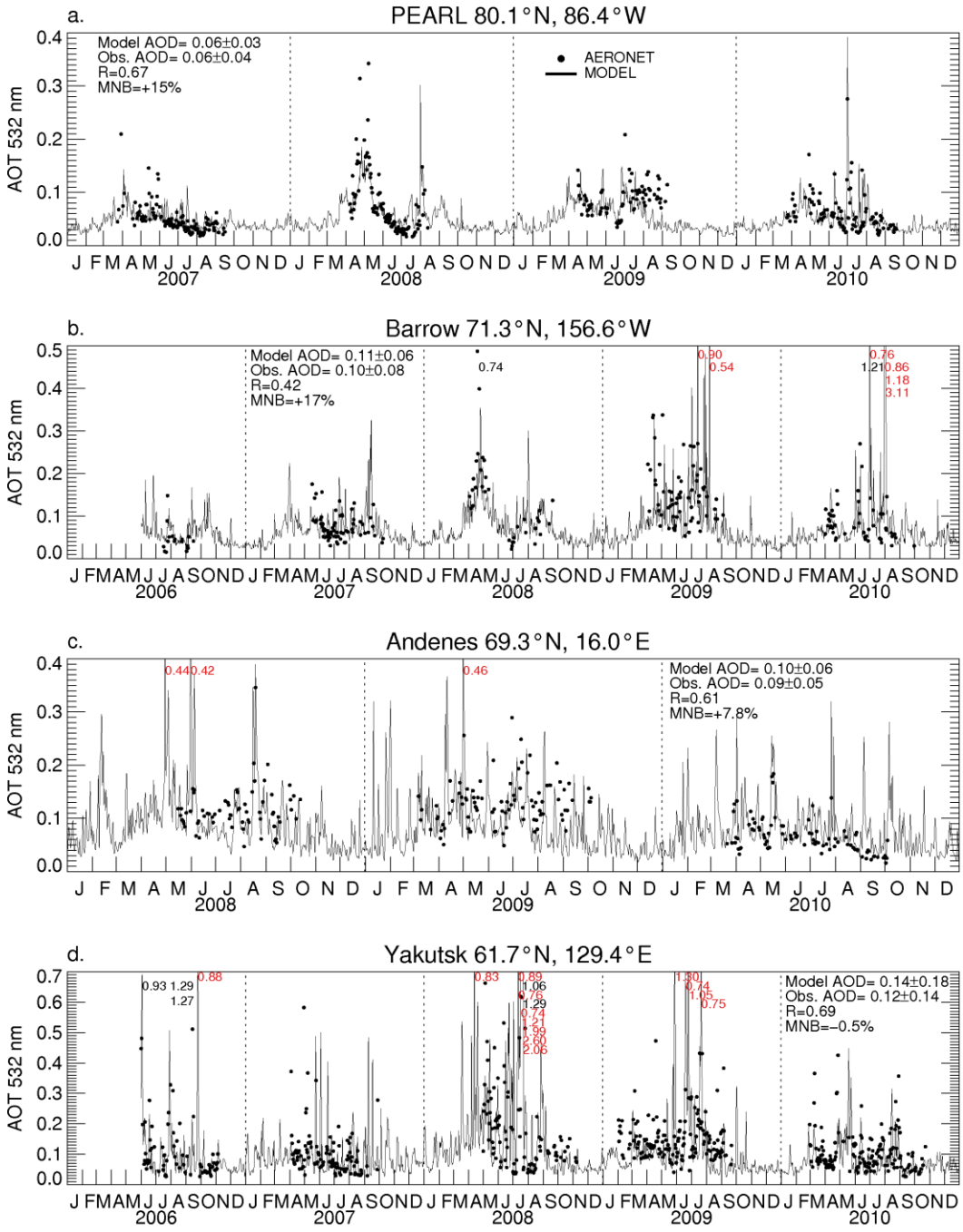

Figure 4.8: Daily column AOD at 532 nm at a subset of four AERONET stations: PEARL, Barrow, Andenes, and Yakutsk Black circles indicate observations, while green circles indicating model values. Red (black) numbers indicate modeled (observed) AOD values larger than the plot scale.

The North American cluster displays the highest bias of all clusters as well as the most dramatic change between spring and summer. In spring, modeled column AOD is 20% lower than observed, but in summer the model bias changes sign (MNB= +23%). The positive bias in summer is consistent with the extinction overestimate at the surface (Figure 4.5) but also suggests a smaller relative contribution of low-level aerosol to the column AOD than in winter. The dramatic spring to summer transition in column AOD model bias is analogous to the one observed at Alert and Barrow for the surface extinction, suggesting that low-level extinction strongly controls the column AOD.

Table 4.2: Monthly mean statistics for the comparison between GEOS-Chem and AERONET.

	MAM			*JJA*		
	MNB (%)	R	N	MNB (%)	R	N
EUROPE	-1.9	0.54	20	+5.5	0.46	17
N.AMERICA	-20.2	0.93	47	+22.8	0.60	64
SIBERIA	-20.7	0.85	9	-9.4	0.79	16
ALL	**-15.5**	**0.85**	**76**	**+14.5**	**0.76**	**97**

The comparison excludes months affected by volcanic eruptions. Europe is defined as the union of Andenes, Sodankyla and Hornsund; North America is the union of Iqaluit, Kangerlussuaq, Ittoqqortoormiit, Barrow, Thule, OPAL, PEARL and Resolute Bay; Siberia is the union of Yakutsk and Tiksi. R indicates the correlation of monthly means, and N indicates the number of months used in the statistic.

4.4 Comparisons against satellite observations

In this section we use the horizontal and vertical distribution of aerosol extinction retrieved by CALIOP for the period of our model simulation (June 2006-December 2010). We grid the CALIOP extinction over the Arctic (poleward of 60°N) on a grid with 200-m vertical resolution and a 2°x2.5° horizontal resolution (same horizontal grid as GEOS-Chem). We use the nighttime-equivalent extinction that was described in Chapter 3.2, which assumes that all undetected aerosols

have an extinction of 0 Mm^{-1}. Similarly, in GEOS-Chem, we set the aerosol extinction to 0 Mm^{-1} whenever the corresponding aerosol backscatter falls below the CALIOP sensitivity threshold (Winker et al., 2009). To compare GEOS-Chem to CALIOP observations, we sample the model along CALIOP orbits and interpolate the modeled extinction and backscatter on a 200 m vertical grid. Since the assumption of spherical size can result in an underestimate of the extinction to backscatter ratio compared to measurements (Mattis et al., 2002; Liu et al., 2002), we divide the dust backscatter (from FlexAOD) by a factor 2.5 as in Yu et al. (2010). This correction does not affect the relative contribution of dust to the total AOD but only reduces the value of the total backscatter resulting in fewer aerosol layers surviving the application of the CALIOP's threshold.

Figure 4.9 shows the CALIOP multi-year seasonal cycle of aerosol extinction averaged over the Low Arctic (60-70°N) and the High Arctic (70-82°N). Near the surface (0-2 km), the zonally-averaged annual mean extinction is roughly a factor of 2 higher in the Low Arctic than in the High Arctic (Low Arctic: 13±2.9 Mm^{-1}; High Arctic 7.1±5.2 Mm^{-1}), but both regions display a maximum in winter-spring of about 15 Mm^{-1} (Figure 4.9a, b). In the Low Arctic (Figure 4.9a), a maximum is also seen in summer, caused by boreal forest fire smoke, which brings the extinction to values comparable to those seen in winter. In the High Arctic (Figure 4.9b), in contrast, the extinction rapidly decreases down to 1-3 Mm^{-1} in summer, similar to ground-based observations at Alert and Barrow (Figure 4.5).

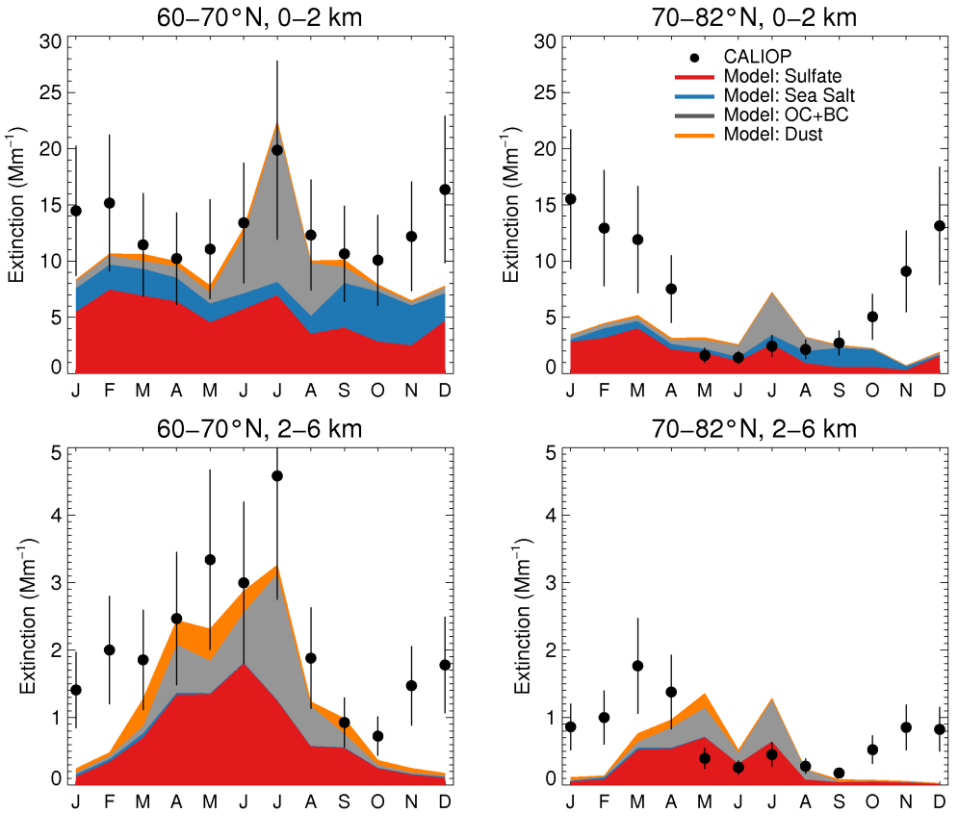

Figure 4.9: Annual cycle of mean extinction for the Low and High Arctic at 0-2 km (a, b) and 2-6 km (c, d). CALIOP observations are indicated with full circles with a vertical bar indicating the error uncertainty associated with the selection of the lidar ratio (±40%). Model extinction for the various aerosol species are indicated with color shadings.

In the mid-upper troposphere (2-6 km, Figure 4.9, bottom panels), the CALIOP annual mean extinction is 2.1±1.1 Mm^{-1} in the Low Arctic, 3 times higher than in the High Arctic (0.7±0.5 Mm^{-1}). At 2-6 km in the Low Arctic, extinction increases through spring and peaks in May-July due to forest fire smoke. At higher Arctic latitudes the extinction peaks in March and April (1-2 Mm^{-1}), associated with increased transport from source regions in the mid-latitudes in Europe, Russia and East Asia. The different seasonal cycles observed between the Low and High arctic troposphere in summer likely reflect the much reduced transport efficiency in this season and

efficient wet removal processes at play (Stohl et al., 2006; Garrett et al., 2011; Browse et al., 2012; Bian et al., 2013).

In the Low Arctic, the GEOS-Chem extinction at 0-2 km and 2-6 km is generally consistent with CALIOP, lying within 20-40% of the retrievals (Figure 4.9a, c). In the Low Arctic, GEOS-Chem reproduces the seasonal cycle both in the lower and middle troposphere, though it appears to underestimate the extinction from November to February at both altitudes.

In the High Arctic at 0-2 km (Figure 4.9b), the GEOS-Chem annual mean extinction is a factor of 2 lower than CALIOP extinction (GEOS-Chem: 3.3±1.7 Mm^{-1}; CALIOP 7.1±5.2 Mm^{-1}). GEOS-Chem does not reproduce the observed seasonal cycle: the model underestimates CALIOP extinction by factors of 2-10 between October and April, but overestimates CALIOP extinction during summer by a factor of 2. At 2-6 km altitude (Figure 4.9d), the modeled seasonal cycle maximizes in summer, while CALIOP shows a spring maximum. The model underestimate is most severe during winter in the High Arctic at 2-6 km.

In order to more accurately evaluate the model bias, we need to take into account the non-linear dependence of applying the CALIOP sensitivity threshold to GEOS-Chem. Take the hypothetical case where the CALIOP extinction is 10% above the sensitivity threshold, but modeled extinction is 10% lower than the threshold. Applying the threshold to GEOS-Chem (setting the extinction to zero) thus leads to an apparent very large model underestimate of CALIOP extinction (100%) while in reality the model was only ~20% lower than CALIOP. We address this by scaling the modeled extinction by constant factors (ranging from 0.25 to 3) prior to applying the CALIOP sensitivity threshold. We find that in the High Arctic, GEOS-Chem underestimates the extinction by a factor 2 to 3 from November to January at 0-2 km, and of by a factor ~2 at 2-6 km, significantly lower than the factor 4-10 that would be inferred from Figure

4.9b, d. During summer, we find that the magnitude of the summer overestimate does not exceed 40% at 0-2 km and 30% at 2-6 from May to August.

Next, we focus on the spatial distribution of extinction during individual seasons to examine the comparison between GEOS-Chem and CALIOP (Figures 4.10 and 4.11).

4.4.1 Winter

During winter at 0-2 km altitude, CALIOP retrievals show two regions where the extinction is enhanced: the North Atlantic Ocean and central Russian Arctic, where extinction reaches up to 35 Mm^{-1} (Figure 4.9, top left panel). The enhancement in the north Atlantic is associated with local production of sea-salt aerosols, which maximizes in winter due to stronger surface winds associated with the storm track. The central Russian enhancement is due to low-level long-range transport of pollution along the Siberian anticyclone which is also strongest in winter. The eastern sector of the Arctic Ocean shows values that are somewhat higher (15-20 Mm^{-1}) than in the Western sector (10-15 Mm^{-1}).

GEOS-Chem reproduces the magnitude of the extinction enhancement in the North Atlantic. It also qualitatively captures the spatial distribution observed by CALIOP with a gradient in extinction between the eastern and western Arctic. However, the modeled extinction is significantly lower than CALIOP over the Arctic Ocean (by 10-15 Mm^{-1}). The model also underestimates CALIOP extinction over central Russia (by 15-25 Mm^{-1}). This suggests that some anthropogenic sources might be missing in our emission inventory for this region, as will be discussed in Section 4.5.

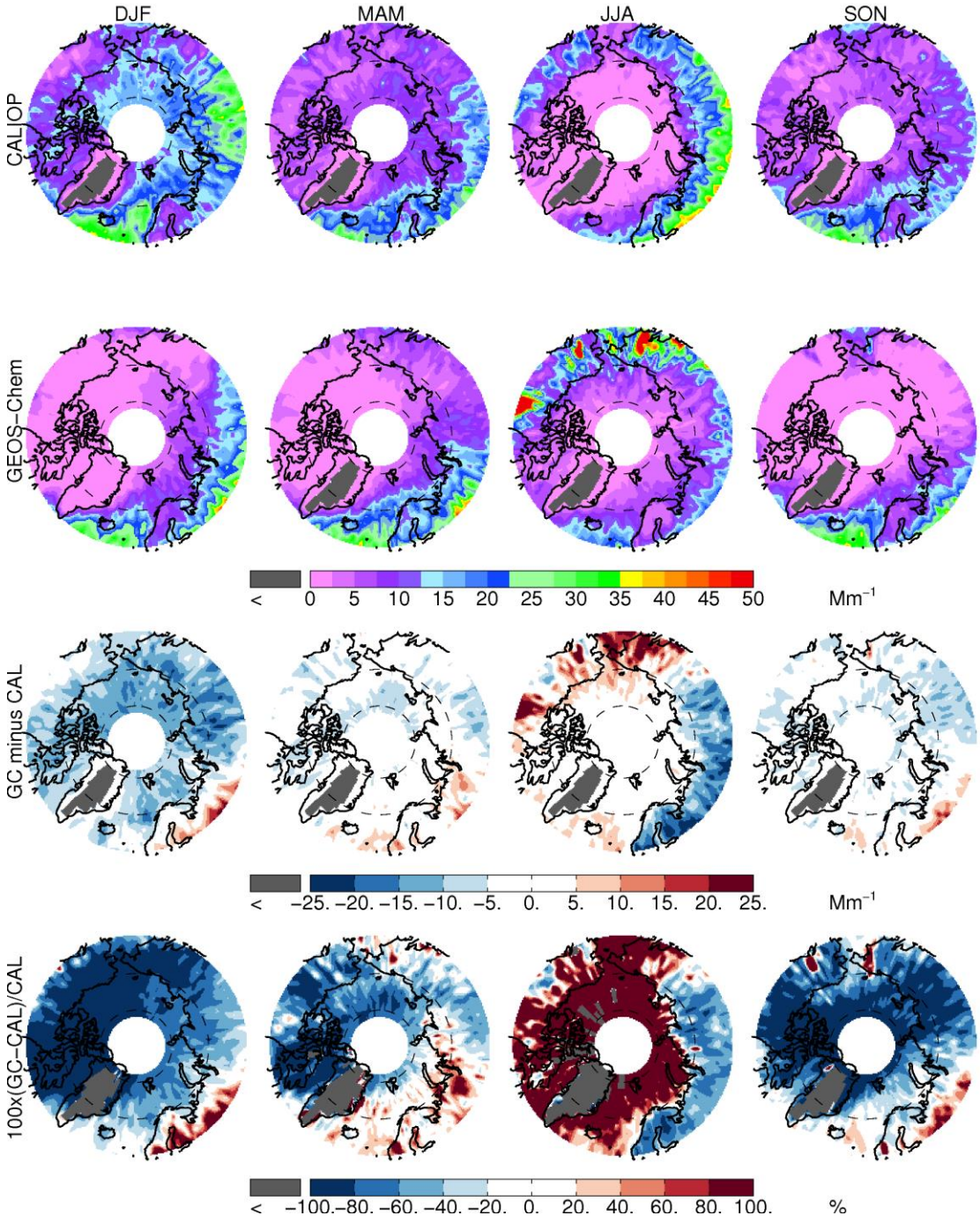

Figure 4.10: Seasonally averaged distribution of extinction at 0-2 km in winter (DJF), spring (MAM), summer (JJA), and fall (SON), from left to right. Top row: CALIOP observations. Second row: GEOS-Chem model. Third row: difference between GEOS-Chem and CALIOP. Bottom row: percent difference between GEOS-Chem and CALIOP.

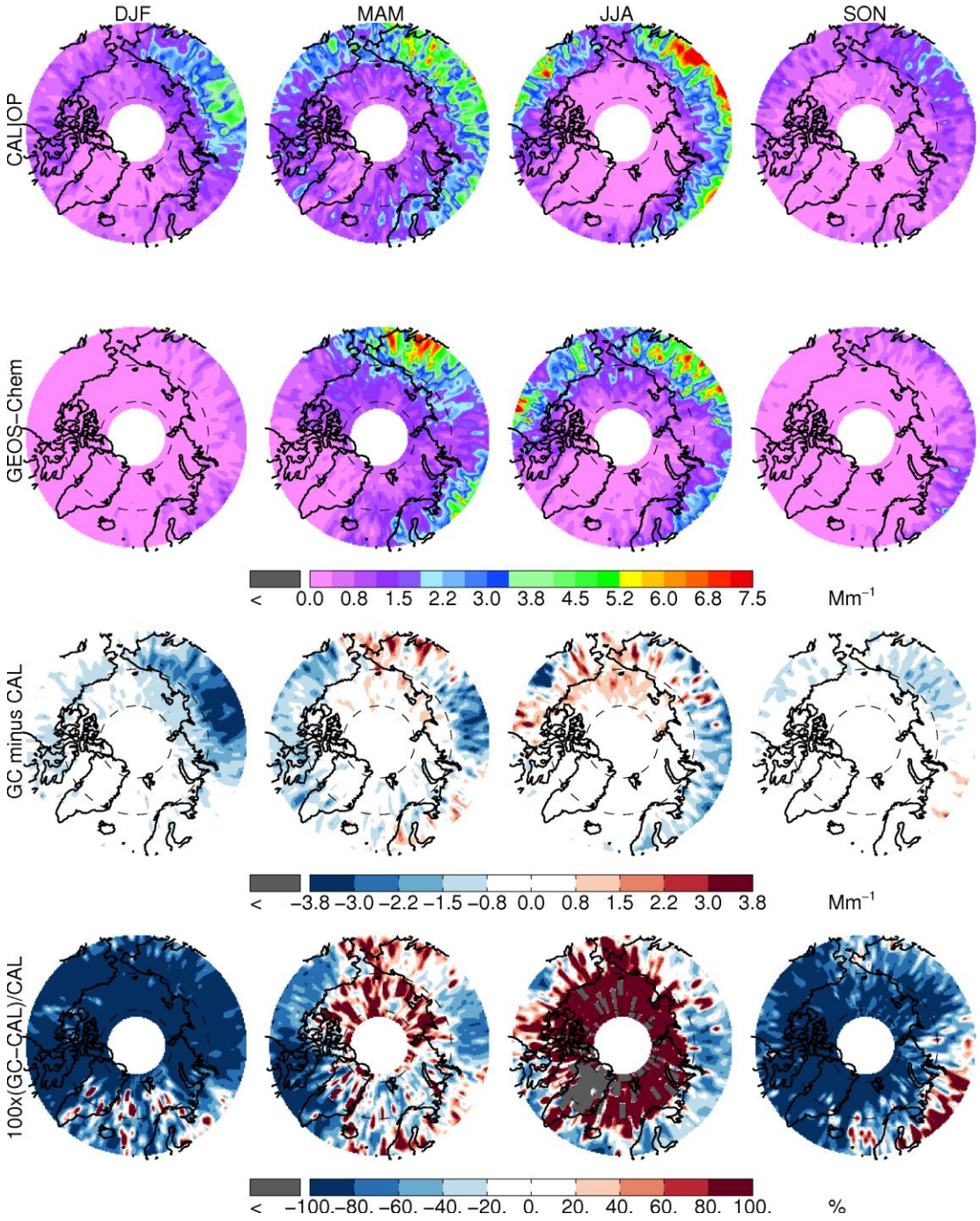

Figure 4.11: Same as Figure 4.10, but for the 2-6 km height interval.

Figure 4.11 show the same comparison as Figure 4.10 but at 2-6 km. CALIOP extinction is much lower than near the surface and maximize in the Siberian quadrant. Some degree of ventilation of the boundary layer must therefore occur over Asia in winter, possibly by mid-latitude cyclones that travel across the Asian continent. GEOS-Chem does not reproduce the enhancement in this season, as the modeled aerosols fall below CALIOP sensitivity threshold across the Arctic.

4.4.2 Spring

In spring, CALIOP extinction near the surface (0-2 km) is lower than in winter by about 10-15 Mm^{-1} (Figure 4.10, second column). GEOS-Chem captures the spatial distribution of observed extinction remarkably well, and is mostly within 5 Mm^{-1} of CALIOP retrievals. However, percent differences still show a significant underestimate in the Western Arctic (60-100%) and over Siberia (40-60%).

In the free troposphere (Figure 4.11, second column), CALIOP show a strong broad enhancement in the entire Eurasian continent, extending to Alaska. The highest extinction is seen in eastern Siberia (6-8 Mm^{-1}). The observed enhancement over Siberia and Alaska, are consistent with the long range transport of pollution aerosols from East Asia in spring that was discussed in Chapter 2. The largest differences between GEOS-Chem and CALIOP occur over central Russia (2-4 Mm^{-1}, corresponding to a 40-80% underestimate) and over the western Arctic (1-2 Mm^{-1}, corresponding to a 60-100% underestimate). The central Russian underestimate is qualitatively consistent with the negative -20% springtime bias in column AOD observed at the Siberian AERONET station of Yakutsk in March-May (Section 4.3.4).

4.4.3 Summer

In summer at 0-2 km (Figure 4.10, third column), CALIOP retrieves a large extinction over Eurasia south of 70°N (20-30 Mm^{-1}) and over Alaska and the Canadian Arctic (10-20 Mm^{-1}). Much

lower values (<10Mm^{-1}) are seen elsewhere, with very low extinction over the Arctic Ocean. The strong enhancement over Siberia and North America are likely associated boreal forest fires. A broad extinction enhancement is also seen in the Russian Arctic, possibly due to smoke transported from fires burning at lower latitudes. GEOS-Chem reproduces the spatial enhancement over the Siberian and North American boreal fires regions, but tends to be too high relative to CALIOP. The model does not reproduce the broad enhancement over the central Russian Arctic.

Poleward of 70°N at 0-2 km, CALIOP hardly detects any aerosols over the Arctic Ocean while the modeled extinction is frequently above CALIOP's threshold. The difference is small in magnitude because of the small values of extinction in the High Arctic in summer, but large in a relative sense (>100%, Figure 4.10). The model summertime overestimate over the High Arctic is consistent with in situ observations of aerosol extinction at Barrow and Alert, which show a comparable (2-4 Mm^{-1}) model overestimate in JJA (section 4.3.2). Given that the model compares well against AERONET column AOD observations across the entire Arctic, this overestimate in the lower troposphere is unlikely to be a consequence of excessive biomass burning emissions. Moreover, the biomass burning emissions used in this study (GFED3) are on the low end compared to other available inventories (Granier et al., 2011).

As shown in Figure 4.11, the observed spatial distribution of extinction in the free troposphere (2-6 km) resembles the one at 0-2 km, but exhibits relatively stronger enhancements over the active fire regions of Siberia and North America. This could reflect the higher injection heights of boreal fires and the higher elevation of Siberian and North American forests compared to mid-latitude forests in southwestern Russia. GEOS-Chem generally reproduces the observed spatial distribution at 2-6 km over continents, but tends to overestimate CALIOP extinction over the Arctic Ocean.

4.4.4 Autumn

Autumn is the season where extinction is at a minimum across the Arctic troposphere (Figure 4.10, 4.11). In both CALIOP and GEOS-Chem, the largest extinction during autumn occur over the North Atlantic Ocean as a result of sea-salt emissions. Similarly to other seasons, GEOS-Chem underestimates observed extinction over central Russia by 10 Mm^{-1} at 0-2 km and 2-3 Mm^{-1} at 2-6 km. The distribution of relative error show a pattern very similar to that found in winter.

4.4.5 Vertical profiles

Figure 4.12 shows the seasonal evolution of the CALIOP extinction profiles for the Low and High Arctic. In winter, the observed extinction maximizes below 1 km and drops rapidly with altitude to near 0 Mm^{-1} at 5 km in both the Low and High Arctic. The rapid drop reflects the strong stratification brought about by strong temperature inversions that develop over snow and ice covered surfaces (Shaw, 1995; Devasthale et al., 2011). A marked transition occurs from winter to spring: the extinction decrease at low altitudes is accompanied by an increase above 3-4 km. During summer, the Low Arctic CALIOP extinction profiles displays a broad enhancement extending to 3-4 km altitude, while the High Arctic has very low extinction throughout the vertical column. Autumn represents a transition towards a winter-like profile, and displays a similarly sharp extinction decrease with altitude.

In the Low Arctic, GEOS-Chem extinction profiles capture the observed evolution relatively well. The largest differences between GEOS-Chem and CALIOP occurs in winter, where the modeled extinction decreases much more rapidly with altitude than CALIOP extinction. In the High Arctic, it is unable to simulate the seasonal cycle correctly as discussed in sections 4.3.1-2. In particular, Figure 4.12 illustrates that the model underestimates the CALIOP extinction

over the entire column during winter and autumn, while overestimating it during summer. During spring the model does capture the observed secondary maximum in the mid-troposphere.

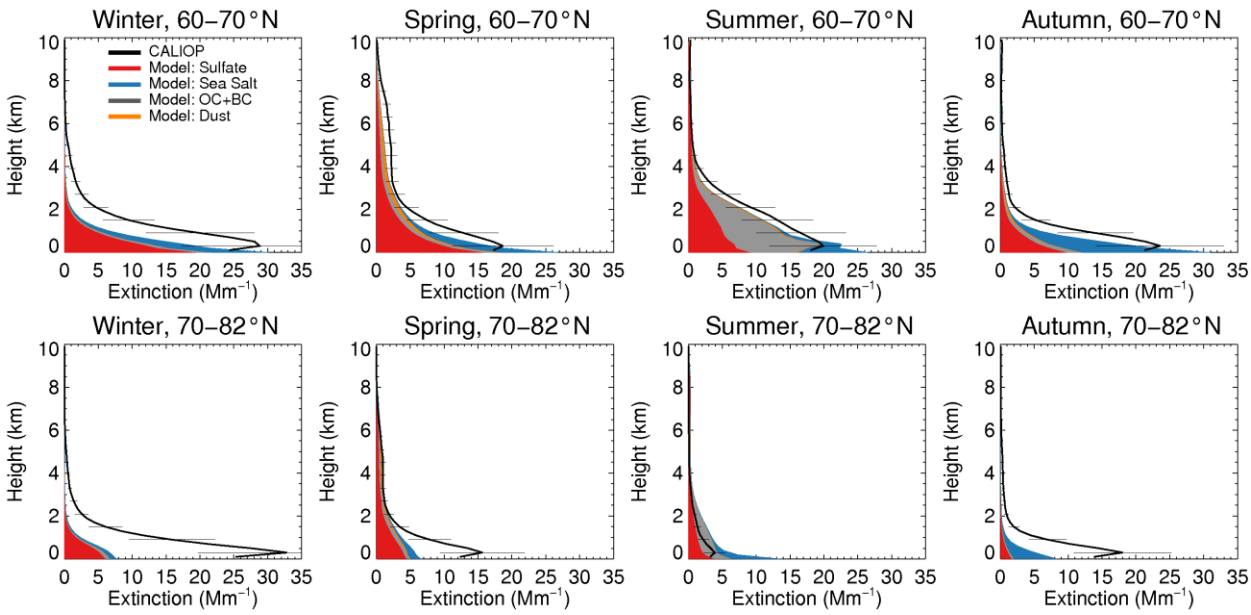

Figure 4.12: Vertical profiles of aerosol extinction as a function of season for the Low Arctic (60°-70°N, top row) and High Arctic (70°-82°N, bottom row). CALIOP observations are shown with the black line. The horizontal bars indicate the error uncertainty associated with the selection of the lidar ratio (±40%). The filled colors indicate the GEOS-Chem extinction for each aerosol species.

The model simulation suggests that sulfate dominates aerosol extinction in winter and spring over the entire Arctic. The spring maximum in the mid-troposphere is nearly equally contributed by sulfate and mineral dust. In summer, organic aerosols contribute 50-70% to the extinction up to 4 km, consistent with observations of aerosol mass concentrations during summer (Schmale et al., 2011). Autumn is the cleanest season at all altitudes: near the surface, sea-salt aerosols dominate extinction due to the large area fraction of open water and stronger winds than in summer.

4.5 Synthesis of model evaluation

We find that the model comparison with the variety of independent measurements used here reveals remarkable consistency, which we synthesize here.

4.5.1 Summertime overestimate in High Arctic aerosol concentration and extinction

In the Low Arctic, GEOS-Chem reproduces the observed summertime in situ aerosol extinction and concentration. Both nss-sulfate and sea-salt aerosol concentrations at the surface are very well simulated at Pallas and Oulanka, and so is the aerosol extinction at the surface (Figure 4.5). The model also effectively reproduces the AOD observed at AERONET stations in Low Arctic sites, and captures the observed daily variability of AOD (Figures 4.7 and 4.8). These comparisons are further supported by the very good agreement between GEOS-Chem and CALIOP as to the shape and magnitude of the aerosol extinction profile (Figure 4.12).

In the High Arctic during summer, however, the GEOS-Chem simulation indicates a systematic overestimate of aerosol extinction both at the surface and in the free troposphere. Comparisons with in situ extinction measurements show an underestimate of 2-4 Mm^{-1} at the surface at Alert, Zeppelin and Barrow. In section 4.2 we showed that the model overprediction of nss-sulfate concentrations could not explain alone the extinction overestimate. Another contributing factor could be associated with an overestimate in organic aerosol concentrations, however comparisons conducted by Heald et al. (2011) during the ARCTAS campaign showed relative good agreement with aircraft observations.

Another possibility is that the model underestimates aerosol removal processes at high latitudes during summer. Indeed, Wood (2006) showed that stratocumulus drizzle is particularly efficient at scavenging aerosols in summer. Based on a model simulation Browse et al. (2012) showed that drizzle is responsible for a factor of 10 reduction in sulfate concentrations between

60°N and 70°N. While GEOS-Chem includes large scale wet scavenging mechanisms, it is possible that the raindrop distribution imposed in the parametrization of wet scavenging does not reflect the true distribution. Since small raindrops are more efficient than large raindrops at collecting aerosol particles for equal precipitation volume (Jung et al., 2003), an overestimate of the true raindrop size distribution would result in an underestimate of wet scavenging.

4.5.2 Missing anthropogenic emissions in the central Russian Arctic

CALIOP observations indicate that the central Russian Arctic is characterized by systematically higher extinction than simulated by GEOS-Chem. Difference plots both in the lower (0-2 km) and middle (2-6 km) show that the model underestimate affects the whole column and occurs in all seasons (Figures 4.10, 4.11). Although this sector of the Arctic is poorly covered by in situ observations, the model mean normalized bias at the two Siberian AERONET stations does indicates a negative mean normalized bias both in spring (MNB=-20%) and summer (MNB=-9%). The summer negative bias is in contrast with the generally positive summertime bias observed at all other AERONET stations.

These two pieces of evidence are suggestive of an emissions underestimate in the model. Indeed, the EDGAR inventory used by GEOS-Chem does not include emissions from large flaring operations and several power plants that support energy-intensive mining operations east of the Ural Mountains (Fu et al., 2013; Huang et al., 2013). Pre-existing industrial operations have also expanded during the past decade. In particular, Fu et al. (2013) estimate that EDGAR BC emissions east of the Ural Mountains and in northern Siberia are too low by a factor of 2.

4.5.3 Wintertime model underestimate in surface aerosol extinction

GEOS-Chem does not capture the high wintertime extinction observed by CALIOP over the entire High Arctic (Figure 4.10). This is confirmed by our comparison to extinction observations at

Barrow and Alert (Figure 4.5). At those two sites, we showed that while GEOS-Chem reproduces observed nss-sulfate concentrations, it underestimates submicron sea-salt aerosol concentrations. At Barrow, observed submicron sea-salt concentrations in November-April (1 μm m^{-3}) are higher than sulfate concentrations (0.45 μm/m^3). We showed that the magnitude of the submicron mass concentration underestimate is quantitatively consistent with the extinction underestimate (section 4.3.2).

It thus appears that a missing sea-salt source can potentially provide the missing extinction to reconcile the simulation with observations. Sea-salt aerosol formation from wind-blown frost flowers has been proposed as a new source in regions covered with sea ice (Rankin et al., 2002; Rankin and Wolff, 2003) but the magnitude of this source is poorly constrained. Yang et al. (2008) showed that blowing snow events could be a significant source of sea-salt aerosols, potentially one order of magnitude larger than that from the open ocean for the same wind speed conditions. This new source is not included in the GEOS-Chem model. In section 4.6, we investigate the possibility that sea-salt from blowing snow could explain the discrepancy with the observations.

4.6 A missing sea-salt source during winter over sea ice?

The formation of sea ice during polar winter has been observed to be accompanied by the formation of frost flowers, ice crystals that grow on a slush layer enriched in salt that forms on the sea ice. These ice crystals are often very saline, up to 3 times the salinity of sea water, since the ions in brine where they form migrate into the crystals by surface tension effects (Rankin et al., 2002). During high wind conditions, fragments of these flowers can get mobilized and be transported for some distance.

Snow that falls onto sea ice progressively becomes enriched in sea-salt. The enrichment mechanism involves contact with frost flowers, sea-salt aerosol deposition, flooding of sea ice and

upward migration of brine into the snow particles (Yang et al., 2008). Under sufficiently high winds, the snow particles can be mobilized into the atmosphere and subsequently release salt particles upon sublimation in the cold, dry air. This can occur during blowing snow events, which are often observed in polar regions.

In this section, we implement the parametrization of Yang et al. (2008) that estimates the sea-salt production rate from blowing snow onto sea ice. The scheme involves the calculation of a snow sublimation flux, which leads to the release of salt aerosols. This flux depends on surface wind speed (U_t), temperature and friction velocity (u*). Snow mobilization is assumed for wind speed exceeding a threshold, which decreases with decreasing temperature. For example its values are 9.4 m/s at 0°C and 7.1 m/s at -20°C. Therefore, no sea-salt emissions are assumed for winds below $U_{t0} = 6.975$ 6.975 m/s under any conditions.

Following sublimation in the cold dry Arctic air, the snowflake release the salt particles. The sublimation flux, Q_s (units), is defined as:

$$Q_s = kA'Q_s' \, q_{bsalt}/q_{b0}$$

Where *A'* depends on the age of snow (we assume 3 days, following Yang et al., 2008) and Q_s' is a normalized column-integrated sublimation rate defined in Déry and Yau (2001). *k*=1.1574x10^{-5} converts the sublimation rate from mm day^{-1} (snow water equivalent) to kg m^{-2} s^{-1}. q_{bsalt} is the saltation layer blowing snow mixing ratio and q_{b0} is the value q_{bsalt} takes when the wind speed equals U_{t0}:

$$q_{bsalt} = 0.385(1 - U_t/U_{10})^{2.59}/u^*$$

The wind speed dependence is included in the q_{bsalt}/q_{b0} term and follows a power law:

$$\frac{q_{bsalt}}{q_{b0}} = \left(\frac{1 - U_t/U_{10}}{1 - 6.975/U_{10}}\right)^{2.59}$$

Where U_{10} is the 10 m wind speed and U_t is the threshold wind speed. The scheme assumes that one snow particle releases one salt particle. Snow particle size is imposed based on the size distributions of suspended particles in snow events (Schmidt, 1982)

$$f(d_i) = \frac{e^{\frac{-d_i}{\beta}} {d_i}^{\alpha-1}}{\beta^{\alpha}\Gamma(\alpha)}$$

With d_i is the snow particle diameter, α=2 and β=37.5 μm, and Γ is the gamma function.

The dry salt particle diameter d_{dry} that is released from sublimation of the snow particle is given by:

$$d_{dry} = d_i \left(\frac{\varsigma\, \rho_{ice}}{1000 \rho_{NaCl}}\right)$$

Where ρ_{ice}= 900 kg/m^3, ρ_{NaCl}=2160 kg/m^3 and ς is the snow salinity in psu.

We assume a constant snow salinity of 3 psu based on observations reported by Massom et al. (2001), and we only calculate the source for dry salt particle diameters less than 1 μm.

We calculate Q_S using GEOS-5 daily wind speeds and temperature. Figure 4.13 shows the seasonal evolution of this blowing snow sea-salt source. The strongest emissions occurs in winter due to the large wind speeds (Figure 4.13, middle row) and extensive sea ice cover (Figure 4.13, top row). In addition, snow mobilization is also favored in winter due to the colder temperatures, which lower the wind speed threshold necessary for the snow mobilization.

Emissions of submicron sea-salt from blowing snow poleward of 70°N are 1.7x10^7 kg day^{-1} averaged over the winters of 2006-2010. These emissions are twice as large as the accumulation-mode sea-salt emissions from open-ocean in GEOS-Chem poleward of 70°N in winter (0.9x10^7 kg day^{-1}). Their spatial distribution is also quite different as they occur over the frozen Arctic Ocean rather than over open waters in the North Atlantic (Figure 4.13). In spring, sea-salt

emissions from blowing snow decay to 0.75×10^7 kg day^{-1} (from open water: 1.8×10^7 kg day^{-1}), become negligible in summer (blowing snow: 0.03×10^7 kg day^{-1}; open water: 1.9×10^7 kg day^{-1}) and increase again in autumn (0.57×10^7 kg day^{-1} ; open water: 3.5×10^7 kg day^{-1}).

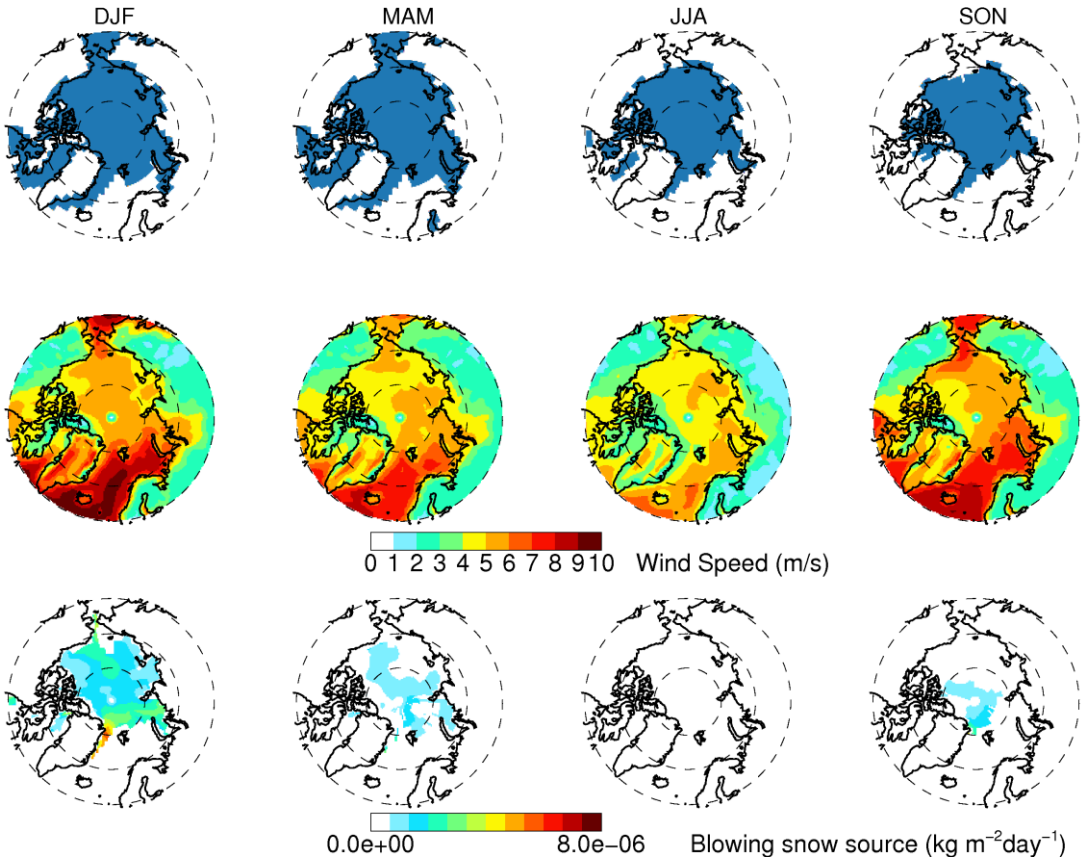

Figure 4.13: Distribution of GEOS-5 sea ice cover (top row), 10-m wind speed (middle row) and blowing snow source (bottom row) as a function of season for 2006 to 2010.

Figure 4.14 shows a monthly timeseries of the blowing snow source of sea-salt averaged over the High Arctic (70°-82°N). The strong seasonal cycle of this source is driven by wind speed and temperature. Figure 4.14 also shows the difference between CALIOP and GEOS-Chem extinction averaged over the High Arctic at 0-2 km. The missing source tracks the extinction difference very

well (r=0.90), thus the seasonality of this blowing snow sea-salt source is consistent with the discrepancy between GEOS-Chem and CALIOP. The snow blowing source and the extinction gap display do not display any strong interannual variability.

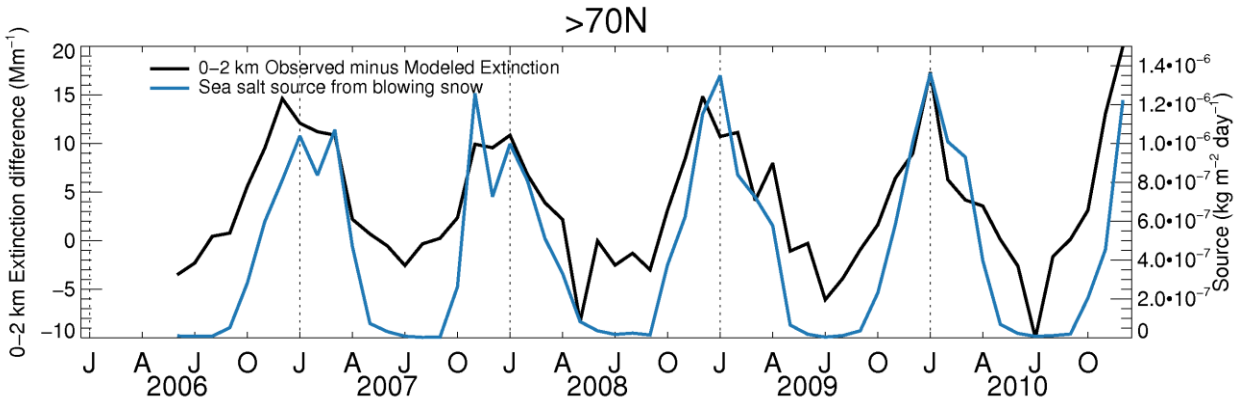

Figure 4.14: Monthly timeseries of calculated submicron blowing snow sea-salt source (blue line, right axis) averaged over the High Arctic (70-82°N). The difference between observed CALIOP and GEOS-Chem modeled extinction over the High Arctic at 0-2 km is shown in black (left axis).

The next step would be to determine whether this additional source is strong enough to reconcile model and observations, is to implement the Yang et al. (2008) scheme into GEOS-Chem. We leave these suggestions as recommendation for future work.

4.7 Conclusions

We evaluated the GEOS-Chem model simulation of aerosol mass concentrations and extinction against surface and aircraft-based in situ measurements. We compared the spatial, vertical and temporal distribution of extinction with the CALIOP distributions constructed in Chapter 3. In spring and summer we also used retrievals from ground-based sun photometers from the AERONET network to constrain the simulated column optical depth.

The model AOD is generally within ±15% of AERONET observations at 12 sites in the Arctic. Comparisons against in situ observations from the ARCTAS aircraft campaign as well as against CALIOP profiles show a good agreement in terms of the shape and magnitude of the extinction profiles in both spring and summer. We find that organic carbon aerosols control 30-60% of the extinction between 0 and 4 km.

Comparing GEOS-Chem with CALIOP observations provides valuable constraints for the simulation of the aerosol vertical distribution. The comparison was performed by applying CALIOP's backscatter detection threshold to the simulated backscatter in GEOS-Chem and by sampling GEOS-Chem along the satellite orbit. The application of the sensitivity threshold makes the comparison particularly sensitive to any large model bias that would bring the modeled extinction systematically above or below CALIOP's sensitivity threshold. It is therefore noteworthy that GEOS-Chem successfully reproduces the monthly evolution of the vertical distribution of Arctic aerosols above 2 km particularly well in both Low and High Arctic. The vertical distribution of extinction is especially well reproduced in spring and is within CALIOP's error uncertainty (±40%). Given that sulfate contributes more than half to the total extinction, and that any large bias in the sulfate simulation would be magnified by the application of the threshold, this suggests that sulfate is well simulated not only at the surface but also in the free troposphere. In the free troposphere, the largest discrepancies between GEOS-Chem and CALIOP observations are seen during the winter months. However, since the underestimate is concentrated over eastern Siberia, we think it could be due to an underestimate of anthropogenic emission in northern Russia.

GEOS-Chem captures the seasonal variation of nss-sulfate concentrations observed at Alert, Zeppelin, Barrow, Pallas and Oulanka. Mean annual extinction is within 40% at all sites except Zeppelin, where the model is a factor of 2 too high. At Barrow and Alert during summer,

we find that the model overestimates sulfate concentrations by 0.2-0.5 $\mu g/m^3$ and extinction by 1-4 Mm^{-1}. The extinction overestimate can not be solely attributed to the overestimate of sulfate concentration because other species also contribute substantially to light extinction in this season. Instead, it could be related to a too weak washout rate in the model. In fact, the raindrop distribution implicit in the washout parametrization may not be suitable for Arctic stratocumulus drizzle.

During winter at Alert and Barrow, GEOS-Chem underestimates in situ extinction by a factor 2-3. This underestimate occurs to a lesser extent in autumn and early spring. We hypothesize that this underestimate is related to the model inability to reproduce the sea-salt concentration maximum observed at Alert, Zeppelin and Barrow in November-April. The size-segregated measurements at Barrow show that the underestimate affects predominantly the sea-salt fine mode. Comparisons with CALIPSO satellite are also consistent with this picture and indicate that extinction is underestimated across the entire High Arctic by a similar factor (2-3).

We examine whether a missing sea-salt source from blowing snow, could explain this underestimate. This blowing-snow sea salt source, which is not included in GEOS-Chem, maximizes in winter. During that time it exceeds the open-ocean sea-salt emissions north of 70°N by 25%. The source strength is highly correlated (R=0.9) with the difference between observed and modeled low-level extinction averaged across the High Arctic, suggesting a causality relationship. Further work is needed to confirm the validity of this source and whether it can account for the large model underestimate of sea-salt mass concentrations and extinction over the High Arctic. Were the existence of such a blowing snow source to be confirmed, it would imply that nearly half of the near-surface wintertime High Arctic haze is natural in origin. Garrett and Zhao (2006) have shown that aerosols increase the emissivity of thin Arctic liquid-phase clouds in winter, thus warming the surface. Measurements made by Ritter et al. (2005) showed that aerosols

have also a significant direct radiative effect at thermal wavelenghts. Thus, a significant fraction of the aerosol direct thermal effect in winter could be natural. Besides blowing snow, another potential source of sea salt is frost flowers, which form only on new sea-ice and also supply salinity to the overlying snow. Changes in Arctic sea ice cover, temperature and windspeed, would likely influence the magniture of such a source of sea-salt aerosols from sea ice and could lead to a climate feedback in late autumn and winter.

Chapter 5

SUMMARY AND RECOMMENDATIONS FOR FUTURE WORK

5.1 Summary of Results

In this dissertation I used observations of vertically resolved aerosol extinction retrieved by the CALIOP instrument on-board the CALIOP satellite to examine the spatiotemporal distribution of aerosols in the Arctic and investigate their origin. I compiled a multi-year dataset of the observed spatial, vertical and seasonal distribution of Arctic aerosols, and compared it to independent ground-based and aircraft-based observations. I then used this new Arctic aerosol distribution to evaluate the GEOS-Chem chemical transport model and to shed light on some of the processes that control aerosols over the Arctic.

In Chapter 2, I documented three long-range transport events of aerosols from East Asia to the Arctic. Two of these events took place February-March 2007 and one in October 2007. The aerosol layers were observed by CALIOP at altitudes between 3 and 6 km. Their thickness was most frequently between 1 and 2 km, and their composition was dominated by sulfate (>80% of AOD), and dust (15-18%). The slanting of the aerosol layers was consistent with the local configuration of isentropic surfaces. Subsidence was observed once in the Arctic, accompanied by a radiative cooling of 1-1.5°C day^{-1}. In all cases the transport was rapid (3-5 days) and characterized by rapid ascent (up to 6 km) at the onset of the export event. When the CALIOP sensitivity threshold was applied to GEOS-Chem, the simulations compared well to the observations in terms of plume thickness, horizontal boundaries and aerosol optical depth.

I found that the meteorological situation conducive to the transport to the Arctic involved two stages: i) the passage of a mid-latitude cyclone that ventilated the planetary boundary layer and (ii) a blocking pattern that diverted the upper-air flow polewards. Following uplift in the cyclone's warm conveyor belt, a lower export efficiency was found for sulfate (~15%) than BC (~20%) or dust (30-40%).

Using the GEOS-Chem model, I systematically examined the occurrence of long-range transport events from Asia to the Arctic. From 2007 to 2009, I found that these events occurred on average six times a year, predominantly in spring. During springtime export events, the elevated sulfate component was often accompanied by an enhancement of the dust component.

In Chapter 3, I compiled six years of CALIOP retrievals from the CALIPSO satellite. I developed an empirical methodology to account for the lower sensitivity of CALIOP daytime retrievals compared to nighttime retrievals, which allowed me to reconstruct the full seasonal cycle of Arctic aerosols. This multi-year dataset shows an annual maximum of extinction in winter to early spring across the whole Arctic at 0-2 km. In addition, over the Low Arctic (60-70°N) there is a secondary maximum during summer associated with biomass burning. During summer, retrieved extinction reaches an annual minimum in the High Arctic at 0-2 km. Thus, in summer, the High and Low Arctic appear decoupled, due to the withdrawal of the Polar Front and efficient wet removal between 55° and 70°N, which results in a strong gradient of extinction observed between 60°N and 75°N.

At low levels, two strong extinction enhancements are observed below 2 km in winter. The first is associated with sea salt production in the North Atlantic caused by the seasonal wind speed maximum. The second (25-35 Mm^{-1}) is seen over central Russia and is related to the southerly circulation on the western side of the Siberian anticyclone. This appear to be an important entry

way to the Arctic of pollution aerosols at low levels. As a consequence, the European Sector of the High Arctic (0-110°E) exhibits the largest extinction in December-March (20-22 Mm^{-1}), while the North American (140°W-60°W) and Atlantic (60°W-0) sectors exhibiting the lowest extinction (8-15 Mm^{-1}).

The seasonality of aerosol extinction above 2 km shows an annual maximum in March-April, associated with increased cyclonic activity and blocking frequency at mid-latitudes. The Asian sector (110°E-140°W) of the Arctic exhibits a clear extinction maximum at 3-6 km in spring (2-3 Mm^{-1}). Both the height and magnitude of this peak are greater than in any other sector, where extinction peaks below 5 km (1-2 Mm^{-1}). There is a progressive shift of the CALIOP extinction maximum with altitude, from January at 0–2 km, to March at 2–5 km, to April at 5–8 km.

The interannual variability of aerosol extinction is relatively small. The largest departures from the multi-year mean are associated with anomalously strong springtime biomass burning, as in the case of April 2008 (agricultural burning in Russia and Kazakhstan) and July 2010 (forest fires in Russia). The Arctic Oscillation (AO) also influences the interannual variability of extinction throughout the troposphere. Two 6-month periods of anomalously low (high) extinction were linked to strongly negative (positive) AO polarities.

Volcanoes occasionally affect extinction in the upper troposphere. Extinction enhancements between 6-10 km were observed in September-October 2008 and 2009, following stratospheric subsidence of sulfate aerosols 2-4 months after the eruptions of Kasatochi (August 7, 2008) and Sarychev (June 2009).

Comparisons of GEOS-Chem with observations of surface aerosol mass concentrations indicate a successful simulation of the seasonality of sulfate at the surface. Sulfate concentrations appear to be systematically overestimated by 1-4 Mm^{-1} (factor 2-5) in the summer at the Alert,

Barrow and Zeppelin. Sea-salt concentrations are well simulated at Pallas and Oulanka. At Alert, Barrow and Zeppelin, however, the model does not reproduce the sea salt maximum in November-March and underestimates the total sea salt mass concentration by 0.5-1.5 $\mu m/m^3$. At these same sites and during the same period the model underestimates surface extinction by 5-10 Mm^{-1} (factor 2-3).

Comparison with measurements of column optical depth from sun photometers and with the observed vertical distribution of extinction from CALIOP demonstrates that GEOS-Chem is able to reproduce the magnitude, variability and vertical distribution of aerosol extinction in spring and summer. The column optical depth comparison indicates a negative model bias (10-20%) at the Siberian station of Yakutsk in both spring and summer. Since CALIOP observations further indicate that Yakutsk falls within and area (90-150°E) where the model underestimates extinction both near the surface and aloft in all seasons, emissions in this area are likely underestimated in the GEOS-Chem.

Overall, the consistency seen across the model comparisons with various independent observations suggests the existence of a missing source of sea salt from processes related to either the seasonal formation of sea ice (frost flowers) or to the deposition of snow on sea-ice, both of which involve the sublimation of saline ice crystals mobilized by wind. A preliminary analysis shows that the production rate of a blowing snow source is comparable to that of sea salt from open waters for latitudes north of 70°N in winter, and that it possesses the right seasonality to improve the simulation of light extinction and sea salt aerosol concentrations in the Arctic. In summer, the large extinction overestimate, in a relative sense, seen in the High Arctic is indicative of too weak removal processes simulated by GEOS-Chem at a time when scavenging by Arctic stratocumulus drizzle is very efficient. The model also underestimates extinction over central and

eastern Russia through the troposphere in all seasons, which suggests rapidly growing emission in the last 10 years in northern Russia.

5.2 Recommendations for future work

Comparisons against observations over the Arctic showed that the GEOS-Chem model reproduces the vertical distribution of aerosol extinction and the seasonality of sulfate concentrations at the surface. This would lend confidence to using the GEOS-Chem model to examine the Arctic sulfur budget analysis as a function of altitude and season. Such an analysis could allow to determine what fraction of $SO_4^=$ directly enters the Arctic in aerosol form and what fraction is produced within the Arctic by oxidation of SO_2. One interesting issue to examine is whether the altitude and latitude shifts of the observed extinction maximum, from March at 2-5 km to April at 5-8 km in the High Arctic, and from March-April in the High Arctic to May in the Low Arctic above 2 km are caused by in situ gas phase oxidation of SO_2 following polar sunrise, which has been invoked to explain the reduction of particle size observed in the upper troposphere from March to June (Treffeisen et al., 2006).

A source attribution analysis for an extended period of time as a function of altitude and season would also be of interest. This could be done by running sensitivity simulations where anthropogenic emissions of aerosols and their precursors are turned off within a specific source region (e.g. N. America, Europe, or Asia). It would be possible to determine what fraction of the Arctic aerosol burden comes from East Asia, at what altitudes, and what fraction of it is deposited as opposed to leaving the Arctic. Such an analysis could be conducted for different types of aerosols: sulfate, BC, organics, sea salt. Since the aerosol simulation is nearly linear in nature, by subtracting the sensitivity simulation from the standard simulation it will be possible to determine the contribution of each region. One could also contrast the export efficiencies for each of these

aerosols depending on their origin. For example, aerosols that enter the Arctic via low-level transport from Eurasia are likely to have a higher export efficiency (i.e. less removal) relative to aerosols that are lifted to the middle troposphere via mid-latitude cyclones.

Finally, it is recommended that the blowing snow source of sea-salt be included in GEOS-Chem and a sensitivity simulation be performed. Sea salt concentrations and total light extinction from the new simulation could be compared in situ measurements at the Arctic sites on daily to weekly timescales, as well as to CALIOP observations of aerosol extinction near the surface. This would determine whether the proposed source is able to produce large enough concentrations and the correct temporal variation, thus reconciling the simulations with observations across the Arctic. This potential source would have implications for the simulation of bromine explosions in polar spring and the simulation of ozone depletion events at polar sunrise. By acting as cloud condensation nuclei, sea salt aerosol from blowing snow would likely contribute to wintertime surface warming by increasing the longwave emissivity of optically thin Arctic clouds (Garrett and Zhao, 2006). It would also be interesting to look at multi-decadal trends of sea salt concentrations where available, to investigate the hypothesis of a changing sea salt source from sea ice, possibly associated with a shrinking sea ice cover and changing wind speeds, as this could represent a positive climate feedback in late autumn and winter.

Bibliography

Aaltonen, V., Lihavainen, H., Kerminen, V.-M., Komppula, M., Hatakka, J., Eneroth, K., Kulmala, M., and Viisanen, Y.: Measurements of optical properties of atmospheric aerosols in Northern Finland, Atmos. Chem. Phys., 6, 1155-1164, doi:10.5194/acp-6-1155-2006, 2006.

Albrecht, B. A.: Aerosols, cloud microphysics, and fractional cloudiness, Science, 245, 1227-1230, 1989.

Alexander, B., Savarino, J., Lee, C. C. W., Park, R. J., Jacob, D. J., Thiemens, M. H., Li, Q. B. and Yantosca, R. M.: Sulfate formation in sea-salt aerosols: Constraints from oxygen isotopes, J. Geophys. Res., 110, D10307, doi:10.1029/2004JD005659, 2005.

Anderson, B. E., Cofer, W. R., Bagwell, D. R., Barrick, J. W., Hudgins, C. H., and Brunke, K. E.: Airborne observations of aircraft aerosol emissions I: Total nonvolatile particle emission indices, Geophys. Res. Lett., 25(10), 1689–1692, doi:10.1029/98GL00063, 1998.

Anderson, T. L. and Ogren, J. A.: Determining aerosol radiative properties using the TSI 3563 integrating nephelometer, Aerosol Sci. Technol., 29, 57–69, doi:10.1080/02786829808965551, 1998.

Anderson, T. L., Charlson, R. J., Winker, D. M., Ogren, J. A., Holmén, K.: Mesoscale Variations of Tropospheric Aerosols, J. Atmos. Sci., 60, 119–136, doi: 10.1175/1520-0469(2003)060<0119:MVOTA>2.0.CO;2, 2003.

Barrie, L. A., Hoff, R. M., and Daggupaty, S. M.: The influence of mid-latitudinal pollution sources on haze in the Canadian Arctic, Atmos. Environ., 15, 1407-1419, doi:10.1016/0004-6981(81)90347-4, 1981.

Barrie, L. A.: Arctic air pollution: An overview of current knowledge, Atmos. Environ., 20, 643-663, 1986.

Barrie, L. A., Olson, M. P., and Oikawa, K. K.: The flux of anthropogenic sulphur into the Arctic from mid-latitudes in 1979/80, Atmos. Environ., 23, 2505–2512, doi:10.1016/0004-6981(89)90262-X, 1989.

Barriopedro, D., Garcia-Herrera, R., Lupo, A. and Hernandez, E.: A climatology of Northern Hemisphere Blocking, J. Climate, 19, 1042-1063, 2006.

Beine, H. J., Engardt, M., Jaffe, D. A., Hov, Ø., Holḿen, K., and Stordal., F.: Measurements of NOx and aerosol particles at the Ny-Ålesund Zeppelin mountain station on Svalbard: Influence on regional and local pollution sources, Atmos. Environ., 30, 1067–1079, 1996.

Bey, I., Jacob, D. J., Yantosca, R. M., Logan, J. A., Field, B. D., Fiore, A. M., Li, Q., Liu, H. Y., Mickley, L. J. and Schultz, M. G.: Global modeling of tropospheric chemistry with assimilated meteorology: Model description and evaluation, J. Geophys. Res., 106(D19), 23073-23095, 2001.

Bian, H., Colarco, P. R., Chin, M., Chen, G., Rodriguez, J. M., Liang, Q., Blake, D., Chu, D. A., da Silva, A., Darmenov, A. S., Diskin, G., Fuelberg, H. E., Huey, G., Kondo, Y., Nielsen, J. E., Pan, X., and Wisthaler, A.: Source attributions of pollution to the Western Arctic during the NASA ARCTAS field campaign, Atmos. Chem. Phys., 13, 4707-4721, doi:10.5194/acp-13-4707-2013, 2013.

Bourdages, L., Duck, T. J., Lesins, G., Drummond, J. R., and Eloranta, E. W.: Physical properties of High Arctic tropospheric particles during winter, Atmos. Chem. Phys., 9, 6881–6897, doi:10.5194/acp-9-6881-2009, 2009.

Bourgeois, Q., and Bey, I.: Pollution transport efficiency toward the Arctic: Sensitivity to aerosol scavenging and source regions, J. Geophys. Res., 116, D08213, doi:10.1029/2010JD015096, 2011.

Brock, C. A., Cozic, J., Bahreini, R., Froyd, K. D., Middlebrook, A. M., McComiskey, A., Brioude, J., Cooper, O. R., Stohl, A., Aikin, K. C., de Gouw, J. A., Fahey, D. W., Ferrare, R. A., Gao, R.-S., Gore, W., Holloway, J. S., Hübler, G., Jefferson, A., Lack, D. A., Lance, S., Moore, R. H., Murphy, D. M., Nenes, A., Novelli, P. C., Nowak, J. B., Ogren, J. A., Peischl, J., Pierce, R. B., Pilewskie, P., Quinn, P. K., Ryerson, T. B., Schmidt, K. S., Schwarz, J. P., Sodemann, H., Spackman, J. R., Stark, H., Thomson, D. S., Thornberry, T., Veres, P., Watts, L. A., Warneke, C., and Wollny, A. G.: Characteristics, sources, and transport of aerosols measured in spring 2008 during the aerosol, radiation, and cloud processes affecting Arctic Climate (ARCPAC) Project, Atmos. Chem. Phys., 11, 2423-2453, doi:10.5194/acp-11-2423-2011, 2011.

Browell, E. V., Hair, J. W., Butler, C. F., Grant, W. B., DeYoung, R. J., Fenn, M. A., Brackett, V. G., Clayton, M. B., Brasseur, L. A., Harper, D. B., Ridley, B. A., Klonecki, A. A., Hess, P. G., Emmons, L. K., Tie, X., Atlas, E. L., Cantrell, C. A., Wimmers, A. J., Blake, D. R., Coffey, M. T., Hannigan, J. W., Dibb, J. E., Talbot, R. W., Flocke, F., Weinheimer, A. J., Fried, A., Wert, B., Snow, J. A., and Lefer, B. L.: Ozone, aerosol, potential vorticity, and trace gas trends observed at high-latitudes over North America from February to May 2000, J. Geophys. Res., 108(D4), 8369, doi:10.1029/2001JD001390, 2003.

Browse, J., Carslaw, K. S., Arnold, S. R., Pringle, K., and Boucher, O.: The scavenging processes controlling the seasonal cycle in Arctic sulphate and black carbon aerosol, Atmos. Chem. Phys., 12, 6775-6798, doi:10.5194/acp-12-6775-2012, 2012.

Burton, S. P., Ferrare, R. A., Hostetler, C. A., Hair, J. W., Rogers, R. R., Obland, M. D., Butler, C. F., Cook, A. L., Harper, D. B., and Froyd, K. D.: Aerosol classification using airborne High Spectral Resolution Lidar measurements – methodology and examples, Atmos. Meas. Tech., 5, 73-98, doi:10.5194/amt-5-73-2012, 2012.

Carlson, T. N.: Speculations on the movement of polluted air to the Arctic, Atmos. Environ., 15(8), 1473–1477, doi: 10.1016/0004-6981(81)90354-1, 1981.

Chen, S.-J., Kuo, Y.-H., Zhang, P.-Z., and Bai, Q.-F.: Synoptic Climatology of Cyclogenesis over East Asia, 1958–1987, Am. Meteor. Soc., 119(6), 1407–1418, doi: 10.1175/1520-0493(1991)119<1407:SCOCOE>2.0.CO;2, 1991.

Curry, J.: On the formation of continental polar air, Amer. Meteor. Soc., 40, 2278-2292, 1983.

Clarke, A. D., and Noone, K. J.: Soot in the Arctic snowpack: a cause for perturbation in radiative transfer, Atmos. Environ., 19, 2045-2053, 1985.

Clarke, A. D., Shinozuka, Y., Kapustin, V. N., Howell, S., Huebert, B., Doherty, S., Anderson, T., Covert, D., Anderson, J., Hua, X., Moore II, K. G., McNaughton, C., Carmichael, G., and Weber, R.: Size distributions and mixtures of dust and black carbon aerosol in Asian outflow: Physiochemistry and optical properties, J. Geophys. Res., 109, D15S09, doi:10.1029/2003JD004378, 2004.

Cohen, J., Foster, J., Barlow, M., Saito, K., and Jones, J.: Winter 2009–2010: A case study of an extreme Arctic Oscillation event, Geophys. Res. Lett., 37, L17707, doi:10.1029/2010GL044256, 2010.

Delene, D. J. and Ogren, J. A.: Variability of Aerosol Optical Properties at Four North American Surface Monitoring Sites, J. Atmos. Sci., 59(6), 1135-1150, doi:10.1175/1520-0469(2002)059<1135:VOAOPA>2.0.CO;2, 2002.

Devasthale, A., Tjernstrom, M., and Omar, A. H.: The vertical distribution of thin features over the Arctic analysed from CALIPSO observations, Tellus, 63B, 86-95, doi: 10.1111/j.1600-0889.2010.00517.x, 2011.

Déry, S. J. and Yau, M. K.: Simulation of blowing snow in the Canadian Arctic using a double-moment model, Boundary Layer Meteorol., 99, 297-316, 2001.

de Villiers, R. A., Ancellet, G., Pelon, J., Quennehen, B., Schwarzenboeck, A., Gayet, J. F., and Law, K. S.: Airborne measurements of aerosol optical properties related to early spring transport of mid-latitude sources into the Arctic, Atmos. Chem. Phys., 10, 5011-5030, doi:10.5194/acp-10-5011-2010, 2010.

Di Pierro, M., Jaeglé, L., and Anderson, T. L.: Satellite observations of aerosol transport from East Asia to the Arctic: Three case studies, Atmos. Chem. Phys., 11, 2225–2243, doi:10.5194/acp-11-2225- 2011, 2011.

Di Pierro, M., Jaeglé, L., Eloranta, E. W., and Sharma, S.: Spatial and seasonal distribution of Arctic aerosols observed by the CALIOP satellite instrument (2006–2012), Atmos. Chem. Phys., 13, 7075-7095, doi:10.5194/acp-13-7075-2013, 2013.

Doherty, S. J., Warren, S. G., Grenfell, T. C., Clarke, A. D., and Brandt, R. E.: Light-absorbing impurities in Arctic snow, Atmos. Chem. Phys., 10, 11647-11680, doi:10.5194/acp-10-11647-2010, 2010.

Draxler, R. R. and Hess, G. D.: Description of the HYSPLIT_4 Modeling System, NOAA Technical Memorandum ERL ARL-224, revised January 2004.

Duncan, B. N., and Bey, I.: A modeling study of the export pathways of pollution from Europe: Seasonal and interannual variations (1987–1997), J. Geophys. Res., 109, D08301, doi:10.1029/2003JD004079, 2004.

Eckhardt, S., Stohl, A., Beirle, S., Spichtinger, N., James, P., Forster, C., Junker, C., Wagner, T., Platt, U., and Jennings, S. G.: The North Atlantic Oscillation controls air pollution transport to the Arctic, Atmos. Chem. Phys., 3, 1769-1778, doi:10.5194/acp-3-1769-2003, 2003.

Eckhardt, S., Breivik, K., Man\o, S., and Stohl, A.: Record high peaks in PCB concentrations in the Arctic atmosphere due to long-range transport of biomass burning emissions, Atmos. Chem. Phys., 7, 4527-4536, doi:10.5194/acp-7-4527-2007, 2007.

Eloranta, E. W. , Razenkov, I. A., and Garcia, J. P.: Arctic Observations with the University of Wisconsin High Spectral Resolution Lidar, in Reviewed and Revised Papers Presented at the 23rd International Laser Radar Conference, edited by: Nagasawa, C. and Sugimoto, N., pp. 399–402, 2006.

Engvall, A.-C., Krejci, R., Ström, J., Minikin, A., Treffeisen, R., Stohl, A., and Herber, A.: In-situ airborne observations of the microphysical properties of the Arctic tropospheric aerosol during late spring and summer, Tellus, 60B, 392-404, doi:10.1111/j.1600-0889.2008.00348.x, 2008.

Fairlie, T. D., Jacob, D. J. and Park, R. J.: The impact of transpacific transport of mineral dust in the United States, Atmos. Environ., 41, 1251-1266, 2007.

Fisher, J. A., Jacob, D. J., Purdy, M. T., Kopacz, M., Le Sager, P., Carouge, C., Holmes, C. D., Yantosca, R. M., Batchelor, R. L., Strong, K., Diskin, G. S., Fuelberg, H. E., Holloway, J. S., Hyer, E. J., McMillan, W. W., Warner, J., Streets, D. G., Zhang, Q., Wang, Y., and Wu, S.: Source attribution and interannual variability of Arctic pollution in spring constrained by aircraft (ARCTAS, ARCPAC) and satellite (AIRS) observations of carbon monoxide, Atmos. Chem. Phys., 10, 977-996, doi:10.5194/acp-10-977-2010, 2010.

Fisher, J. A., Jacob, D. J., Wang, Q., Bahreini, R., Carouge, C. C., Cubison, M. J., Dibb, J. E., Diehl, T., Jimenez, J. L., Leibensperger, E. M., Lu, Z. F., Meinders, M. B. J., Pye, H. O. T., Quinn, P. K., Sharma, S., Streets, D. G., van Donkelaar, A., and Yantosca, R. M.: Sources, distribution, and acidity of sulfate-ammonium aerosol in the Arctic in winter-spring. Atmospheric Environment, 45(39), 7301-7318, doi: 10.1016/j.atmosenv.2011.08.030, 2011.

Flanner, M. G., Zender, C. S., Randerson, J. T., and Rasch, P. J.: Present-day climate forcing and response from black carbon in snow, J. Geophys. Res.-Atmos., 112, D11202, doi:10.1029/2006JD008003, 2007.

Ford, B. J. and Heald C. L.: An A-Train and model perspective on the vertical distribution of aerosols and CO in the Northern Hemisphere, J. Geophys. Res., doi:10.1029/2011JD016977, 2012.

Fountoukis, C. and Nenes, A.: ISORROPIA II: a computationally efficient thermodynamic equilibrium model for K+–Ca2+–Mg2+–NH4+–Na+–SO42−–NO3−–Cl−–H2O aerosols, Atmos. Chem. Phys., 7, 4639-4659, doi:10.5194/acp-7-4639-2007, 2007.

Fu, J. S., Huang, K., Dong, X., Hodson, E., Storey, J., Prikhodko, V., and Cheng, M.: Assessment of black carbon in Russia using GEOS-Chem, presented at the 6th International GEOS-Chem Meeting (IGC6), Harvard University May 6-9, 2013.

Fuelberg, H. E., Harrigan, D. L., and Sessions, W.: A meteorological overview of the ARCTAS 2008 mission, Atmos. Chem. Phys., 10, 817-842, doi:10.5194/acp-10-817-2010, 2010.

Garrett, T. J., and Zhao, C.: Increased Arctic cloud longwave emissivity associated with pollution from mid-latitudes, Nature, 440, 787-789, doi:10.1038/nature04636, 2006.

Garrett, T. J., and Verzella L. L.: Looking back: an evolving history of Arctic aerosols, B. Am. Meteorol. Soc., 89, 299-302, doi:10.1175/BAMS-89-3-299, 2008.

Garrett, T. J., Brattström, S., Sharma, S., Worthy, D. E. J., and Novelli, P.: The role of scavenging in the seasonal transport of black carbon and sulfate to the Arctic, Geophys. Res. Lett., 38, L16805, doi:10.1029/2011GL048221, 2011.

Gassó, S., Hegg, D. A., Covert, D. S., Collins, D., Noone, K. J., Öström, E., Schmid, B., Russell, P. B., Livingston, J. M., Durkee, P. A. and Jonsson, H.: Influence of humidity on the aerosol scattering coefficient and its effect on the upwelling radiance during ACE-2. Tellus, 52B, 546-567, doi: 10.1034/j.1600-0889.2000.00055.x, 2000.

Gayet, J.-F., Mioche, G., Dörnbrack, A., Ehrlich, A., Lampert, A., and Wendisch, M.: Microphysical and optical properties of Arctic mixed-phase clouds. The 9 April 2007 case study., Atmos. Chem. Phys., 9, 6581-6595, doi:10.5194/acp-9-6581-2009, 2009.

Giglio, L., Csiszar, I., and Justice, C. O.: Global distribution and seasonality of active fires as observed with the Terra and Aqua Moderate Resolution Imaging Spectroradiometer (MODIS) sensors, J. Geophys. Res., 111, G02016, doi:10.1029/2005JG000142, 2006.

Gong, S. L., Zhao, T. L., Sharma, S., Toom-Sauntry, D., Lavoué, D., Zhang, X. B., Leaitch, W. R. ,and Barrie, L. A.: Identification of trends and interannual variability of sulfate and black carbon in the Canadian High Arctic: 1981–2007, J. Geophys. Res., 115, D07305, doi:10.1029/2009JD012943, 2010.

Granier, C., et al.: Evolution of anthropogenic and biomass burning emissions of air pollutants at global and regional scales during the 1980-2010 period, Climatic Change, 109, 163-190, doi:10.1007/s10584-011-0154-1, 2011.

Grenier, P., Blanchet, J., and Muñoz-Alpizar, R.: Study of polar thin ice clouds and aerosols seen by CloudSat and CALIPSO during midwinter 2007, J. Geophys. Res., 114, D09201, doi:10.1029/2008JD010927, 2009.

Harte, J.: Ecological Implications of Arctic air pollution, in: Arctic air pollution, Adie, R. J., Armstrong, T. E., Drewry, D. J., Greene, S. W., Stonehouse, B., Wadhams, P., Walton, D. W., and Whitaker, I. (eds), Cambridge University Press, Cambridge, UK, ISBN 0521 330009, 1986.

Haywood, J.M. and Ramaswamy, V.: Global sensitivity studies of the direct radiative forcing due to anthropogenic sulfate and black carbon aerosols, J. Geophys. Res., 103, 6043-6058, doi: 10.1029/97JD03426, 1998.

Hegg, D. A., Warren, S. G., Grenfell, T. C., Doherty, S. J., and Clarke, A. D.: Sources of light-absorbing aerosol in arctic snow and their seasonal variation, Atmos. Chem. Phys., 10, 10923-10938, doi:10.5194/acp-10-10923-2010, 2010.

Heintzenberg, J., Birmili, W., Otto, R., Andreae, M. O., Mayer, J.-C., Chi, X., and Panov, A.: Aerosol particle number size distributions and particulate light absorption at the ZOTTO tall tower (Siberia), 2006–2009, Atmos. Chem. Phys., 11, 8703-8719, doi:10.5194/acp-11-8703-2011, 2011.

Henze, D. K., and J. H. Seinfeld, Global secondary organic aerosol from isoprene oxidation, Geophys. Res. Lett., 33, L09812, doi: 10.1029/2006GL025976, 2006.

Henze, D. K., Seinfeld, J. H., Ng, N. L., Kroll, J. H., Fu, T.-M., Jacob, D. J., and Heald, C. L.: Global modeling of secondary organic aerosol formation from aromatic hydrocarbons: high- vs. low-yield pathways, Atmos. Chem. Phys., 8, 2405-2420, doi:10.5194/acp-8-2405-2008, 2008.

Hirdman, D., Burkhart, J. F., Sodemann, H., Eckhardt, S., Jefferson, A., Quinn, P. K., Sharma, S., Ström, J., and Stohl, A.: Long-term trends of black carbon and sulphate aerosol in the Arctic: changes in atmospheric transport and source region emissions, Atmos. Chem. Phys., 10, 9351-9368, doi:10.5194/acp-10-9351-2010, 2010.

Holben, B. N., Eck, T. F., Slutsker, I., Tanré, D., Buis, J. P., Setzer, A., Vermote, E., Reagan, J. A., Kaufman, Y. J., Nakajima, T., Lavenu, F., Jankowiak, I., and Smirnov, A.: AERONET-A federated instrument network and data archive for aerosol characterization, Remote Sens. Environ., 66, 1–16, doi:10.1016/S0034-4257(98)00031-5, 1998.

Hoff, R. M.*:* Vertical Structure of Arctic Haze Observed by Lidar, J. Appl. Meteorol., 27, 125–139, doi: 10.1175/1520-0450(1988)027<0125:VSOAHO>2.0.CO;2, 1988.

Huang, K., Fu, J. S., and Dong, X.: Missing black carbon emissions in Russia: new BC emissions for GEOS-Chem, presented at the 6th International GEOS-Chem Meeting (IGC6), Harvard University May 6-9, 2013.

Ichoku, C., Giglio, L., Wooster, M. J., and Remner, L.: Global characterization of biomass-burning patterns using satellite measurements of fire radiative energy, Remote Sens. Environ., 112, 2950-2962, 2008.

Intrieri, J. M., and Shupe, M. D.: Characteristics and radiative effects of diamond dust over the Western Arctic Ocean region, J. Climate, 17, 2953-2960, doi: 10.1175/1520-0442(2004)017<2953:CAREOD>2.0.CO;2, 2004.

Ishii, S., Shibata, T., Sakai, T., Kido, M., Hara, K., Osada, K., Iwasaka, Y., Nagai, T., Fujimoto, T., Itabe, T., Mizutani, K., and Uchino, O.: The source, size and chemical composition of the winter Arctic tropospheric aerosol layer observed by lidar at Eureka, Canada, J. Meteorol. Soc. Jpn., 79(1), 61–78, doi: 10.2151/jmsj.79.61, 2001.

Iversen, T.: On the atmospheric transport of pollution to the Arctic, Geophys. Res. Lett, 11, 457-460, doi: 10.1029/GL011i005p00457, 1984.

Iversen, T., and Joranger, E.: Arctic air pollution and large-scale atmospheric flows, Atmos. Environ., 19(12), 2099–2108, doi: 10.1016/0004-6981(85)90117-9, 1985.

Iziomon, M. G., Lohmann, U., and Quinn, P. K.: Summertime pollution events in the Arctic and potential implications, J. Geophys. Res., 111, D12206, doi:10.1029/2005JD006223, 2006.

Jacob, D. J., Crawford, J. H., Maring, H., Clarke, A. D., Dibb, J. E., Emmons, L. K., Ferrare, R. A., Hostetler, C. A., Russell, P. B., Singh, H. B., Thompson, A. M., Shaw, G. E., McCauley, E., Pederson, J. R., and Fisher, J. A.: The Arctic Research of the Composition of the Troposphere from Aircraft and Satellites (ARCTAS) mission: design, execution, and first results, Atmos. Chem. Phys., 10, 5191-5212, doi:10.5194/acp-10-5191-2010, 2010.

Jaeglé, L., Quinn, P. K., Bates, T. S., Alexander, B., and Lin, J.-T.: Global distribution of sea salt aerosols: new constraints from in situ and remote sensing observations, Atmos. Chem. Phys., 11, 3137-3157, doi:10.5194/acp-11-3137-2011, 2011.

Jung, C. H., Kim, Y. P., Lee, K. W.: A moment model for simulating raindrop scavenging of aerosols, J. Aerosol Sci., 34, 9, 1217-1233, 2003.

Kalnay, E. and Coauthors: The NCEP/NCAR Reanalysis 40-year Project, Bull. Amer. Meteor. Soc., 77, 437-471, 1996.

Klein, W. H.: The frequency of cyclones and anticyclones in relation to the mean circulation, J. of Meteo., 15(1), 98–102, doi: 10.1175/1520-0469(1958)015<0098:TFOCAA>2.0.CO;2, 1958.

Klonecki, A., Hess, P., Emmons, L., Smith, L., Orlando, J., and Blake, D.: Seasonal changes in the transport of pollutants into the Arctic troposphere-model study, J. Geophys. Res., 108(D4), 8367, doi:10.1029/2002JD002199, 2003.

Koch, D. and Hansen, J.: Distant origins of Arctic black carbon: A Goddard Institute for Space Studies ModelE experiment, J. Geophys. Res., 110, D04204, doi:10.1029/2004JD005296, 2005.

Koch, D., Menon, S., Del Genio, A., Ruedy, R., Alienov, I., and Schmidt, G. A.: Distinguishing aerosol impacts on climate over the past century, J. Climate, 22, 2659-2677, doi:10.1175/2008JCLI2573.1, 2009.

Koffi, B., Schulz, M., Bréon, F-M, Griesfeller, J., Winker, D. M., Balkanski, Y., Bauer, S., Berntsen, T., Chin, M., Collins, W. D., Dentener, F., Diehl, T., Easter, R. C., Ghan, S. J., Ginoux, P. A., Gong, S., Horowitz, L. W., Iversen, T., Kirkevag, A., Koch, D., M., Krol, M., Myhre, G., Stier, P., and Takemura, T.: Application of the CALIOP layer product to evaluate the vertical distribution of aerosols estimated by global models: AeroCom phase I results, J. Geophys. Res., 117, D10201, doi:10.1029/2011JD016858, 2012.

Kravitz, B., Robock, A., Bourassa, A., Deshler, T., Wu, D., Mattis, I., Finger, F., Hoffmann, A., Ritter, C., Bitar, L., Duck, T. J., and Barnes, J. E.: Simulation and observations of stratospheric aerosols from the 2009 Sarychev volcanic eruption, J. Geophys. Res., 116, D18211, doi:10.1029/2010JD015501, 2011.

Law, K. S., and Stohl, A.: Arctic air pollution: Origins and impacts, Science, 315(5818), 1537–1540, doi:10.1126/science.1137695, 2007.

Lejenas, H. and Økland, H.: Characteristics of northern hemisphere blocking as determined from a long time series of observational data, Tellus, 35A, 350–362, 1983.

Liao, H, Seinfeld, J., Wu, S. and Mickley, L.: Biogenic Secondary Organic Aerosol over the United States: Comparison of Climatological Simulations with Observations, J. Geophys. Res, 112, D06201, doi:10.1029/2006JD007813, 2007.

Liu, D., Wang, Z., Liu, Z., Winker, D. and Trepte, C.: A height resolved global view of dust aerosols from the first year CALIPSO lidar measurements, J. Geophys. Res., 113, D16214, doi:10.1029/2007JD009776, 2008.

Liu, H., Jacob, D. J., Bey, I. and Yantosca, R. M.: Constraints from ^{210}Pb and ^{7}Be on wet deposition and transport in a global three-dimensional chemical tracer model driven by assimilated meteorological fields, J. Geophys. Res., 106, 12, 109-12,128, 2001.

Liu, J., Fan, S., Horowitz, L. W., and Levy II, H.: Evaluation of factors controlling long-range transport of black carbon to the Arctic, J. Geophys. Res., 116, D04307, doi:10.1029/2010JD015145, 2011.

Liu, Z., Sugimoto, N., and Murayama, T.: Extinction-to-backscatter ratio of Asian dust observed with high-spectral-resolution lidar and Raman lidar, Appl. Opt., 41, 2760-2767, doi:10.1364/AO.41.002760, 2002.

Liu, Z., Vaughan, M. A., Winker, D. M., Hostetler, C. A., Poole, L. R., Hlavka, D., Hart, W. and McGill, M.: Use of probability distribution functions for discriminating between cloud and

aerosol in lidar backscatter data, J. Geophys. Res., 109, D15202, doi:10.1029/2004JD004732, 2004.

Liu, Z., Vaughan, M. A., Winker, D. M., Kittaka, C., Kuehn, R. E., Getzewich, B. J., Trepte, C. R., and Hostetler, C. A.: The CALIPSO Lidar Cloud and Aerosol Discrimination:Version 2 Algorithm and Initial Assessment of Performance, J. Atmos. Ocean. Tech., 26, 1198–1213, doi:10.1175/2009JTECHA1229.1, 2009.

Liu, Z., Kuehn, R., Vaughan, M., Winker, D., Omar, A., Powell, K., Trepte, C., Hu, Y. and Hostetler, C.: The CALIPSO Cloud And Aerosol Discrimination: Version 3 Algorithm and Test Results, 25th International Laser Radar Conference (ILRC), St. Petersburg, Russia, 2010.

Martin, R.V., Jacob, D. J., Yantosca, R. M., Chin, M. and Ginoux, P.: Global and regional decreases in tropospheric oxidants from photochemical effects of aerosols, J. Geophys. Res., 108, 4097, doi:10.1029/2002JD002622, 2003.

Martinsson, B. G., Brenninkmeijer, C. A. M., Carn, S. A., Hermann, M., Heue, K.-P., van Velthoven, P. F. J., and Zahn, A.: Influence of the 2008 Kasatochi volcanic eruption on sulfurous and carbonaceous aerosol constituents in the lower stratosphere, Geophys. Res. Lett., 36, L12813, doi:10.1029/2009GL038735, 2009.

Massom, R. A., et al.: Snow on Antarctic sea ice, Rev. Geophys, 39, 413-445, 2001.

Mattis, I., Ansmann, A., Müller, D., Wandinger, U., and Althausen, D.: Dual-wavelength Raman lidar observations of the extinction to backscatter ratio of Saharan dust, Geophys. Res. Lett., 29(9), 1306, doi:10.1029/2002GL014721.

Matsui, H., Kondo, Y., Moteki, N., Takegawa, N., Sahu, L. K., Zhao, Y., Fuelberg, H. E., Sessions, W. R., Diskin, G., Blake, D. R., Wisthaler, A., and Koike, M.: Seasonal variation of the transport of black carbon aerosol from the asian continent to the Arctic during the ARCTAS aircraft campaign, J. Geophys. Res., 116, D05202, doi:10.1029/2010JD015067, 2011.

McConnell, J. R., Edwards, R., Kok, G. L., Flanner, M. G., Zender, C. S., Saltzman, E. S., Banta, J. R., Pasteris, D. R., Carter, M. M., Kahl, J. D. W.: 20th-Century Industrial Black Carbon Emissions Altered Arctic Climate Forcing, Science, 317(5843), 1381-1384, doi: 10.1126/science.1144856, 2007.

Meijer, S. N., Ockenden W. A., Sweetman, A., Breivik, K., Grimalt, J. O., and Jones, K. C.: Global Distribution and Budget of PCBs and HCB in Background Surface Soils: Implications for Sources and Environmental Processes, Environ. Sci. Technol., 37, 667– 672, 2003.

Mitchell, M.: Visual range in the polar regions with particular reference to the Alaskan Arctic, J. Atmos. Terr. Phys., Special Supplement, 195-211, 1956.

Montilla, E., Mogo, S., Cachorro, V., Lopez, J., and de Frutos, A.: Absorption, scattering and single scattering albedo of aerosols obtained from in situ measurements in the subarctic coastal region of Norway, Atmos. Chem. Phys. Discuss., 11, 2161-2182, doi:10.5194/acpd-11-2161-2011, 2011.

Novakov, T., Ramanathan, V., Hansen, J. E., Kirchstetter, T. W., Sato, M., Sinton, J. E., and Satahye, J. A.: Large historical changes of fossil-fuel black carbon aerosols. *Geophys. Res. Lett.*, 30(6), 1324, doi:10.1029/2002GL016345, 2003.

Olivier, J. G. J. and Berdowski, J. J. M.: Global emissions sources and sinks, in: The Climate

System, Berdowski, J., Guicherit, R. and B. J. Heij (eds.), A.A. Balkema Publishers/Swets & Zeitlinger Publishers, Lisse, The Netherlands, ISBN 90 5809 255 0, 33-78, 2001.

Omar, A. H, Winker, D. M., Kittaka, C., Vaughan, M. A., Liu, Z. Y., Hu, Y. X., Trepte, C. R., Rogers, R. R., Ferrare, R. A., Lee, K. P., Kuehn, R. E., and Hostetler, C. A.: The CALIPSO automated aerosol classification and lidar ratio selection algorithm, J. Atmos. Oceanic Technol., 26, 1994–2014, doi: 10.1175/2009JTECHA1231.1, 2009.

Park, R. J., Jacob, D. J., Chin, M. and Martin, R. V.: Sources of carbonaceous aerosols over the United States and implications for natural visibility, J. Geophys. Res., 108(D12), 4355, doi:10.129/2002JD003190, 2003.

Park, R. J., Jacob, D. J., Field, B. D., Yantosca, R. M. and Chin, M.: Natural and transboundary pollution influences on sulfate-nitrate-ammonium aerosols in the United States: implications for policy, J. Geophys. Res., 109, D15204, 10.1029/2003JD004473, 2004.

Park, R. J., Jacob, D. J., Palmer, P. I., Clarke, A. D., Weber, R. J., Zondlo, M. A., Eisele, F. L., Bandy, A. R., Thornton, D. C., Sachse, G. W., Bond, T. C.: Export efficiency of black carbon aerosol in continental outflow: Global implications, J. Geophys. Res., 110, D11205, doi:10.1029/2004JD005432, 2005.

Pye, H. O. T., Liao, H., Wu, S., Mickley, L. J., Jacob, D. J., Henze, D. K., and Seinfeld, J. H.: Effect of changes in climate and emissions on future sulfate-nitrate-ammonium aerosol levels in the United States, J. Geophys. Res., 114, D01205, 2009.

Quinn, P. K., Bates, T. S., Miller, T. L., Coffman, D. J., Johnson, J. E., Harris, J. M., Ogren, J. A., Forbes, G., Anderson, T. L., Covert, D. S., Rood, M. J., Surface submicron aerosol chemical composition: what fraction is not sulfate?, J. Geophys. Res., 105, 6785-6805, doi:10.1029/1999JD901034, 2000.

Quinn, P. K., Miller, T. L., Bates, T. S., Ogren, J. A., Andrews, E., and Shaw, G. E.: A three year record of simultaneously measured aerosol chemical and optical properties at Barrow, Alaska, J. Geophys. Res., 107(D11), 4130, doi:10.1029/2001JD001248, 2002.

Quinn, P. K., Shaw, G. E., Andrews, E., Dutton, E. G., Ruoho-Airola, T., and Gong, S. L.: Arctic haze: Current trends and knowledge gaps, Tellus, 59B, 99–114, doi:10.1111/j.1600-0889.2006.00238.x, 2007.

Quinn, P. K., Bates, T. S., Baum, E., Doubleday, N., Fiore, A. M., Flanner, M., Fridlind, A., Garrett, T. J., Koch, D., Menon, S., Shindell, D., Stohl, A., and Warren, S. G.: Short-lived pollutants in the Arctic: their climate impact and possible mitigation strategies, Atmos. Chem. Phys., 8, 1723-1735, doi:10.5194/acp-8-1723-2008, 2008.

Quinn, P. K., Bates, T. S., Schulz, K., and Shaw, G. E.: Decadal trends in aerosol chemical composition at Barrow, Alaska: 1976–2008, Atmos. Chem. Phys., 9, 8883-8888, doi:10.5194/acp-9-8883-2009, 2009.

Raatz, W., and Shaw, G. E.: Long-range tropospheric transport of pollution aerosols into the Alsakan Arctic, J. Clim. Appl. Meteorol., 23(7), 1052–1064, 1984.

Rahn, K. A., Borys, R. D., and Shaw, G. E.: Asian source of Arctic haze bands, Nature, 268, 713–715, 1977.

Rahn, K. A. and McCaffrey, R. J.: On the origin and transport of the winter Arctic aerosol, Ann. N. Y. Acad. Sci., 338, 486–503, 1980.

Rahn, K. A.: The Mn/V ratio as a tracer of large-scale sources of pollution aerosol for the Arctic, Atmos. Environ., 15(8), 1457–1464, doi:10.1016/0004-6981(81)90352-8, 1981.

Rahn, K. A., and Lowenthal, D. H.*:* Elemental tracers of distant regional pollution aerosols, Science, 223(4632), 132-139, doi: 10.1126/science.223.4632.132, 1984.

Rankin, A. W., Wolff, E. W., and Martin, S.: Frost flowers: Implications for tropospheric chemistry and ice core interpretation, J. Geophys. Res., 107, D23, 4683, doi:10.1029/2002JD002492, 2002.

Rankin, A. W. and Wolff, E. W., A year-long record of size-segregated aerosol composition at Halley, Antarctica, J. Geophys. Res., 108, D24, 4775, doi:10.1029/2003JD003993, 2003.

Rastigejev, Y., Park, R., Brenner, M. P. and Jacob, D. J.: Resolving intercontinental pollution plumes in global models of atmospheric transport, J. Geophys. Res., 115, D02302, doi:10.1029/2009JD012568, 2010.

Ritter, C., Notholt, J., Fisher, J., and Rathke, C.: Direct thermal radiative forcing of tropospheric aerosol in the Arctic measured by ground based infrared spectrometry, Geophys. Res. Lett., 32, L23816, doi:10.1029/2005GL024331, 2005.

Rogers, R. R., Hostetler, C. A., Hair, J. W., Ferrare, R. A., Liu, Z., Obland, M. D., Harper, D. B., Cook, A. L., Powell, K. A., Vaughan, M. A., and Winker D. M.: Assessment of the CALIPSO Lidar 532nm attenuated backscatter calibration using the NASA LaRC airborne High Spectral Resolution Lidar, Atmos. Chem. Phys., 11, 1295–1311, doi:10.5194/acp-11-1295-2011, 2011.

Scheuer, E., Talbot, R. W., Dibb, J. E., Seid, G. K., DeBell, L., and Lefer, B.: Seasonal distributions of fine aerosol sulfate in the North American Arctic basin during TOPSE, J. Geophys. Res., 108(D4), 8370, doi:10.1029/2001JD001364, 2003.

Schmale, J., Schneider, J., Ancellet, G., Quennehen, B., Stohl, A., Sodemann, H., Burkhart, J. F., Hamburger, T., Arnold, S. R., Schwarzenboeck, A., Borrmann, S., and Law, K. S.: Source identification and airborne chemical characterisation of aerosol pollution from long-range transport over Greenland during POLARCAT summer campaign 2008, Atmos. Chem. Phys., 11, 10097-10123, doi:10.5194/acp-11-10097-2011, 2011.

Seager, R., Y. Kushnir, J. Nakamura, M. Ting, and N. Naik: Northern Hemisphere winter snow anomalies: ENSO, NAO and the winter of 2009/10, Geophys. Res. Lett., 37, L14703, doi:10.1029/2010GL043830, 2010.

Shao, Y. and Dong, C. H.: A review on East Asian dust storm climate, modeling and monitoring, Glob. Planet. Change, 52, 1–22, 2006.

Shaw, G. E.: The Arctic Haze phenomenon, Bull. Am. Meteorol. Soc., 76(12), 2403–2413, doi: 10.1175/1520-0477(1995)076<2403:TAHP>2.0.CO;2, 1995.

Shindell, D. T., Chin, M., Dentener, F., Doherty, R. M., Faluvegi, G., Fiore, A. M., Hess, P., Koch, D. M., MacKenzie, I. A., Sanderson, M. G., Schultz, M. G., Schulz, M., Stevenson, D. S., Teich, H., Textor, C., Wild, O., Bergmann, D. J., Bey, I., Bian, H., Cuvelier, C., Duncan, B. N., Folberth, G., Horowitz, L. W., Jonson, J., Kaminski, J. W., Marmer, E., Park, R., Pringle, K. J., Schroeder, S., Szopa, S., Takemura, T., Zeng, G., Keating, T. J., and Zuber, A.: A multi-model

assessment of pollution transport to the Arctic, Atmos. Chem. Phys., 8, 5353-5372, doi:10.5194/acp-8-5353-2008, 2008.

Shindell, D. and Faluvegi, G.: Climate response to regional radiative forcing during the twentieth century, Nature Geosci., 2, 294-300, doi:10.1038/ngeo473, 2009.

Shinozuka, Y., Redemann, J., Livingston, J. M., Russell, P. B., Clarke, A. D., Howell, S. G., Freitag, S., O'Neill, N. T., Reid, E. A., Johnson, R., Ramachandran, S., McNaughton, C. S., Kapustin, V. N., Brekhovskikh, V., Holben, B. N., and McArthur, L. J. B.: Airborne observation of aerosol optical depth during ARCTAS: vertical profiles, inter-comparison and fine-mode fraction, Atmos. Chem. Phys., 11, 3673-3688, doi:10.5194/acp-11-3673-2011, 2011.

Sirois, A. and Barrie, L.A.: Arctic lower tropospheric aerosol trends and composition at Alert, Canada: 1980-1995, J. Geophys. Res., 104, doi: 10.1029/1999JD900077, 1999.

Solomon, S., Qin, D., Manning, M., Alley, R. B., Berntsen, T., Bindoff, N. L., Chen, Z., Chidthaisong, A., Gregory, J. M., Hegerl, G. C., Heimann, M., Hewitson, B., Hoskins, B. J., Joos, F., Jouzel, J., Kattsov, V., Lohmann, U., Matsuno, T., Molina, M., Nicholls, N., Overpeck, J., Raga, J., Ramaswamy, V., Ren, J., Rusticucci, M., Somerville, R., Stocker, T. F., Whetton, P., Wood, R. A., and Wratt, D., 2007: Technical Summary. In Climate Change 2007: The Physical Science Basis. Contribution of Working Group I to the Fourth Assessment Report of the Intergovernmental Panel on Climate Change [Solomon, S., Qin, D., Manning, M., Chen, Z., Marquis, M., Averyt, K. B., Tignor, M., and Miller H. L. (eds.)]. Cambridge University Press, United Kingdom and New York, NY, USA.

Stern, D. I.: Global sulfur emissions from 1850 to 2000, Chemosphere, 58, 163–175, doi:10.1016/j.chemosphere.2004.08.022, 2005.

Stocks, B. J. et al., Climate change and forest fire potential in Russian and Canadian boreal forests, Climatic Change, 38, 1-13, 1998.

Stohl, A.: Characteristics of atmospheric transport into the Arctic troposphere, J. Geophys. Res., 111, D11306, doi:10.1029/2005JD006888, 2006.

Stohl, A., Eckhardt, S., Forster, C., James, P., and Spichtinger, N.: On the pathways and timescales of intercontinental air pollution transport, J. Geophys. Res., 107(D23), 4684, doi:10.1029/2001JD001396, 2002.

Sun, J., Zhang, M., and Liu, T.: Spatial and temporal characteristics of dust storms in China and its surrounding regions, 1960–1999: Relations to source area and climate, J. Geophys. Res., 106(D10), 10,325–10,333, doi:10.1029/2000JD900665, 2001.

Tegen, I. and Lacis, A. A.: Modeling of particle size distribution and its influence on the radiative properties of mineral dust aerosol. J. Geophys. Res., 101, 19237-19244, doi:10.1029/95JD03610, 1996.

Textor, C., Schulz, M., Guibert, S., Kinne, S., Balkanski, Y., Bauer, S., Berntsen, T., Berglen, T., Boucher, O., Chin, M., Dentener, F., Diehl, T., Easter, R., Feichter, H., Fillmore, D., Ghan, S., Ginoux, P., Gong, S., Grini, A., Hendricks, J., Horowitz, L., Huang, P., Isaksen, I., Iversen, I., Kloster, S., Koch, D., Kirkevåg, A., Kristjansson, J. E., Krol, M., Lauer, A., Lamarque, J. F., Liu, X., Montanaro, V., Myhre, G., Penner, J., Pitari, G., Reddy, S., Seland, Ø., Stier, P., Takemura, T., and Tie, X.: Analysis and quantification of the diversities of aerosol life cycles within AeroCom, Atmos. Chem. Phys., 6, 1777-1813, doi:10.5194/acp-6-1777-2006, 2006.

Textor, C., Schulz, M., Guibert, S., Kinne, S., Balkanski, Y., Bauer, S., Berntsen, T., Berglen, T., Boucher, O., Chin, M., Dentener, F., Diehl, T., Feichter, J., Fillmore, D., Ginoux, P., Gong, S., Grini, A., Hendricks, J., Horowitz, L., Huang, P., Isaksen, I. S. A., Iversen, T., Kloster, S., Koch, D., Kirkevåg, A., Kristjansson, J. E., Krol, M., Lauer, A., Lamarque, J. F., Liu, X., Montanaro, V., Myhre, G., Penner, J. E., Pitari, G., Reddy, M. S., Seland, Ø., Stier, P., Takemura, T., and Tie, X.: The effect of harmonized emissions on aerosol properties in global models – an AeroCom experiment, Atmos. Chem. Phys., 7, 4489-4501, doi:10.5194/acp-7-4489-2007, 2007.

Tomasi, C., et al.: Aerosols in polar regions: A historical overview based on optical depth and in situ observations, J. Geophys. Res., 112, D16205, doi:10.1029/2007JD008432, 2007.

Treffeisen, R. E., Thomason, L. W. , Ström, J., Herber, A. B., Burton, S. P., and Yamanouchi, T.: Stratospheric Aerosol and Gas Experiment (SAGE) II and III aerosol extinction measurements in the Arctic middle and upper troposphere, J. Geophys. Res., 111, D17203, doi:10.1029/2005JD006271, 2006.

Twomey, S., The influence of pollution on the shortwave albedo of clouds, J. Atmos. Sci., 34, 1149-1152, 1977.

Valero, F. P. J., Ackerman, T. P., and Gore J. Y.: The absorption of solar radiation by the Arctic atmosphere during the haze season and its effects on the radiation balance, Geophys. Res. Lett., 11(5), 465-468, 1984.

Val Martin, M., Logan, J. A., Kahn, R. A., Leung, F.-Y., Nelson, D. L., and Diner, D. J.: Smoke injection heights from fires in North America: analysis of 5 years of satellite observations, Atmos. Chem. Phys., 10, 1491-1510, doi:10.5194/acp-10-1491-2010, 2010.

van der Werf, G. R., Randerson, J. T., Giglio, L., Collatz, G. J., Kasibhatla, P. S., and Arellano Jr., A. F.: Interannual variability in global biomass burning emissions from 1997 to 2004, Atmos. Chem. Phys., 6, 3423–3441, doi:10.5194/acp-6-3423-2006, 2006.

van Donkelaar, A., Martin, R.V., and Park, R.J.: Estimating ground-level $PM_{2.5}$ using aerosol optical depth determined from satellite remote sensing, J. Geophys. Res., 111, doi: 10.1029/2005JD006996, 2006.

van Donkelaar, A., Martin, R. V., Leaitch, W. R., Macdonald, A. M., Walker, T. W., Streets, D. G., Zhang, Q., Dunlea, E. J., Jimenez, J. L., Dibb, J. E., Huey, L. G., Weber, R., and Andreae, M. O.: Analysis of aircraft and satellite measurements from the Intercontinental Chemical Transport Experiment (INTEX-B) to quantify long-range transport of East Asian sulfur to Canada, Atmos. Chem. Phys., 8, 2999-3014, doi:10.5194/acp-8-2999-2008, 2008.

Vaughan, M., Young, S., Winker, D., Powell, K., Omar, A., Liu, Z., Hu, Y. and Hostetler, C.: Fully automated analysis of space-based lidar data: an overview of the CALIPSO retrieval algorithms and data products, Proc. SPIE, 5575, 16-30, doi:10.1117/12.572024, 2004.

Wallace, J. M. and Gutzler, D. S.: Teleconnections in the Geopotential Height Field during the Northern Hemisphere Winter, Mon. Weather Rev., 109, 784-812, 1981.

Wang, H., Easter, R. C., Rasch, P. J., Wang, M., Liu, X., Ghan, S. J., Qian, Y., Yoon, J.-H., Ma, P.-L., and Vinoj, V.: Sensitivity of remote aerosol distributions to representation of cloud-aerosol interactions in a global climate model, Geosci. Model Dev., 6, 765-782, doi:10.5194/gmd-6-765-2013, 2013.

Wang, Q., Jacob, D. J., Fisher, J. A., Mao, J., Leibensperger, E. M., Carouge, C. C., Le Sager, P., Kondo, Y., Jimenez, J. L., Cubison, M. J., and Doherty, S. J.: Sources of carbonaceous aerosols and deposited black carbon in the Arctic in winter-spring: implications for radiative forcing, Atmos. Chem. Phys., 11, 12453-12473, doi:10.5194/acp-11-12453-2011, 2011.

Wang, Y., Jacob D. J. and Logan J. A.: Global simulation of tropospheric O3-NOx-hydrocarbon chemistry, 1. Model formulation, J. Geophys. Res., 103, D9, 10,713-10,726, 1998.

Warneke, C., Bahreini, R., Brioude, J., Brock, C. A., de Gouw, J. A., Fahey, D. W., Froyd, K. D., Holloway, J. S., Middlebrook, A., Miller, L., Montzka, S., Murphy, D. M., Peischl, J., Ryerson, T. B., Schwarz, J. P., Spackman, J. R., Veres, P.: Biomass burning in Siberia and Kazakhstan as an important source for haze over the Alaskan Arctic in April 2008, Geophys. Res. Lett., 36, L02813, doi:10.1029/2008GL036194, 2009.

Warneke, C., Froyd, K. D., Brioude, J., Bahreini, R., Brock, C. A., Cozic, J., de Gouw, J. A., Fahey, D. W., Ferrare, R., Holloway, J. S., Middlebrook, A. M., Miller, L., Montzka, S., Schwarz, J. P., Sodemann, H., Spackman, J. R., and Stohl, A.: An important contribution to springtime Arctic aerosol from biomass burning in Russia, Geophys. Res. Lett., 37, L01801, doi:10.1029/2009GL041816, 2010.

Warren, S. G. and Wiscombe, W. J.: Dirty snow after nuclear-war, Nature, 313, 467-470, 1985.

Wesely, M. L.: Parameterization of surface resistance to gaseous dry deposition in regional-scale numerical models, Atmos. Environ., 23, 1293-1304, 1989.

Winker D. M., Hunt, W., Hostetler, C.: Status and performance of the CALIOP lidar, Proc. SPIE Int. Soc. Opt. Eng., 5575, 8-15, 2004.

Winker, D. M., Vaughan, M. A., Omar, A., Hu, Y., and Powell, J. A.: Overview of the CALIPSO Mission and CALIOP Data Processing Algorithms, J. Atmos. Ocean. Tech., 26, 2310–2323, doi:10.1175/2009JTECHA1281.1, 2009.

Winker, D. M., Tackett, J. L., Getzewich, B. J., Liu, Z., Vaughan, M. A., and Rogers, R. R.: The global 3-D distribution of tropospheric aerosols as characterized by CALIOP, Atmos. Chem. Phys., 13, 3345-3361, doi:10.5194/acp-13-3345-2013, 2013.

Witte, J. C., Douglass, A. R., da Silva, A., Torres, O., Levy, R., and Duncan, B. N.: NASA A-Train and Terra observations of the 2010 Russian wildfires, Atmos. Chem. Phys., 11, 9287-9301, doi:10.5194/acp-11-9287-2011, 2011.

Wood, R.: Rate of loss of cloud droplets by coalescence in warm clouds, J. Geophys. Res., 111, D21205, doi:10.1029/2006JD007553, 2006.

Yang, X., Pyle, J. A., and Cox, R. A.: Sea salt aerosol production and bromine release: Role of snow on sea ice, Geophys. Res. Lett., 35, L16815, doi:10.1029/2008GL034536, 2008.

Young, S. A., and Vaughan, M. A.: The retrieval of profiles of particulate extinction from Cloud Aerosol Lidar Infrared Pathfinder Satellite Observations (CALIPSO) data: Algorithm description, J. Atmos. Ocean. Tech., 26, 1105–1119, doi:10.1175/2008JTECHA1221.1, 2009.

Yu, H., Chin, M., Winker, D. M., Omar, A. H., Liu, Z., Kittaka, C., and Diehl, T.: Global view of aerosol vertical distributions from CALIPSO lidar measurements and GOCART simulations: Regional and seasonal variations, J. Geophys. Res., 115, D00H30, doi:10.1029/2009JD013364, 2010.

Yumimoto, K., Eguchi, K., Uno, I., Takemura, T., Liu, Z., Shimizu, A., and Sugimoto, N.: An elevated large-scale dust veil from the Taklimakan Desert: Intercontinental transport and three-dimensional structure as captured by CALIPSO and regional and global models, Atmos. Chem. Phys., 9, 8545-8558, doi:10.5194/acp-9-8545-2009, 2009.

Zender, C. S., Bian, H., Newman, D., The mineral dust entrainment and deposition (DEAD) model: description and 1990s dust climatology, J. Geophys. Res, 108(D14), 4416, doi:10.1029/2002JD002775, 2003.

Zhang, Q., Streets, D. G., Carmichael, G. R., He, K. B., Huo, H., Kannari, A., Klimont, Z., Park, I. S., Reddy, S., Fu, J. S., Chen, D., Duan, L., Lei, Y., Wang, L. T., and Yao, Z. L.: Asian emissions in 2006 for the NASA INTEX-B mission, Atmos. Chem. Phys., 9, 5131-5153, 2009.

Zieger, P., Fierz-Schmidhauser, R., Weingartner, E., and Baltensperger, U.: Effects of relative humidity on aerosol light scattering: results from different European sites, Atmos. Chem. Phys. Discuss., 13, 8939-8984, doi:10.5194/acpd-13-8939-2013, 2013.